MICROSTRUCTURAL CHARACTERIZATION & VISCOELASTIC PROPERTIES OF AlZnMg & AlCuMg ALLOYS

by

José I. Rojas

Supervisor: Daniel Crespo

DOCTORAL PROGRAMME IN
AEROSPACE SCIENCE & TECHNOLOGY

ESCOLA D'ENGINYERIA DE TELECOMUNICACIÓ I
AEROESPACIAL DE CASTELLDEFELS (EETAC)

UNIVERSITAT POLITÈCNICA DE CATALUNYA (UPC)

Barcelona, July 2011

A thesis submitted in fulfilment of the requirements to obtain the title of
Doctor by Universitat Politècnica de Catalunya

ABSTRACT

Historically, much research has been devoted to the characterization of most of the mechanical properties of materials. However, the viscoelastic behaviour of metals, consequence of internal friction when subjected to fluctuating loads, has received much less attention. The comprehension of the underlying physics of this phenomenon is of high interest as structural materials are subjected to dynamic loads in most applications, and also because it enables a deeper understanding of several technologically essential properties, like mechanical damping and yielding. Thus, research on this field is needed not only because it may lead to new potential applications of metals, but also because predictability of the fatigue response may be greatly enhanced. Indeed, fatigue is the consequence of microstructural effects induced in a material under dynamic loading, while the viscoelastic behaviour is also intimately linked to the microstructure. Accordingly, the characterization of the viscoelastic response of a material offers an alternative method for analysing its microstructure and ultimately its fatigue behaviour.

The research reported in this document is aimed at the identification, characterization and modelling of the effects of temperature, frequency of dynamic loading and microstructure/phase transformations (when present) on the viscoelastic behaviour of commercial aluminium alloys AA 7075-T6 and 2024-T3, and of pure aluminium in the H24 temper. The identification and characterization of the mechanical relaxation processes taking place will be attempted for all these materials. Furthermore, this research pursues to identify the relation between the viscoelastic response of AA 7075-T6 and AA 2024-T3 and the fatigue behaviour, which is of remarkable importance in view of the structural applications of these alloys. Finally, we intend to investigate possible influences of the dynamic loading frequency on fatigue, and especially the existence of a threshold frequency marking the transition from a static-like response of the material to the advent of fatigue problems.

AA 7075-T6 and AA 2024-T3 were selected for this study because these alloys are key representatives of their important families, and are highly suitable to a number of industrial applications, especially in the aerospace sector and transport industry. Pure aluminium was selected because of the inherent interest of this metal and because the results obtained may be used for comparison purposes with data available in the literature and when discussing on the phenomena observed for AA 7075-T6 and AA 2024-T3.

To accomplish the proposed objectives, the viscoelastic response of AA 7075-T6, AA 2024-T3 and pure aluminium in H24 temper was measured experimentally with a Dynamic-Mechanical Analyser (DMA). The results of this analysis were combined with Transmission Electron Microscopy (TEM) and Differential Scanning Calorimetry (DSC). Next, an analytical model is proposed which fits the storage modulus up to 300 ºC. The model takes into account the effect of temperature, the excitation frequency and the concentration of Guinier-Preston Zones (GPZ) and η’ phase in AA 7075-T6, and GPZ/Guinier-Preston-Bagariastkij Zones (GPBZ), and θ’/S’ phase in AA 2024-T3. This allows us to test models proposed for the reaction rates, to determine the kinetic parameters of these microstructural transformations and to

characterize their influence on the viscoelastic behaviour, showing that the DMA is a good tool for studying the material microstructure, phase transformation kinetics and the influence of transformations on the viscoelastic properties of materials.

The TTS principle has been successfully applied to the DMA data, providing master curves for the storage and loss moduli, and enabling extrapolation of the viscoelastic behaviour to any frequency and temperature within the regions of validity. Also, it is proposed that the decrease of yield and fatigue strength with temperature observed in some aluminium alloys may be due to the internal friction increase with temperature, and possible relaxation mechanisms are suggested for the studied materials. Finally, the existence of a threshold frequency is suggested, below which materials subjected to dynamic loading exhibit a static-like, elastic response, such that creep mechanisms dominate. In this regime, deterioration due to fatigue may be neglected. A procedure to estimate this transition frequency is proposed.

KEYWORDS

viscoelastic behaviour, aluminium alloy, AlZnMg, AlCuMg, AA 7075, AA 2024, microstructure, phase transformations, Guinier-Preston Zones, storage modulus, loss modulus, dynamic-mechanical analysis

ACKNOWLEDGEMENT

First, I would like to acknowledge and thank the priceless help and advice that I have received throughout my research work from my PhD advisor, Dr. Daniel Crespo.

Second, I would like to thank also the help that I have received at different times from Dr. José M. Calderón, Dr. Mónica Mihaela, Joshua Tristancho, Dr. Lluís Gil, Joan M. Portero, Víctor Ortiga, David Díaz, Dr. Douglas P. Romilly, Dr. Randal C. Clark, Dr. Jaime O. Casas, José A. Membrive, Dr. Josep L. Tamarit, Dr. Néstor Veglio, Dr. Joan Torrens, Dr. Josep Sabaté, Dr. Trinitat Pradell, Dr. Pere Bruna and Dr. Eloi Pineda.

At last but not least, I would like to thank the essential support I have received at all moment from Isabel, Marta, María V., Jordi, Raúl, José I., my co-workers at EETAC-UPC, and more recently Tiago.

Dedicated to my wonderful family
and especially to Isabel and Tiago

CONTENTS

LIST OF FIGURES

LIST OF TABLES

ACRONYMS

1DAP	1-Dimensional Atom Probe
3DAP	3-Dimensional Atom Probe
3PB	3-Point Bending
AA	Aluminium Alloy
bcc	Body-centered cubic
CCD	Charge-coupled device
CEN	European Committee for Standardization
CFCG	Creep-fatigue crack growth
DIC	Differential Isothermal Calorimeter/Calorimetry
DMA	Dynamic-Mechanical Analyser/Analysis
DSC	Differential Scanning Calorimeter/Calorimetry
EETAC	Escola d'Enginyeria de Telecomunicació i Aeroespacial de Castelldefels
fcc	Face-centered cubic
FCG	Fatigue crack growth
GPBZ	Guinier-Preston-Bagariastkij Zones
GPZ	Guinier-Preston Zones
HCF	High cycle fatigue
hcp	Hexagonal close-packed
HREM	High-Resolution Electron Microscope/Microscopy
HRTEM	High-Resolution Transmission Electron Microscope/Microscopy
IADS	International Alloy Designation System
JMAK	Johnson-Mehl-Avrami-Kolmogorov
N/A	Non applicable/Non available
PUCOT	Piezoelectric Ultrasonic Composite Oscillator Technique
RRA	Retrogression & Re-ageing
RT	Room temperature
SAED	Selected Area Electron Diffraction
SEM	Scanning Electron Microscope/Microscopy
SSS	(Super) Saturated solid solution
TEM	Transmission Electron Microscope/Microscopy
TTS	Time-Temperature Superposition
UPC	Universitat Politècnica de Catalunya
UTS	Ultimate Tensile Strength/Stress
VHCF	Very high cycle fatigue
WLF	Williams-Landel-Ferry

SYMBOLS

a	Crack length
a_T	Shift factor
C	Concentration
C_1	GPZ/GPBZ concentration
C_2	η' or θ'/S' phase concentration
$C/C_{reference}$	Transformed fraction
d	Sample thickness
E	Static and dynamic elastic (or tensile or Young's) modulus
E'	Storage modulus
E'_0	Model coefficient accounting for the temperature gradient of the storage modulus
E'_1	Model coefficient accounting for the contribution of GPZ to the storage modulus
E'_2	Model coefficient accounting for the contribution of η' phase for AA 7075-T6, or θ'/S' phases for AA 2024-T3, to the storage modulus
E'_{RT}	Model coefficient accounting for the storage modulus at RT
E''	Loss modulus
E_A	Activation energy
f	Frequency [Hz]
k_0	Pre-exponential coefficient
K	Boltzmann constant
K_{max}	Stress intensity factor
K_S	Stiffness
L	Sample length
m	Constant
n	Avrami exponent
N	Number of loading cycles
N_{exp}	Number of experimental observations
q	Heat flow
r	Constant
R	Stress ratio (ratio minimum-to-maximum stress levels)
S	Stress amplitude
S	Incoherent stable (equilibrium) Al_2CuMg phase
S'	Semi-coherent metastable Al_2CuMg phase
S"	Semi-coherent metastable Al_2CuMg phase
t	Time
T	Temperature
T_0	Arbitrary chosen reference temperature for application of TTS principle
T_C	Critical loading period

$Tan\ \delta$	Loss tangent, loss factor, internal friction or mechanical damping
w	Sample width
z	Number of frequencies solved simultaneously in the integration of the model

GREEK SYMBOLS

δ	Angle between the dynamic tensile modulus and the storage modulus
ε	Strain
η	Incoherent stable (equilibrium) $MgZn_2$ phase
η'	Semi-coherent metastable $MgZn_2$ phase
θ	Incoherent stable (equilibrium) Al_2Cu phase
θ'	Semi-coherent metastable Al_2Cu phase
θ"	Semi-coherent metastable Al_2Cu phase
μ	Micron (10^{-6} mm)
ν	Poisson's ratio
ν_r	Relaxation rate
σ	Stress
τ	Characteristic transformation time
Φ	DSC heating rate
ψ	Error function
ω	Frequency [rad·s^{-1}]

GLOSSARY

Age hardening: Process of formation of precipitates from the decomposition of a metastable super-saturated solid solution. This process may develop slowly at room temperature (natural ageing) or faster at higher temperatures (artificial ageing). In any case, it modifies the microstructure and causes changes in properties such as strength, hardness and plasticity.

Ageing sequence: Decomposition path of the metastable super-saturated solid solution (SSS), evolving towards an equilibrium structure.

Ageing treatment: Synonym of age hardening.

Annealing: Heat treatment by which plastic deformation attained by cold working may be eliminated, or by which coalescence of precipitates formed from a solid solution may be promoted. This treatment modifies the microstructure and causes changes in properties such as strength, hardness and plasticity.

Artificial ageing: Process of decomposition of a metastable super-saturated solid solution that is forced by heat-treatment at a given temperature and during a given time.

Basal plane: Plane perpendicular to the principal c-axis in a tetragonal or hexagonal crystal structure.

Coherent phase: A crystalline precipitate that forms from a super-saturated solid solution and that maintains continuity in the crystal lattice and atomic arrangement between the precipitate and the matrix, usually accompanied by a strain field in both lattices.

Cold working: Process of application of plastic deformation on a metal, which causes the following effects on the mechanical properties: significant increase in the yield strength, tensile strength and hardness, and noticeable loss of plasticity.

Complex defect: Class of crystal imperfection resulting from a combination of two or more elementary point defects.

Composite defect: Synonym of complex defect.

Corrosion: Process of degradation of a material due to chemical reaction with its environment.

Creep: Process by which a solid material strains in a time-dependent manner under constant stress.

Defect complex: Synonym of complex defect.

Diffusion: Flow mechanism consisting in a continuous displacement with time of atoms or molecules within the material.

Dislocation: A linear microstructural imperfection around which some atoms are misaligned.

Ductility: Capacity of a material to undergo permanent (plastic) deformation under stress.

Elementary point defect: The simplest class of crystal imperfections. The types of elementary point defects are: vacancies, substitutional atoms and interstitial atoms.

Elastic modulus: Slope of the stress-strain curve, in the linear elastic region, obtained by tension test.

Elongation: Lengthening of a material subjected to tensile stress.

Endurance limit: Stress level below which a material withstands dynamic loading indefinitely without exhibiting fatigue failure.

Enthalpy: Thermodynamic magnitude which is a measure of the total energy of a thermodynamic system, and in particular of a material. It is the sum of the internal energy of the system plus the product of pressure and volume.

Entropy: Thermodynamic magnitude which is the measure of the disorder in a thermodynamic system, or a material. It is also a measure of the unavailability of a system's thermal energy for being converted into mechanical work.

Fatigue: Form of failure that occurs in structures subjected to dynamic loading.

Fatigue life: Number of stress cycles of a specified character that a specimen sustains before failure of a specified nature occurs.

Fatigue limit: Synonym of endurance limit.

Fatigue resistance: Stress amplitude at which fatigue failure occurs for a given number of cycles.

Fatigue strength: Synonym of fatigue resistance.

Grain boundary: Microstructural interface that separates one crystal or grain from another in a polycrystalline material.

Hardness: Resistance of a material to local plastic (permanent or irreversible) deformation.

Heat capacity: Physical quantity representing the amount of heat required to raise the temperature of a unit mass of a substance by a temperature unit.

Hysteresis heating: Temperature increase due to energy dissipated as heat.

Incoherent phase: A crystalline precipitate that forms from a super-saturated solid solution having no continuity in the crystal lattice and atomic arrangement between the precipitate and the matrix, usually accompanied by larger strains in both lattices.

Interstitial atom: Elementary point defect that results from bringing an extra atom (of the same or a different species) into a position which is not a regular lattice site.

Loss factor: Ratio between the loss modulus and the storage modulus, which is a measure of the internal friction and mechanical damping.

Loss modulus: Viscous (imaginary or plastic) component of the dynamic tensile modulus, which accounts for the energy dissipation due to internal friction (the frictional energy loss) during relaxation processes.

Loss tangent: Synonym of loss factor.

Natural ageing: Process of decomposition of a metastable super-saturated solid solution that takes place spontaneously at room temperature.

Phase transformation: Process by which a material undergoes a change from one phase or mixture of phases to another. This process might involve a modification of the crystal structure or the state of order of the crystal (e.g. atomic order, magnetic order or dipolar order). Examples of phase transformations are allotropic, eutectoid, order-disorder, ferromagnetic and ferroelectric transformations.

Plasticity: Synonym of ductility.

Precipitation path: Synonym of ageing sequence.

PUCOT: Experimental technique that allows the measurement of mechanical damping and dynamic tensile modulus as a function of temperature.

Quenching: Process of fast cooling.

Residual stress: Tensions due to incompatible internal permanent strains that remain after the original cause has been removed. They may be generated or modified at every stage in the component life cycle, from original material production to final disposal, by application of external forces, heat gradients, etc.

Solution treatment and quenching: Heat treatment consisting first in heating the materials at an appropriate temperature and during sufficient time to allow for the formation of a solid solution. Secondly, the solid solution is cooled fast such that a metastable super-saturated solid solution is obtained.

Storage modulus: Elastic (real) component of the dynamic tensile modulus, which is a measure of the deformation energy stored by the material.

Strain hardening: Synonym of cold working.

Stress amplitude: Half of the difference between the maximum and the minimum applied stresses in a loading cycle.

Substitutional atom: Elementary point defect that results from substituting an atom of the crystal lattice with another of a different species.

Tensile strength/stress: Maximum stress in the stress-strain curve obtained by tension test.

Ultimate tensile strength/stress: Synonym of tensile strength/stress.

Vacancy: Elementary point defect that results from removing an atom from the crystal.

Viscoelasticity: Property of materials that exhibit time-dependent strain, thereby showing both viscous and elastic behaviour when undergoing deformation.

Work hardening: Synonym of cold working.

Yield strength/stress: Stress at which a specific amount of permanent (plastic) deformation is produced in the material, usually taken as 0.2% of the unstressed length.

Young's modulus: Synonym of the elastic modulus.

1 INTRODUCTION

Being aeronautics a wide and multidisciplinary field of knowledge, materials science and technology have historically played a role of significant relevance, to such an extent that, in many cases, both have evolved together. That is, breakthrough progresses in materials have frequently leaded to breakthrough improvements in the aerospace sector. Many examples can be easily found: the rise of aluminium alloys and the intense research to improve their mechanical properties, the development of titanium alloys and later nickel super-alloys for turbine blades of air-breathing engines, the use of advanced composite materials for structural applications, etc.

Much research has been devoted to the characterization of most of the mechanical properties of materials and to the development of techniques to produce components with tailored properties. However, the viscoelastic behaviour of metals, consequence of internal friction when subjected to fluctuating loads, has received much less attention. The comprehension of the underlying physics of this phenomenon is of high interest as structural materials are subjected to dynamic loads in most applications, and also because it enables a deeper understanding of several technologically essential properties, like mechanical damping and yielding [1]. Thus, research on this field is important not only because it may lead to new potential applications of metals (e.g. vibration and noise can be reduced using viscoelastic damping materials [2]), but also because predictability of their performances in applications under dynamic loading may be greatly enhanced.

Indeed, fatigue is the consequence of microstructural effects and dislocation-microstructure interactions [3, 4] induced in a material under dynamic loading, and the viscoelastic behaviour is also intimately linked to the microstructure [1, 5]. The latter has been repeatedly shown in metallic glasses, for which mechanical relaxations, transport phenomena, the glass transition and crystallization processes have been studied by dynamic-mechanical analysis [6, 7]. Accordingly, the characterization of the viscoelastic response of a material offers an alternative method for analyzing its microstructure and ultimately its fatigue behaviour.

The research reported in this document is aimed at the identification, characterization and modelling of the effects of temperature, frequency of dynamic loading and microstructure/phase transformations (when present) on the viscoelastic behaviour of commercial aluminium alloys AA 7075-T6 and 2024-T3, and of pure aluminium in the H24 temper. The identification of the mechanical relaxation processes taking place will be attempted for all these materials, too. Ultimately, this research pursues to identify the relation between the viscoelastic response of AA 7075-T6 and AA 2024-T3 (and in particular, the internal friction caused by the mechanical relaxation processes taking place) and the fatigue behaviour, which is of remarkable importance in view of the structural applications of these alloys. We decided to focus this research specifically on the low temperature regions (in this case, approximately from RT to 300 ºC). The reason is that, in the aerospace sector, most of the structural components made from aluminium alloys

which are likely to suffer from fatigue work at low temperatures throughout their service life. Finally, we intend to investigate possible influences of the dynamic loading frequency on fatigue, and especially the existence of a threshold frequency marking the transition from a static-like response of the material to the advent of fatigue problems.

AA 7075-T6 and AA 2024-T3 were selected for this study because these alloys are key representatives of their important families (i.e. AlZnMg and AlCuMg alloys from 7XXX and 2XXX series, respectively). After proper treatments, AlZnMg alloys feature excellent specific mechanical properties, while AlCuMg alloys have excellent fatigue resistance, formability and corrosion resistance [8] and retain high strength at high temperature [9]. These are the reasons why both families are highly suitable to a number of industrial applications, especially in the aerospace sector and transport industry. For instance, these alloys are widely used in skin panels, especially in military aircraft [10-12], but also in commercial civil aviation aircrafts [13]. Pure aluminium was selected because of the inherent interest of studying this metal and because the results obtained may be used as a baseline reference for comparison purposes with data available in the literature and when discussing some of the phenomena observed for AA 7075-T6 and AA 2024-T3.

In this document, the research work to accomplish the proposed objectives is described in five chapters. The state of the art on fatigue, viscoelastic properties and relaxation phenomena for AlZnMg and AlCuMg alloys, the characteristics of their ageing paths and precipitates, and the modelling of the kinetics of the transformations involved is presented in Chapter 1. In Chapter 2, the materials and methods to conduct the experiments are reviewed, and the test results for AA 7075-T6, AA 2024-T3 and pure aluminium are presented. In Chapter 3, a model to account for the behaviour of the storage modulus on temperature and loading frequency is proposed, and the model results for AA 7075-T6, AA 2024-T3 and pure aluminium are shown. In Chapter 4, the experimental results, the model results and related findings are discussed. Finally, Chapter 5 presents the conclusions derived from this research work.

1.1 ALUMINIUM ALLOYS

Aluminium (initially termed alumium) was officially established and named by Sir Humphry Davy, who first identified its existence as the metal base of alum salts in 1808. However, Hans Christian Oersted is considered to be the first producer of this material, by reduction of aluminium chloride with potassium in 1825. In 1854 Henri Etienne Sainte-Claire Deville from France produced aluminium by reduction of aluminium chloride with sodium, significantly cheaper than potassium, and thus industrial production was initiated in 1856 in Nanterre, France. Nevertheless, in these early stages of production, aluminium was extremely difficult to extract from its ores, like bauxite ore, as discovered by Pierre Berthier.

In 1888, Paul Héroult from France and Charles Martin Hall from the USA independently developed the so-called Hall-Héroult process. In this method, aluminium is obtained by reduction of melted aluminium oxide (i.e. alumina) through electrolysis. Alumina can be refined from aluminium ore or bauxite using the

Bayer process, for instance. Hall's process gave raise in 1888 in USA to the Pittsburgh Reduction Company, known today as Alcoa, while Héroult's process gave raise in 1889 in Switzerland to Aluminium Industrie, known today as Alcan. This techniques made aluminium production cheaper and are still at present day the most important production methods worldwide. Since then, aluminium and aluminium alloys have gradually replaced other materials in many applications [14].

1.1.1 Aluminium families

To avoid confusions that may arise between different actors, industrial sectors or research areas, a designation system was established, by which aluminium alloys are classified into several families or series in terms of the principal alloying element. This system also states the minimum and maximum composition limits for the alloying elements. Fortunately, the number of elements which are significant to aluminium alloys are limited [13]. In particular, the nomenclature accepted by most countries for wrought aluminium alloys is the International Alloy Designation System (IADS), which is a four-digit numerical system (see Table 1) developed by the Aluminium Association. In this system, the first digit designates the alloy family or principal alloying element, the second digit indicates modifications of the original alloy or impurity limits and the last two digits identify the specific aluminium alloy [13].

Table 1 Families for wrought aluminium alloys.

Family	Aluminium content or principal alloying element
1XXX	Pure Aluminium (Al), a minimum purity of 99.0%
2XXX	Copper (Cu)
3XXX	Manganese (Mn)
4XXX	Silicon (Si)
5XXX	Magnesium (Mg)
6XXX	Magnesium (Mg) and Silicon (Si)
7XXX	Zinc (Zn)
8XXX	Others, e.g. Lithium (Li)
9XXX	Unused

Throughout the 20th century and up to present day, aluminium alloys have been widely used in structural applications in aircraft, being those from the families 7XXX and 2XXX the most extended. The former are particularly interesting for applications for which the critical requirement is the strength, while the latter are more convenient when the critical requirement is fatigue resistance [13].

1.1.2 Aluminium treatments

As compared to other metals, pure aluminium features very low hardness, yield strength, tensile strength and elastic modulus. Therefore, to enable the use of aluminium in structural applications it is critical to increase its strength. This can be done by means of several types of treatments. A system was

developed also by the Aluminium Association that allows distinguishing and describing the treatments or tempers to which aluminium alloys are subjected, and therefore their properties, too. This system became part of the IADS and has also been adopted by the major part of countries [13].

For wrought aluminium alloys, the nomenclature for the tempers consists of letters added as suffixes to the four-digit numerical designator of the alloy. The suffix letters for the designation of the basic tempers are presented in Table 2, as described in the UNE-EN 515 standards [13, 15]. Subcategories within a given temper may be designated by one or more digits following the corresponding letter.

Table 2 Basic tempers for wrought aluminium alloys.

Temper designation letter	Description of the treatment
F	For alloys in the as-fabricated condition
H	For alloys in the strain hardened condition
O	For alloys in the annealed condition
T	For alloys in the solution heat-treated and age-hardened condition
W	For alloys in the solution heat-treated condition but which have not achieved a significantly stable condition

The most widely used techniques for strengthening aluminium are strain hardening (or cold working or work hardening), which corresponds to designation letter H, and age hardening, which corresponds to designation letter T.

1.1.3 Strain hardening & H tempers

Strain hardening is based on the application of plastic deformation to aluminium. This process causes a loss of plasticity and an increase in the yield strength, tensile strength and hardness. In this case, the increased resistance to deformation is due to dislocation-dislocation interactions [3]. The main subcategories in the H temper are shown in Table 3, as described in the UNE-EN 515 standards [15]. The first digit after the suffix letter H indicates the treatment applied after cold working. The second digit indicates the attained degree of strain hardening in relation to the reference annealed condition O.

1.1.4 Age hardening & T tempers

Age hardening is based on the formation of precipitates (i.e. structural inhomogeneities) in intermediate stages of the decomposition of the metastable super-saturated solid solution (SSS), evolving towards an equilibrium structure. The SSS has been obtained previously by solution treatment at sufficiently high temperature and permanence time, and quenching at adequate cooling rate. The decomposition of the SSS and formation of precipitates is achieved by excess solute segregation after natural ageing at room temperature (RT) or artificial ageing at higher temperatures [8, 16].

Table 3 Subcategories in the H temper for wrought aluminium alloys.

Subcategory	Description of the treatment after strain hardening
H1X	No treatment has been applied other than the strain hardening
H2X	For alloys that, after having been strain hardened beyond desired hardness, are ultimately softened by partial anneal (the microstructural evolution depends on the annealing temperature and time). For a given value of strength, the metal in the H2 temper has a slightly higher elongation and plasticity than that in the H1 temper
H3X	For alloys with mechanical properties stabilized by low temperature heat-treatment, such that degradation of properties during service life is significantly reduced
H4X	For alloys with possible partial anneal due to heat-treatment after coating application
HX9	Special tempers for which the tensile strength is at least 10 MPa higher than HX8
HX8	Applicable to conventional tempers resulting in peak tensile strength
HX6	Applicable to tempers with tensile strength between HX4 and HX8
HX4	Applicable to tempers with tensile strength between O and HX8
HX2	Applicable to tempers with tensile strength between O and HX4

The particular precipitation path and phase transformations during the ageing process, which depend on the alloy composition, quenching conditions and ageing parameters [16, 17], determine the resulting microstructure, and hence the material properties. In this case, the interaction of decomposition products with dislocations is the principal mechanism responsible for the hardening [3, 8], so the presence of these products is essential for achieving significant hardening [16]. In this atmosphere mechanism, the stress-strain fields associated to solute atoms cause locking of dislocations. That is, plastic deformation is hindered and so hardness is increased. Indeed, for the metastable SSS in AlZnMg alloys, where no precipitates are present, the hardness has been determined to be at its lowest level [16].

The main subcategories in the T temper are shown in Table 4, as described in the UNE-EN 515 standards [15]. Aside from the brief descriptions of the basic tempers and subcategories in Tables 2, 3 and 4, the reader may find more information on these topics in the referenced documents [13, 15].

Table 4 Subcategories in the T temper for wrought aluminium alloys, according to the UNE-EN 515.

Subcategory	Description of the treatment
T1X	Natural ageing at RT (aiming at stabilization) after cooling from hot forming
T2X	Natural ageing at RT after cooling from hot forming and cold-working
T3X	Natural ageing at RT after solution treatment, quenching and cold-working
T4X	Natural ageing at RT after solution treatment and quenching
T5X	Artificial ageing after tempering treatment
T6X	Artificial ageing (aiming at hardening peak) after solution treatment and quenching
T7X	Over-ageing (artificial ageing aiming at a more stable final condition beyond the hardening peak) after solution treatment and quenching
T8X	Artificial ageing after solution treatment, quenching and cold-working
T9X	Cold-working after solution treatment, quenching and artificial ageing

1.2 FATIGUE

Fatigue is a form of failure that occurs in structures that are subjected to dynamic loading, i.e. dynamic stresses/strains. The importance of fatigue in structural applications of materials stems from the fact that failure may occur at stress levels significantly lower compared to the yield stress and/or Ultimate Tensile Stress (UTS) for the particular material when subjected to static loading [18]. Fatigue failure results from a gradual process of damage accumulation and local strength reduction, which is manifested by crack initiation and propagation, after long periods of dynamic loading. It is particularly dangerous because of its brittle, catastrophic nature, and because it occurs suddenly and without warning, since very little plastic deformation is observed prior to failure [18, 19].

In particular, the mechanisms responsible for the fracture behaviour are due to competing and synergistic influences of intrinsic microstructural effects and dislocation-microstructure interactions (e.g. dislocation-dislocation and dislocation-precipitates interactions) [3]. When a material is subjected to dynamic loading, energy is dissipated due to internal friction. Most of this energy manifests as heat and causes temperature increases of the samples. This process is termed hysteresis heating. Amiri [20] affirms that all metals, when subjected to hysteresis heating, are prone to fatigue.

The fatigue response of a material is usually presented graphically by means of an *S-N* curve. This curve is a plot of the parameter *S* vs. the number of loading cycles to failure *N*. The parameter *S* may vary, but it is generally the stress amplitude, i.e. a half of the difference between the maximum and the minimum applied stresses in the loading cycle [18]. Typically, two kinds of behaviour are observed:

- Materials with no fatigue limit (e.g. aluminium, copper, magnesium): These materials present always fatigue failure if dynamically loaded, regardless of the amplitude of the applied stresses. Nevertheless, the number of loading cycles to failure increases monotonically as the stress amplitude is reduced. For these materials, the fatigue behaviour is specified in terms of fatigue strength, which is the stress amplitude at which failure occurs for a given number of cycles.
- Materials with fatigue limit (e.g. some ferrous and titanium alloys): These materials only present fatigue failure when dynamically loaded if the amplitude of the applied stresses is larger than a given value. This stress amplitude level is termed fatigue limit, and it is used to specify the fatigue behaviour of the corresponding material. For these materials, the *S-N* curve decreases initially but becomes horizontal at high numbers of loading cycles, once the fatigue limit is reached.

Fatigue may be sensitive to a significant number of material properties and test or operational conditions, e.g. the strength of the material, the manufacturing conditions of the sample, the surface treatment, the frequency of the mechanical excitation, the loading environment, the displacement rates, the stress amplitude, etc [18, 21-23]. The effects of loading frequency and temperature on fatigue behaviour are dealt more in-depth in the following sections.

1.2.1 Influence of loading frequency on fatigue response of metals

Due to the importance of fatigue in structural applications of metals and the time-consuming nature of fatigue tests, much research has been devoted to ascertain whether accelerated laboratory tests (i.e. with loading frequencies higher than those in service conditions) affect the fatigue response and how, but yet this is a controversial issue. This is particularly true for the study of very high cycle fatigue (VHCF) behaviour by means of very high frequency tests[1]. For instance, Zhu [24] states that environmental effects need to be considered, and Mayer [25] explains that this is so because the time-dependent interaction with the environment may cause an extrinsic frequency influence on fatigue properties, on top of the intrinsic strain rate effects. Furuya [26] states that frequency generally affects high frequency fatigue tests because:

- Fatigue limits and lives decrease due to temperature increase caused by plastic deformation [27].
- Dislocations may not match the applied frequency because dislocation movement is slow compared to sonic velocity [28].
- Provided that embrittlement by hydrogen diffusion had an effect [29], fatigue lives would depend both on number of loading cycles and time.

Nonetheless, Mayer [30] reported also that high cycle fatigue (HCF) behaviour of metallic alloys is relatively insensitive to test frequency, provided that the ultrasonic testing procedure is appropriate (e.g. adequate cooling) and that fatigue-creep interaction and the time-dependent interaction with the environment are negligible. The reasons suggested are, on the one hand, that cyclic plastic straining is limited near the fatigue limit or the threshold of fatigue crack growth (FCG), and thus plastic strain rates are low even at high frequencies; and, on the other hand, the fact that shear stress has little sensitivity to strain rate [31]. Mayer [25] also commented that the influence of frequency becomes significantly smaller if the dynamic stress amplitude is lower, maybe because cyclic loading is almost perfectly elastic.

For body-centered cubic (bcc) metals and metallic alloys, HCF behaviour is reported to be more sensitive to frequency than for face-centered cubic (fcc) metals [32]. For example, for tantalum and titanium it was observed that high frequency tests resulted in longer fatigue lives and higher fatigue limits compared to conventional fatigue tests, at 2×10^8 cycles and temperatures below 30°C. Also, fractured tantalum showed ductile, trans-granular cracks in conventional tests, whereas brittle, crystallographic and inter-granular cracks were more common after high frequency tests, contrary to what commonly reported for fcc metals. However, Furuya [26] observed that fatigue behaviour of high-strength steels is independent of frequency. The argued cause was their extremely high-strength, which reduced plasticity and dislocation mobility. The hysteresis energy is low in low plasticity materials, and thus the frequency effects on fatigue associated to the temperature increase are minimized. Likewise, Yan [33] observed

[1] Tests in VHCF and very low crack growth rates are time consuming with conventional fatigue testing techniques, like rotating bending, with a maximum frequency of 100 Hz. A significant reduction of testing times is possible if using a high-speed servo-hydraulic machine [26], which may work at a frequency of 600 Hz, or specially if using ultrasonic equipment, which may reach a frequency of 20 kHz [32].

very little variation of the fatigue strength of high-strength steel when testing at a conventional frequency (52.5 Hz) and at an ultrasonic frequency (20 kHz).

The fatigue response of pure fcc metals and metallic alloys is relatively insensitive to frequency [32]. For example, for an aluminium alloy similar to AA 7075 tested in the HCF regime at RT, samples tested at 100 Hz tend to fail earlier than those tested at 20 kHz. However, the effect of frequency on fatigue behaviour was not statistically significant [25]. Also, for copper single crystals and poly-crystals, and cycles to failure above 10^6, it was determined that the variation of the test frequency between 60 Hz and 20 kHz has no influence on fatigue life, if samples are adequately cooled [31]. On the contrary, it has also been reported a significant influence of frequency on fatigue response for copper poly-crystals tested at 0.5, 2 and 8 Hz [34]. In this case, it is argued that frequency influences the level of strain localization [35] and thus the resistance of dislocation structures to plastic deformation. In particular, saturation plastic strains were 2.2 times higher and the density of intrusions, extrusions and micro-cracks at the surfaces of the samples was 4 times higher, if cycled at 0.5 Hz compared to 8 Hz [34]. Also, for E319 cast aluminium alloy at 20, 150 and 250 ºC, fatigue life at 20 kHz was 5 to 10 times longer than that at 75 Hz [24], but this author states that fatigue crack initiation is not influenced either by temperature or frequency. Rather, the observed difference in fatigue life is attributed to environmental effects on FCG rate.

The fact that the moisture of ambient air deteriorates the fatigue life of materials (e.g. high-strength aluminium alloys) by increasing the FCG rate has also been suggested by other authors [25, 36]. Namely, Menan [37] suggests for AA 2024-T351 that extrapolation of results from accelerated tests to real operating lives is not appropriate in some cases because fatigue and corrosion may interact such that FCG rates are enhanced. These synergistic effects are more notorious at low frequencies, for a given number of cycles at RT. Finally, Benson [38] observed strain rate effects on cyclic plastic deformation of AA 7075-T6, provided that cyclic stresses were close to the yield stress.

As per research on low frequency loading, Nikbin [39] considered the problem that data are generally limited to either static creep or high frequency (pure) fatigue. Otherwise, tests could allow predict the frequency region of interaction between creep and FCG. He proposed a method to overcome this, and used static data (obtained at 150 ºC for aluminium alloy RR58 and at 550 ºC for steel FV448) and RT high frequency fatigue data to predict the interaction region, assuming a linear cumulative damage law. The results showed that the frequency range of interaction is 0.1 to 1 Hz for the aluminium alloy (see Fig. 1), and 0.01 to 1 Hz for the steel. In the intermediate (steady state) stage of cracking for static and low frequency tests, crack growth is sensitive to frequency and the fracture mode is time-dependent inter-granular in nature, suggesting that creep mechanisms dominate. Conversely, for high frequency tests, crack growth is insensitive to frequency and the fracture mode is trans-granular, suggesting that pure fatigue mechanisms dominate. The results indicated also little interaction between these processes, i.e. either static creep or pure fatigue controls the response except over a narrow frequency range in the transition region.

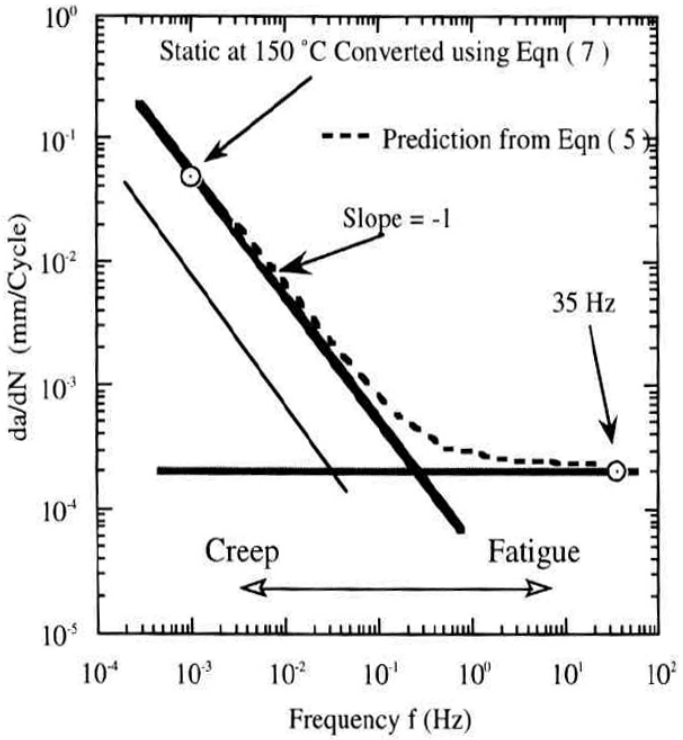

Fig. 1 Crack growth rate *da/dN* vs. frequency *f* at 150 ºC under static and dynamic loading, at a stress intensity factor range of 20 MPa·m$^{1/2}$, for aluminium alloy RR58 [39] (printed with permission from Elsevier).

To enable prediction of crack growth resistance of AA 2650-T6 under very low frequency loading at elevated temperatures, creep crack growth rates, FCG rates and creep-fatigue crack growth (CFCG) rates of this alloy were analysed at 20, 130 and 175 °C, for frequencies of 0.05 and 20 Hz [40]. It was concluded that, in the studied frequency range, frequency has only a slight effect on FCG rates at 175 °C. In particular, under low frequency loading it was observed a high increase in fracture surface fraction of inter-granular type, similar to that corresponding to creep crack growth. This shows that creep damage might occur during loading at low frequency, in accordance with Nikbin's findings [39].

Henaff [40] reported also that, for a given temperature, CFCG is unaffected by frequency above a critical value of the loading frequency (see Fig. 2). Below, CFCG is inversely proportional to excitation frequency, i.e. a time-dependent crack growth processes take place. This researcher suggests the existence of creep-fatigue-environment interaction, as CFCG is affected by the environment at low frequency loading. Accordingly, while fatigue and creep damage can be linearly summed in vacuum, a cumulative rule using creep crack growth data and FCG data is not appropriate in air. An alternative method is proposed to predict CFCG rates at very low frequencies, using a superposition model and results obtained at higher frequencies.

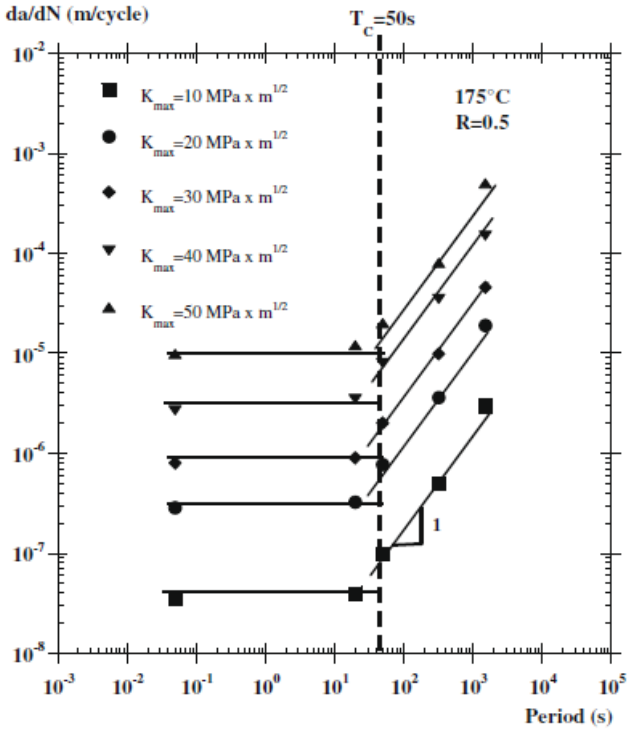

Fig. 2 Creep-fatigue crack growth rates *da/dN* vs. loading period in air at 175 ºC, a stress ratio of 0.5, and several values of stress intensity factor, for AA 2650-T6 [40] (printed with permission from Elsevier).

1.2.2 Influence of temperature on fatigue response of aluminium alloys

Zhu [24] observed for E319 cast aluminium alloy tested at 20, 150 and 250 ºC that fatigue strength decreases with temperature. This author reported also that the temperature dependence of fatigue resistance at 10^8 cycles follows closely the temperature dependence of yield and tensile strength for this alloy. Furthermore, this author states that, by integration of a universal version of a modified superposition model, the effects of temperature, frequency and the environment on the *S-N* curve of this alloy can be predicted, and it is possible also to extrapolate ultrasonic data to conventional fatigue behaviour [24]. Henaff [40] concluded that temperature has almost no influence on FCG rates for AA 2650-T6, after conducting tests at 20, 130 and 175 °C and frequencies of 0.05 and 20 Hz.

1.2.3 Influence of the microstructure on fatigue response of aluminium alloys

This is a very wide research area as the microstructure certainly has a direct influence on the fatigue response of a material. Due to size constraints, it is not our intention to summarize the state of the art in this topic. We will only recall briefly the background that allows us to elaborate the hypothesis of the existence of a relation between the viscoelastic response and the fatigue behaviour, through their mutual dependence on the microstructure. Chung [4] states that it should be possible to predict fatigue life based on the knowledge of the microstructure prior to beginning of service, without the need for expensive, time

consuming experiments. This would enable the optimization of the material properties by simply controlling the microstructure. This author suggests a model based on dislocation stress to predict *S-N* curves using microstructure/material sensitive parameters instead of constitutive equation parameters. The model is reported to be successful for low cycle fatigue life prediction. In turn, Amiri [20] states that the slope of the temperature rise due to hysteresis heating observed at the beginning of fatigue tests is a characteristic of metals. Capitalizing on this, an empirical model is developed that predicts effectively fatigue life, thus preserving testing time. Furthermore, the heat dissipated during ultrasonic cycling can be used to calculate the cyclic plastic strain amplitude [25].

1.3 VISCOELASTICITY

Viscoelasticity is a property of materials that exhibit time-dependent strain [41]. Perfectly viscous materials exhibit stress proportional to strain rate, while perfectly elastic materials feature stress proportional to strain, the proportionality constant being the elastic (or Young's) modulus. Viscoelastic materials feature intermediate characteristics between purely elastic and purely viscous behaviour, i.e. they show both behaviours when undergoing deformation.

In crystalline solids, elasticity usually involves the stretching of atomic bonds (i.e. atomic displacements) along specific crystallographic planes, whereas viscosity and viscoelasticity involve relaxations associated to diffusion. For example, this mechanism enables relaxation phenomena consisting in atomic rearrangements, large-scale cooperative motion of atomic groups, or localized atomic motion without collective atomic rearrangements or changes in chemical order [42], e.g. movements of the network itself or diffusion of a mobile species [43, 44]. Materials may exhibit viscoelastic relaxations in response to mechanical, electrical or temperature perturbations, and the relaxation processes are manifested by a transient response of physical or thermodynamic properties (e.g. enthalpy, volume, strain or stress). In any case, relaxations result in frictional energy loss appearing as heat [45].

Whether the behaviour of a material is closer to purely elastic or purely viscous depends mainly on temperature and the excitation frequency (strain rate), but it may also depend significantly on test and environmental conditions such as the pre-load, dynamic load, environmental humidity, etc [2]. To characterize the response of a material, samples are usually excited dynamically under controlled temperature, frequency and amplitude of the loading, and the strain-stress behaviour is recorded. For instance, they are often strained or stressed sinusoidally with a Dynamic-Mechanical Analyser (DMA). For an ideal elastic material, stress and strain are in phase, and the energy lost as heat per cycle is null. For an ideal viscous material, stress and strain are 90º out of phase. In reality, viscoelastic behaviour is more common. Thus, for most of the materials there is usually an intermediate phase lag between stress and strain (i.e. they are out of phase) and a certain amount of frictional energy loss (see Fig. 3). Polymers, polymer solutions and dispersions, metals and amorphous materials (organic and inorganic) are examples of materials that exhibit viscoelastic behaviour.

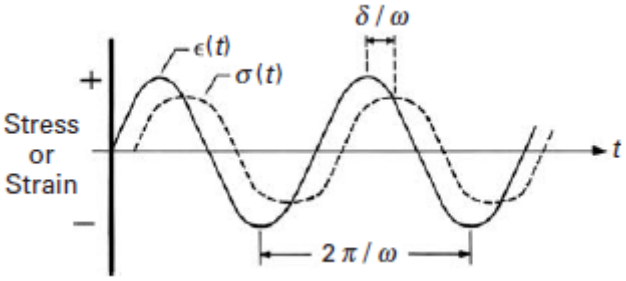

Fig. 3 Viscoelastic response of a material with phase lag between stress and strain [41] (printed with permission from Cambridge University Press).

The dynamic behaviour of linear viscoelastic materials can be described by the complex modulus approach [2]. In particular, the parameters commonly utilized for the characterization of the viscoelastic properties are the two components of the complex (or dynamic) tensile modulus, and the loss tangent[2]. The elastic (real) component of the tensile modulus is the storage modulus *E'*, which is a measure of the deformation energy stored by the material. The viscous (imaginary or plastic) component of the tensile modulus is the loss modulus *E"*, which accounts for the energy dissipation due to internal friction, i.e. the frictional energy loss, during relaxation processes [1]. Finally, the loss tangent is the ratio energy loss-to-energy stored, i.e. the ratio loss modulus-to-storage modulus (see Fig. 4).

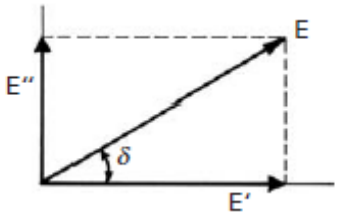

Fig. 4 Relationship between the dynamic tensile modulus *E*, the storage modulus *E'*, the loss modulus *E"* and the loss tangent *Tan δ* [41] (printed with permission from Cambridge University Press).

1.3.1 Variation of the elastic modulus of metals

In some metals and alloys, the elastic modulus shows variations which are not attributed to residual stresses, texture changes or microstructural damage [46]. Variations have been observed with:

- Cold working: The elastic modulus diminishes (e.g. around 6–10% and up to 20%) with cold working [47]. This behaviour has been reported in polycrystalline aggregates of copper [48], in carbon steels and stainless steels [49], in iron, steels and other metals and alloys [50, 51]. In some cases, the elastic modulus may recover with further cold working or may return to its original value after annealing.

[2] The loss tangent *Tan δ* is often referred to in the literature as loss factor, internal friction or mechanical damping.

- Temperature (variations should be large): The elastic constants of pure aluminium and aluminium alloys vary with temperature. Particularly, it has been observed for pure aluminium [52] and AA 2024 [53] that the elastic modulus decreases linearly with temperature from RT to 500 ºC. Deviations from this linear behaviour are reported but are only significant in the vicinity of the absolute zero.
- The crystallographic orientation (variations should be large) [46].
- The microstructure (or also, the thermal treatment): Some variations of the elastic modulus correlate to microstructural changes during thermal treatments. For instance, for AA 2024 the lowest elastic modulus value corresponds to the quenched material, while increasing the ageing time causes slight increases in the modulus (from 70.7 to 72.7 GPa) [46].
- The structure (arrangement) of dislocations: Some variations of the elastic modulus correlate to the structure of dislocations at each deformation level [46]. For example, the elastic modulus diminishes when the dislocation density increases by cold work (which agrees with what was mentioned above) or thermal treatment. It may also recover slightly with successive cold work. Nonetheless, the arrangement of dislocations should cause minimal variations in the elastic modulus of AA 2024.

1.3.2 Viscoelastic behaviour of aluminium alloys

Das [54] studied SiC particle reinforced AA 6061 matrix composites using Differential Scanning Calorimetry (DSC) and DMA[3], and compared the viscoelastic properties of these composites to those of unreinforced AA 6061, both in the as-received and T6 conditions. For these materials the storage modulus decreases with increasing temperature (see Fig. 5), and the lowest storage modulus is that of unreinforced AA 6061. The larger storage modulus of the particulate reinforced metal matrix composites is often explained in terms of the rule of mixtures, but interfacial factors and precipitation may also have an influence. It was noticed that the absolute values of the storage modulus measured at RT where lower than values reported in the literature [55-57], but the author could not find a satisfactory explanation and ignored this discrepancy. Finally, this researcher reported the loss modulus and loss tangent for the 20 vol.% SiC, AA 6061-T6 matrix composite (see Fig. 6). Unfortunately, these parameters are not reported for unreinforced AA 6061-T6.

Wolfenden [55] and Wolla [56] studied the mechanical damping and dynamic elastic modulus of alumina (Al_2O_3) fibre reinforced AA 6061 matrix composites at 80 kHz, and compared the properties of these composites to those of 99.999% pure aluminium. The temperature dependence of the dynamic elastic modulus from RT to 475 °C was measured, and it was observed a highly linear decrease with temperature (see Fig. 7). The slope was roughly the same for all the studied materials (around -80 $MPa \cdot °C^{-1}$). For one of the composites, the decrease was attributed to the reduction in the matrix modulus solely.

[3] Unfortunately, no information is provided on the tested frequencies.

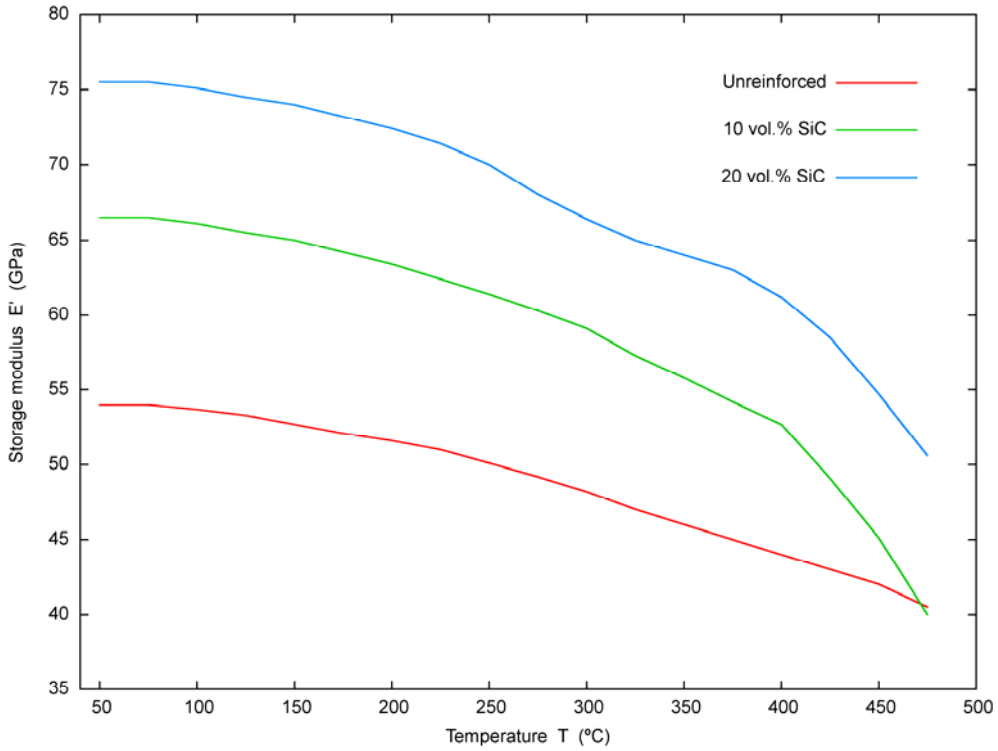

Fig. 5 Storage modulus *E'* vs. temperature *T* from DMA tests on unreinforced AA 6061-T6 and SiC particle AA 6061-T6 matrix composites, with 10 and 20 vol.% SiC [54] (printed with permission from Springer).

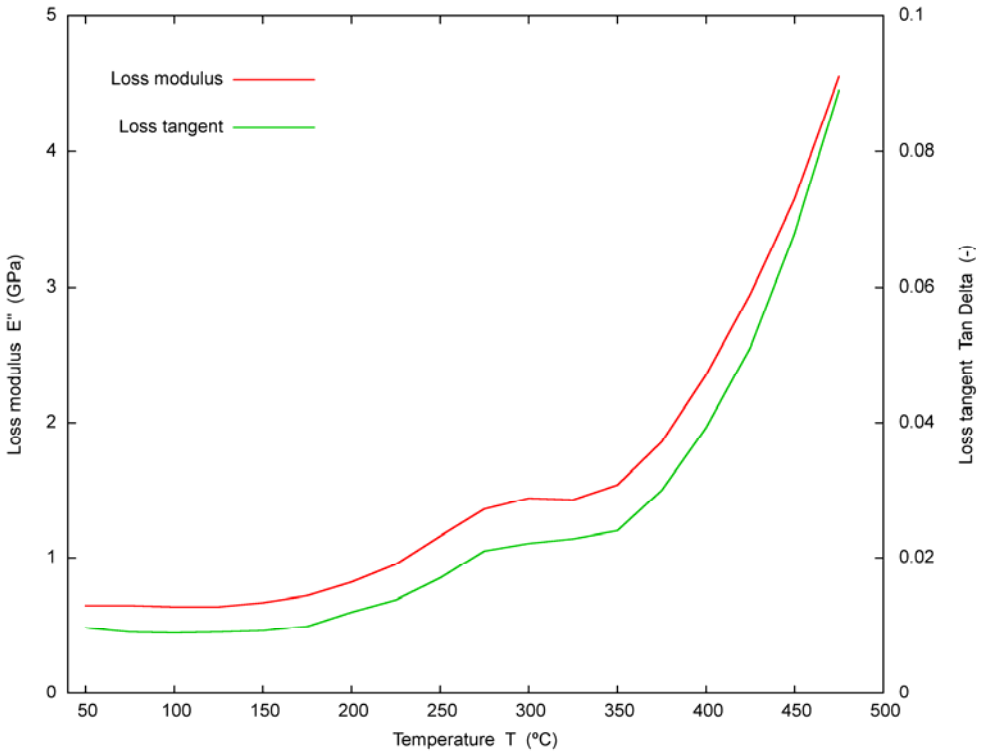

Fig. 6 Loss modulus *E''* and loss tangent *Tan δ* vs. temperature *T* from DMA tests on 20 vol.% SiC particle AA 6061-T6 matrix composite [54] (printed with permission from Springer).

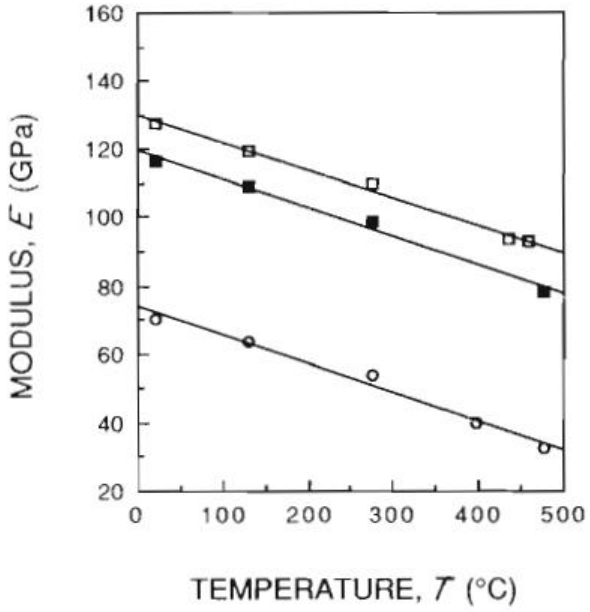

Fig. 7 Dynamic elastic modulus E vs. temperature T from Piezoelectric Ultrasonic Composite Oscillator Technique (PUCOT) tests on pure aluminium (o), and Al_2O_3 fibre AA 6061 matrix composites with 30 vol.% continuous (□) or chopped (■) fibre [55] (printed with permission from Springer).

1.4 INFLUENCE OF THE MICROSTRUCTURE ON VISCOELASTIC BEHAVIOUR

The mechanical properties of materials are intimately linked to their microstructure [5, 58], and thus the microstructure and phase transformations are reflected on the viscoelastic behaviour. Particularly, the viscoelastic response in crystalline materials may involve different types of mechanical relaxation processes, observable as internal friction peaks. The mechanism of diffusion is the physical origin of these relaxations, and they are related to a series of internal variables that depend on stress in a time-dependent manner [1]. Next we review mechanical relaxation processes associated to the microstructure in crystalline materials which are of some interest to the scope of this work:

- Point-defect relaxations.
- Relaxations related to dislocations.
- Relaxations related to grain boundaries.
- Relaxations related to phase transformations.

1.4.1 Point-defect relaxations

In this case, the relaxations are associated to the presence of elementary point defects (vacancies, substitutional atoms or interstitial atoms) or composite defects (or defect complexes) on diverse crystallographic sites of the microstructure. The presence of these defects in the crystal causes local

elastic distortions, and the mechanical relaxations arise due to interactions between the distortion stress fields of the defects and the stress applied to the crystal [1]. The migration of solute species, vacancies or solute-vacancy pairs are examples of mechanical relaxation processes involving point defects, as well as more particular cases like the Snoek relaxation and the Zener relaxation. The Snoek relaxation is due to stress-induced reordering of impurity interstitials in solution in bcc metals. The Zener relaxation is virtually a general property of substitutional solid solutions, and can be found in many alloys for all the common metallic structures, i.e. fcc, bcc and hexagonal close-packed (hcp). Basically, it is due to stress-induced reorientation of solute atom pairs in nearest-neighbour configuration [1].

1.4.2 Relaxations associated to dislocations

In this case, the relaxations are associated to the presence and displacement of dislocations, and also to the nature of the dislocation microstructure (e.g. whether we have isolated dislocations or not, etc.). Namely, relaxation phenomena are associated to the lag between the dislocation motion and the applied stress. This might occur when obstacles or potential barriers (e.g. point defects) hinder the displacement of dislocations [1]. In almost all cases, it is necessary that the material be in cold-worked or deformed state for these relaxation effects to appear. Nevertheless, internal friction due to point defects alone or due to dislocation motion interacting with point defects might also occur in deformed state materials, since their defect structure is highly complex. The Hasiguti peaks and the Snoek-Köster peak, which are attributed to dislocation motion in combination with point defects in bcc metals, and the Bordoni peak are examples of mechanical relaxation processes associated to dislocation motion. The latter is a very low-temperature internal friction peak that appears in cold-worked fcc metals. Particularly, it is attributed to the limited motion of dislocations which lie along low-energy positions [1]. Further details on relaxations associated to dislocations are presented in Annex B.

1.4.3 Relaxations associated to grain boundaries

In this case, the relaxations arise due to the occurrence of sliding at the boundaries between adjacent grains. Schematically, these processes start, upon application of stress, with the sliding of a grain over the adjacent one due to the shear stress that initially acts across their boundary. Thereby, shear stress is gradually reduced and opposing stresses build up at the end of the boundary and into other adjacent grains. This process ends when the shear stress reaches zero across most of the boundary and the grain corners sustain most of the total shearing force [1].

1.4.4 Relaxations associated to phase transformations & precipitates

Relaxation effects might also be related to phase transformations and precipitates. To explain this, it is necessary to assume first that the internal state of a material close to a transformation might be described by one or more internal order variables. Thus, some relaxations reported in materials close to the

transformation critical temperature are attributed to stress-induced changes in these order variables. Another example of this type of relaxations is the influential role that stress might play in changing the state of two-phase materials in which the formation mechanism is nucleation and growth [1]. For instance, it can be found in the literature a theory applicable to bi-phased systems of either one or two components [59, 60] and a general theory based on thermodynamics, describing the relaxation peaks caused by interface motions, with thermally-activated atomic diffusion [61].

1.4.5 Relaxations reported for AlZn & AlCu alloys & pure aluminium

AlZn alloys may exhibit high internal friction due to large scale discontinuous precipitation. This is characterized by preferential precipitation starting at grain boundaries and penetrating into grains with the decomposition of the super-saturated matrix as the interface advances. The internal friction in this case increases with temperature reaching very high values without exhibiting a peak, which may be explained by presence of coupled relaxations. In particular, the proposed mechanism consists of shear stress relaxations across the network of matrix-precipitate interfaces. Prolonged ageing at high temperatures results in internal friction reduction due to partial precipitate dissolution [1].

In opposition to the very high internal friction phenomena observed in AlZn alloys, AlCu alloys usually present low internal friction phenomena, like:

- A relaxation effect associated to atom groupings within individual clusters[4] [62].
- A Zener peak at 173–175 ºC for 1 Hz [1], observed in solution-treated and quenched samples. This peak declines as GPZ II precipitate[5], while it is stable provided the excess vacancies are removed (this can be accomplished by short annealing), since GPZ II formation only proceeds if large amounts of quenched-in vacancies are present. For these reasons, it was associated to the alloy with all the Cu in solution. The activation energy of the corresponding relaxation is 1.32±0.08 eV/atom, and the frequency factor is $10^{15.6\pm1}$ s^{-1}. However, the activation energy may change with composition.
- A broad relaxation peak at 135 ºC due to θ′ phase [1]. The nucleation and growth of θ′ precipitates modifies the internal friction behaviour:
    - It causes the appearance and growth of a peak slightly below the temperature for the Zener peak. Its magnitude is approximately proportional to θ′ phase fraction, thus declines as θ′ phase transforms into θ precipitates, and vanishes completely when no θ′ phase is present. This is why it was named the θ′ peak. Its activation energy is 0.95±0.05 eV/atom, the reciprocal of the frequency factor is $10^{-12.5\pm0.8}$ s^{-1} and its width is about 3 times larger than that for a process having a single relaxation time.

[4] The clusters the author refers to are probably GPZ or precursors of GPZ. This author does not use the term GPZ probably because by the time his work was published this nomenclature was not yet well established.
[5] The characteristic phases and precipitates of the studied alloys are described in the following sections.

  - It causes a further decline of the Zener peak, which vanishes when θ′ phase formation is complete.
- A relaxation peak associated to θ phase [63]. This relaxation has a maximum at 0.1 Hz, and disappears after annealing at 550 ºC. This is why it was associated to incoherent θ precipitates. Schoeck [64] attributes the internal friction peaks associated to incoherent phases to their viscous boundaries. More recently, to explain the fact that this relaxation is not thermally activated, it was suggested that phase transformation occurs at the precipitate-matrix interface with applied strain but without the need for long-range atomic diffusion [65].

Furthermore, AlZnMg alloys, AlCuMg alloys and pure aluminium may exhibit relaxation peaks associated to dislocations [66, 67] and to grain boundaries. For example, dislocation motions explain some internal friction peaks associated to semi-coherent precipitates [68], and also the Bordoni peak, which has been extensively studied in cold-worked pure aluminium [1]. Finally, polycrystalline aluminium presents a peak related to grain boundaries at about 300 ºC for 1 Hz [1].

1.5 AGEING PATHS OF AlZnMg & AlCuMg ALLOYS

As mentioned in Section 1.1.4, the precipitation path resulting from the decomposition of the metastable SSS determines the microstructure and the material properties. This is the reason why appreciable research efforts have been focused on the investigation of the transformation sequence during ageing in metals. This research has been particularly intense in AlZnMg alloys [69] and in AlCuMg alloys because of their commercial and industrial importance.

1.5.1 Ageing path of AlZnMg alloys

For the alloys of the family AlZnMg, it is normally accepted that the age-hardening mechanism is based on the following ageing sequence [16, 69-72]:

- α_{SSS} – GPZ I – GPZ II – η’ – η

where GPZ are Zn/Mg solute-rich coherent clusters named Guinier-Preston Zones, η’ the semi-coherent metastable $MgZn_2$ phase and η the incoherent stable (equilibrium) $MgZn_2$ phase. Nevertheless, it has also been suggested that in AlZnMg alloys a precipitation sequence involving GPZ I and another involving GPZ II might evolve in parallel [69].

1.5.2 Ageing path of AlCuMg alloys

For the alloys of the family AlCuMg, it is normally accepted that the age-hardening mechanism is based essentially on two different ageing sequences [8, 9, 72-75]:

- α_{SSS} – GPZ I – GPZ II (θ”) – θ' – θ
- α_{SSS} – GPBZ – (S”) – S' – S

where GPZ are Cu solute-rich coherent clusters named also Guinier-Preston Zones, θ” and θ' the semi-coherent metastable Al_2Cu phases, θ the incoherent stable (equilibrium) Al_2Cu phase, GPBZ the Cu/Mg coherent clusters named Guinier-Preston-Bagariastkij Zones, S” and S' the semi-coherent metastable Al_2CuMg phases and S the incoherent stable (equilibrium) Al_2CuMg phase. The existence of an intermediate phase S” between GPBZ and S’ is still controversial, though [8].

Decomposition of the SSS occurs along either one or both paths depending on the Cu:Mg ratio. The AA 2024-T3 studied in the present work contains 4.46 wt.% Cu and 1.35 wt.% Mg. For this Cu:Mg ratio and in view of the AlCuMg phase diagram [75, 76], ageing of this alloy should involve both precipitation paths, leading finally to formation of both θ and S phases. This has been indeed confirmed by electron microscopy [75] and DSC, Transmission Electron Microscopy (TEM) and Selected Area Electron Diffraction (SAED) investigations [77].

Finally, in the case of AlCuMgZn alloys, apart from the latter two precipitation sequences, that of AlZnMg may be present too. There are no indications so far of interactions between these three different sequences which apparently develop independently [74].

1.6 PHASES & TRANSFORMATIONS IN THE AGEING PATH OF AlZnMg ALLOYS

In this section, we summarize some of the findings on the precipitates in the ageing sequence of AlZnMg alloys, their size and shape, and the characteristic temperatures for the respective phase transformations.

1.6.1 Summary of sizes & shapes of precipitates

Table 5 summarizes the reported sizes and shapes for the precipitates present in AlZnMg alloys.

Table 5 Sizes and shapes of the precipitates in the ageing sequence of AlZnMg alloys.

Precipitate type	Size[a] [nm]	Shape	Reference
GPZ	Diameter: 0.5–1	Spheres	[79]
	Diameter: 1.5–16	Spheres	[80]
	Diameter: 2.5	Spheres	[81]
	Less than 7.5	Spheres	[82]
	Radius: a few nm	Spheres	[16]
	Diameter: 2–3	GPZ I and II are spheres	[69, 83]
		Discs	[84]
		Spheres and ellipsoids	[85]
		Spheres	[86]
	1.5 (at 160ºC)	Spheres	[80]
		Spheres (GPZ I)	[87]
η' phase	12.5		[82]
	Width: 5.8–7.3	Platelets	[79]
	Width: 5–10; Aspect ratio: 1.5–2.5	Platelets[b]	[69]
	15	Platelets or rods	[80]
	5–10		[87]
η phase	Width: 5.8–7.3	Platelets	[79]
	Width: 5–10; Aspect ratio: 1.5–2.5	Rods	[69]
Unidentified	Max. diameter: 5	Platelets	[88]
	Width: 2; radius: 2.5–5		[87]
		Spheres	[89]

[a] The particle size may increase (due to coarsening) with heat-treatment time.
[b] This researcher also reports that η' and η particles do not deviate largely from spheres and therefore may be treated roughly as spherical for some purposes.

1.6.2 Guinier-Preston Zones (GPZ)

The first stage in the ageing sequence of AlZnMg alloys is the formation of GPZ, which are coherent segregates of Zn and Mg atoms. Hansen [87] claims that there is a lack of established, complete structure models for these and other phases in AlZnMg alloys, except for the η phase [90], so he proposed new models for the η phase and GPZ. In particular, GPZ I are segregates internally ordered on {100} aluminium matrix planes, while GPZ II are thin (a few atoms thick) Zn-enriched structures ordered on {111} planes [69, 87, 91]. GPZ II form by segregation of Zn, but only when there is high super-saturation of quenched-in vacancies, and grow by incorporation of Mg [87].

GPZ nucleate mainly at dislocations and grain boundaries [86], and vacancy-rich clusters [87]. Site saturation is likely to occur before growth [86]. Generally, the rate-limiting factor in a precipitation process in the solid state, at low temperatures, is the diffusion of the slowest solute species that contributes to the process. In this case, it is Mg [16]. GPZ may grow in size as temperature increases [80] or grow during ageing even at RT. For example, the third power of GPZ diameter is proportional to time during ageing at RT up to three hours (i.e. the volume increases linearly with time). Ferragut [16] affirms that GPZ grow until coherence with the aluminium matrix becomes energetically unfavourable [16]. Then, GPZ become unstable and transform into η' precipitate. Likewise, other researchers reported that GPZ II transform into

η' phase, and subsequently into η phase [83, 87]. As per GPZ I, Engdahl [69] concluded that these structures are less stable and dissolve as temperature increases.

Finally, it is worth to note the research already performed on the role of GPZ on hardening. Some investigations pointed that hardening is proportional to the volume of GPZ [81, 86]. Macchi [70] reports that the GPZ, on the one side, and the semi-coherent and incoherent precipitates, on the other side, are in competition to control the hardening effects and that the level of hardening will thus depend on, among other parameters, the relative hardening associated to each phase. He obtained the maximum hardening when the microstructure consisted of GPZ mainly. However, Ferragut [16] claims that the η' particles are more effective in hindering the motion of dislocations and thus are the main responsible for the hardening.

1.6.3 Intermediate η' phase

The second stage in the ageing sequence of AlZnMg alloys is the formation of η' phase. Traditionally it has been accepted that the η' phase consists of semi-coherent metastable hexagonal $MgZn_2$ precipitates. However, according to a more recent structural model [69, 92], the composition is $Mg_2Zn_{(5-x)}Al_{(2+x)}$. This indicates that Al atoms may occupy some of the Zn sites. Although it has been usually accepted that η' phase nucleates from, or at sites of GPZ, or at dislocations [16], other researchers suggest that this may not necessarily be so [70, 93]. In any case, quenched-in vacancies may play an essential role in this process [69]. Hansen [87] states that η' phase forms from GPZ II through a gradual change in internal order and composition, as more layers are added.

There is an orientation relationship between the aluminium matrix and the η' phase. For instance, Graf [80] affirms that η' precipitates appear oriented parallel to {111} aluminium matrix planes. More recently, High-Resolution Electron Microscopy (HREM) analyses [69, 92] showed that the c-axis[6] of the hexagonal η' cell fits to {111} planes. HREM analyses also revealed a variation in the structure from the centre towards the edge of η' particles [92]. A gradual change of composition in the form of a radial gradient is suggested. This is supported by 3-Dimensional Atom Probe (3DAP) studies [69], showing that the aluminium content decreases towards the centre while solute concentration is higher at the centre.

1.6.4 Equilibrium η phase

The third stage in the ageing sequence of AlZnMg alloys is the formation of the stable (equilibrium) η phase, which consists of incoherent hexagonal $MgZn_2$ precipitates. This phase forms from η' phase by coarsening of η' precipitates (e.g. expansion in the basal plane) and a collapse from 6 layers to 4 along the hexagonal cell c-axis [87]. Phases η' and η have similar chemistry, i.e. there is no substantial composition change. Also, although the total amount of solute in η' particles is smaller than in η particles,

[6] The c-axis corresponds to the edges of the hexagonal cell that are perpendicular to the hexagonal faces.

the Zn:Mg ratio is similar for both, and it is not possible to differentiate between individual precipitates on the basis of these ratio [69, 83].

1.6.5 Characteristic temperatures for phase transformations

Tables 6 and 7 summarize (in a numerical and qualitative manner, respectively) the characteristic temperatures reported for the phase transformations in the precipitation sequences of AlZnMg alloys.

Table 6 Characteristic temperatures for transformations in ageing sequence of AlZnMg alloys.

Transformation	Temperature[a]	Heating rate[a]	Reference
GPZ formation	At RT		[70, 80, 87]
	At 77 ºC	**5**, 10, 20, 40, 60 ºC/min	[94]
	From RT to 70 ºC	10 ºC/min	[71]
GPZ dissolution	Above 100ºC		[87]
	At 190 ºC	10 ºC/min	[71, 95]
	At 200 ºC	15 ºC/min	[78]
	From 100 to 150 ºC	**1**, 5, 10, 20 ºC/min	[84]
	From 100 to 217 ºC	5, 10, 20 ºC/min	[96]
	From 130 to 219 ºC	10, 15 ºC/min	[82]
η' formation	At 189 ºC	**5**, 10, 20, 40, 60 ºC/min	[94]
	At 230 ºC	10 ºC/min	[71, 95]
	At 250 ºC	3–20 ºC/min	[86]
	From 100 to 200 ºC		[16]
	From 217 to 271 ºC	5, 10, 20 ºC/min	[96]
	From 219 to 306 ºC	10, 15 ºC/min	[82]
η' dissolution	At 257 ºC	10 ºC/min	[71]
η formation	At 219 ºC	**5**, 10, 20, 40, 60 ºC/min	[94]
	At 230 ºC	10 ºC/min	[71]
	At 240 and 300 ºC	15 ºC/min	[78]
	At 260 ºC	10 ºC/min	[84]
	From 219 to 306 ºC	10, 15 ºC/min	[82]
η dissolution	Above 257 ºC	10 ºC/min	[71]
	From 271 to 448ºC	5, 10, 20 ºC/min	[96]
	From 300 to 450 ºC	**1**, 5, 10, 20 ºC/min	[84]

[a] The temperatures reported in this table may correspond to peak or start-to-end temperatures obtained after DSC scans, and thus they may vary with particle size and/or heating rate. When data for several heating rates were available, priority was given to data for the closest heating rate to that we used for the DMA tests, i.e. approximately 1 ºC/min. When known, the heating rate corresponding to the presented data appears in bold letters.

Table 7 Characteristic temperatures for transformations in ageing sequence of AlZnMg alloys. The grey levels are proportional to the number of references reporting each transformation at the corresponding temperature.

	25 °C	50 °C	75 °C	100 °C	125 °C	150 °C	175 °C	200 °C	225 °C	250 °C	275 °C	300 °C	325 °C	350 °C	375 °C	400 °C	425 °C	450 °C
GPZ formation																		
GPZ dissolution																		
η' formation																		
η' dissolution																		
η formation																		
η dissolution																		

1.7 PHASES & TRANSFORMATIONS IN THE AGEING PATH OF AlCuMg ALLOYS

In this section, we summarize some of the findings on the precipitates in the ageing sequence of AlCuMg alloys, their size and shape, and the characteristic temperatures for the respective phase transformations.

1.7.1 Summary of sizes & shapes of precipitates

Table 8 summarizes the reported sizes and shapes for the precipitates present in AlCuMg alloys.

Table 8 Sizes and shapes of the precipitates in the ageing sequence of AlCuMg alloys.

Precipitate type	Size[a] [nm]	Shape	Reference
GPZ	Diameter: 2–10	GPZ I are discs[b]	[72]
	From 8–15 to 50		[8]
GPBZ	Width: 421; thickness: 0.2	Platelets	[77]
	From 8–15 to 50		[8]
		Cylinders	[97]
		Cylinders	[9]
	Length: 10–20; Diameter: 1–3	Rods	[76]
θ" phase	20 or more		[72]
θ' phase	Length: 500–5000	Platelets	[1, 98]
		Discs	[84, 99]
θ phase	–	–	–
S" phase	–	–	–
S' phase		Rods	[100]
S phase	Diameter: 5–18 (fine)		[101]
	Diameter: 40–80 (coarse)		[101]
		Laths	[76]

[a] The particle size may increase (due to coarsening) with heat-treatment time.
[b] This shape minimizes the strain energy, according to the author.

1.7.2 Guinier-Preston Zones (GPZ)

The first stage in the θ-phase based ageing sequence of AlCuMg alloys is the formation of GPZ, which are coherent segregates of Cu atoms. To form, this phase needs a sufficient concentration of excess vacancies [98], and the formation rate increases with the excess vacancies concentration [9]. They seem to nucleate on dislocations and also to precipitate homogeneously inside grains, and are accompanied by intense strain fields [8]. It has been suggested that GPZ II may grow by a layer-by-layer mechanism, and also that GPZ I transform into GPZ II, but controversy still exists as to the mechanism by which this transformation occurs as temperature increases [72]. In particular:

- GPZ I may be:
  - single-layered coherent precipitates parallel to the {100} matrix planes [102-104]; or
  - multi-layered precipitates [105-109].
- GPZ II may be (see Fig. 8):
  - a slightly modified (multi-layered) form of (predominantly single-layered) GPZ I or of a different phase. In the latter case the designation θ" would be preferred [72];
  - tetragonal structures formed by layers in a Al:(Al, Cu):Cu:(Al, Cu):Al sequence [102];
  - single Cu layers separated by three aluminium layers [110, 111];
  - two Cu layers separated by a single aluminium layer; or
  - other complex structures [105, 107].

1.7.3 Intermediate θ" phase

It has been generally accepted that the θ" phase consists of semi-coherent metastable Al_2Cu precipitates. Nevertheless, Konno [72] states that θ" phase is the designation reserved for a particular case of GPZ II, in AlCuMg alloys.

1.7.4 Intermediate θ' phase

The θ' phase consists also of semi-coherent metastable Al_2Cu precipitates. They nucleate at dislocations [112] or on the faces of GPZ II [72], particularly on the {100} planes of the aluminium matrix, with which form a coherent interface [1]. The growth kinetics of θ' precipitates (both for thickening and lengthening) are controlled by diffusion and by the interface (which is ultimately controlled by diffusion, too) [99].

1.7.5 Equilibrium θ phase

The last stage in the θ-phase based ageing sequence of AlCuMg alloys is the stable (equilibrium) θ phase, consisting of incoherent Al_2Cu precipitates, which may have body centred tetragonal structure, or a complex tetragonal structure [1].

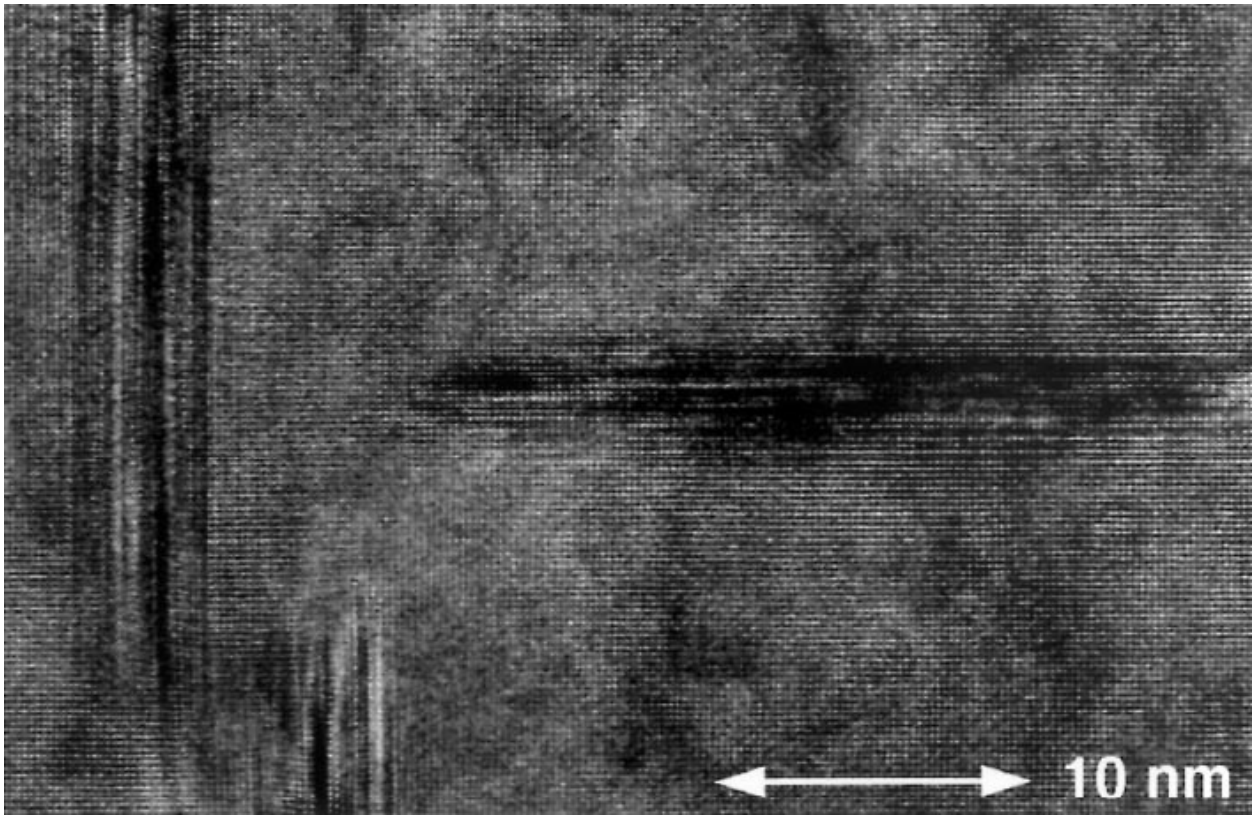

Fig. 8 Micrograph of an AlCu alloy aged at 180 ºC for 48h, obtained by High-Resolution Transmission Electron Microscopy (HRTEM). GPZ II parallel to {100} matrix planes are shown [72] (printed with permission from Oxford University Press).

1.7.6 Guinier-Preston-Bagariastkij Zones (GPBZ)

The first stage in the S-phase based ageing sequence of AlCuMg alloys is the formation of GPBZ, which consist of thin (even single-layered), coherent Cu/Mg precipitates ordered on {001} aluminium matrix planes [77]. They appear by a nucleation and growth process. Particularly, during ageing, GPBZ form from, or nucleate at, the sites of Cu-Mg co-clusters [76], and grow by quenched-in vacancy aided diffusion of solutes [9], becoming finely dispersed throughout the grains. Research suggests that the slower Cu atom diffusion may control GPBZ formation, but also that the kinetics of this transformation depends on the excess vacancy concentration [101].

The GPBZ radius was reported to be proportional to the square root of time [9], provided that nucleation takes place at the early stages of GPBZ precipitation and growth of the particles is controlled by diffusion. Nevertheless, GPBZ are difficult to detect even at high magnification due to their small size. Finally, Dixit [101] stated that GPBZ are the major strengthening phase in AA 2024-T3.

1.7.7 Intermediate S” phase

The S” phase consists of semi-coherent metastable Al_2CuMg precipitates. Charai [77] observed monoclinic S″ precipitates by HREM in samples aged at temperatures around 200°C. However, the existence of this phase is still a controversial issue [8].

1.7.8 Intermediate S’ phase

The S' phase consists also of semi-coherent metastable Al_2CuMg precipitates. Charai [77] observed orthorhombic S’ precipitates by HREM in samples aged at around 200°C. It has been suggested that Cu/Mg clusters may constitute nuclei for homogeneous S′ formation, and that S’ phase may precipitate heterogeneously on dislocations [77], too. Finally, formation of S’ phase is attributed to linear axial growth or radial growth controlled by diffusion [9].

1.7.9 Equilibrium S phase

The last stage in the S-phase based ageing sequence of AlCuMg alloys is the stable (equilibrium) S phase, consisting of incoherent Al_2CuMg precipitates. These precipitates nucleate heterogeneously on dislocation lines and have been reported to be homogenously distributed throughout the matrix. Apparently, they have little or no significant influence on hardening [76].

1.7.10 Characteristic temperatures for phase transformations

Tables 9 and 10 summarize (in a numerical and qualitative manner, respectively) the characteristic temperatures reported for the phase transformations in the precipitation sequences of AlCuMg alloys.

Table 9 Characteristic temperatures for transformations in ageing sequence of AlCuMg alloys.

Transformation	Temperature[a]	Heating rate[a]	Reference
GPZ/GPBZ formation	At RT	In general, 20 ºC/min	[77]
	At RT and at 74 ºC	0.5, **2**, 5, 20, 40 ºC/min	[98]
	At RT and at 75–80 ºC	20 ºC/min	[8]
	At 75 ºC	**5**, 10, 15, 20 ºC/min	[9]
	At 80 ºC	10 ºC/min	[113]
	At 90 ºC	2, 5, 10, 20, 30, 50 ºC/min	[75]
GPZ/GPBZ dissolution	At 120 ºC	20 ºC/min	[8]
	At 200 ºC	**5**, 10, 15, 20 ºC/min	[9]
	At 200 ºC	10 ºC/min	[113]
	From 100 to 170 ºC	**1**, 5, 10, 20 ºC/min	[84]
	From 120 to 280 ºC	In general, 20 ºC/min	[77]
	From 137 to 247 ºC		GPZ I [114]
	From 140 to 240 ºC	0.5, **2**, 5, 20, 40 ºC/min	[98]
	From 150 to 250 ºC	10 ºC/min	[101]
	From 150 to 250 ºC	20 ºC/min	[115]
	From 170 to 224 ºC	2, 5, 10, 20, 30, 50 ºC/min	[75]
	From 187 to 297 ºC		GPZ II [114]
θ” formation	–	–	No references were found
θ” dissolution	–	–	No references were found
θ’ formation	At 286 ºC	2, 5, 10, 20, 30, 50 ºC/min	[75]
	At 313 ºC	0.5, **2**, 5, 20, 40 ºC/min	[98]
	From 200 to 270 ºC	**1**, 5, 10, 20 ºC/min	[84]
θ’ dissolution	At 390 ºC	0.5, 2, **5**, 20, 40 ºC/min	[98]
	From 300 to 550 ºC	**1**, 5, 10, 20 ºC/min	[84]
θ formation	At 306 ºC	2, 5, 10, 20, 30, 50 ºC/min	[75]
	At 313 ºC	0.5, **2**, 5, 20, 40 ºC/min	[98]
	From 400 to 450 ºC	**1**, 5, 10, 20 ºC/min	[84]
θ dissolution	At 470 ºC	0.5, 2, **5**, 20, 40 ºC/min	[98]
	From 300 to 550 ºC	**1**, 5, 10, 20 ºC/min	[84]
S” formation	At 235 ºC	In general, 20 ºC/min	[77]
	From 120 to 280 ºC	In general, 20 ºC/min	[77]
S” dissolution	At 250 ºC	10 ºC/min	[113]
S’ formation	At 270 ºC	**5**, 10, 15, 20 ºC/min	[9]
	At 286 ºC	2, 5, 10, 20, 30, 50 ºC/min	[75]
	At 300 ºC	10 ºC/min	[113]
	From 120 to 280 ºC	In general, 20 ºC/min	[77]
	From 250 to 350 ºC	10 ºC/min	[101]
S’ dissolution	Above 350 ºC	In general, 20 ºC/min	[77]
	At 365 ºC	**5**, 10, 15, 20 ºC/min	[9]
S formation	At 300 ºC	10 ºC/min	[113]
	From 250 to 320 ºC	20 ºC/min	[115]
	From 250 to 350 ºC	10 ºC/min	[101]
	From 280 to 350 ºC	In general, 20 ºC/min	[77]
S dissolution	Above 350 ºC	In general, 20 ºC/min	[77]
	At 450 ºC	10 ºC/min	[113]
	From 320 to 470 ºC	20 ºC/min	[115]

[a] The temperatures reported in this table may correspond to peak or start-to-end temperatures obtained after DSC scans, and thus they may vary with particle size and/or heating rate. When data for several heating rates were

available, priority was given to data for the closest heating rate to that we used for the DMA tests, i.e. approximately 1 ºC/min. When known, the heating rate corresponding to the presented data appears in bold letters.

Table 10 Characteristic temperatures for transformations in ageing sequence of AlCuMg alloys. The grey levels are proportional to the number of references reporting each transformation at the corresponding temperature.

	25 °C	50 °C	75 °C	100 °C	125 °C	150 °C	175 °C	200 °C	225 °C	250 °C	275 °C	300 °C	325 °C	350 °C	375 °C	400 °C	425 °C	450 °C
GPZ/GPBZ formation																		
GPZ/GPBZ dissolution																		
θ” formation																		
θ” dissolution																		
θ’ formation																		
θ’ dissolution																		
θ formation																		
θ dissolution																		
S” formation																		
S” dissolution																		
S’ formation																		
S’ dissolution																		
S formation																		
S dissolution																		

1.8 DENSITIES & CONCENTRATIONS OF PARTICLES

The concentrations of GPZ/GPBZ and metastable and equilibrium precipitates in AlZnMg and AlCuMg alloys may vary with the alloy type and with the heat-treatment time or temperature. That being said, for AA 7075-T6, Sharma [79] measured an overall surface density of particles of 4×10^4 per μ^2, in average. De Sanctis [88] obtained similar results previously. This author measured particles in excess of 4×10^4 per μ^2 for a commercial AlZnMg alloy. Park [89] reported a surface density of 10^3 particles per μ^2 after conducting TEM investigations on commercial AA 7075-T6. Hansen [87] obtained overall volume particle densities ranging from 10^6 to 3×10^6 particles per μ^3 after TEM and atom probe analyses of precipitates in AA 7108. Finally, Dixit [101] reported GPBZ volume fractions within the range 0.4–3.2% and S phase volume fractions within the range 0.7–3.8%. The total combined volume fraction of precipitates is reported to fall within the range 3.9–5.2%.

1.9 PHASE TRANSFORMATION KINETICS

In this section, we describe the kinetics of phase transformations that are of interest to the scope of this research. In phase transformations, thermodynamic effects, kinetic effects and mass transport usually

appear interrelated [116]. Namely, the extent of a transformation at any given temperature is controlled either by kinetics or by temperature dependent thermodynamic equilibrium[7] [84]. We shall be concerned principally with nucleation and growth reactions, which are possible in metastable phases. These are heterogeneous transformations for which the new phase grows in detriment of the old one by migration of an inter-phase boundary [117]. Growth occurs through an atomic transfer process across this boundary. For a recent review of the state of the art on this subject, the reader is referred to Liu's work [118].

1.9.1 Modelling of phase transformation kinetics of AlZnMg & AlCuMg alloys

Significant research has been devoted to the study and modelling of thermodynamic and kinetic effects in phase transformations of the ageing paths of AlZnMg and AlCuMg alloys. In particular, several types of rate equations have been proposed that establish the time-evolution of the transformed fraction during the corresponding transformation. For instance, the Johnson-Mehl-Avrami-Kolmogorov (JMAK) model is commonly used to describe the kinetics of nucleation and growth transformations, where the formation of a new phase typically follows a sigmoidal curve [116, 117, 119]. This equation can be stated as:

$$\frac{C(t)}{C_{final}} = 1 - \exp(-(t/\tau)^n) \qquad \text{Eq. 1}$$

where the term on the left hand side of this equation is the transformed fraction, t is time, τ is the characteristic transformation time and n is the Avrami exponent. The transformation time is determined by the activation energy and the transformation temperature, and thus will decrease as the transformation temperature increases. The Avrami exponent depends on the nature of the nucleation process (continuous or site saturated) and growth process (2D or 3D, interface or diffusion controlled) [117]. It is noteworthy that the Avrami model relates only to kinetics and stems simply from geometrical considerations (i.e. the rate of occupation of the space by the new phase), and its application does not require any assumption or consideration regarding the thermodynamics of the transformation. Finally, the classical definition of the Avrami exponent is only adequate if the driving mechanisms do not vary during the transformation process [120].

From Differential Isothermal Calorimetry (DIC) scans, Smith [73] obtained information on the kinetics of phase transformations of AA 2124 using a 2-exponential fit and a rate-averaged time constant. However, GPZ formation was best fitted to a JMAK kinetics model [73].

[7] Thermodynamics are always the reason behind any transformation, but in some cases kinetics phenomena (e.g. diffusion) play a key role on top of thermodynamics. The latter transformations are considered to be "kinetically controlled", while the rest are "thermodynamically controlled". As per the temperature-dependent behaviour, kinetic effects associated to enthalpy changes are more likely to dominate at lower temperatures, while thermodynamic effects associated to entropy changes are more likely to dominate at higher temperatures [116].

Papazian [84] studied GPZ dissolution for AA 2219 and AA 7075. Experimental DSC data was fitted to a 3D volume diffusion limited rate expression, Eq. 2, and a first order diffusion expression, Eq. 3:

$$\left[1-(1-\frac{C_1}{C_{initial}})^{1/3}\right]^2=\frac{k_0E_A}{K\phi}\int_{\frac{E_A}{KT}}^{\infty}\frac{e^{-x}}{x^2}dx \qquad \text{Eq. 2}$$

$$-\ln(1-\frac{C_1}{C_{initial}})=\frac{k_0E_A}{K\phi}\int_{\frac{E_A}{KT}}^{\infty}\frac{e^{-x}}{x^2}dx \qquad \text{Eq. 3}$$

where k_0 is a pre-exponential coefficient, E_A is the activation energy (assumed to be constant), K is the Boltzmann constant, Φ is the DSC heating rate and T is temperature. For AA 2219 aged at low temperature, Papazian concluded that GPZ dissolution is best described by the 3D volume diffusion limited rate expression, Eq. 2. For AA 7075 aged 6 months at RT, and AA 7075-T651, Papazian concluded that the GPZ dissolution in AA 7075 is best described also by the 3D volume diffusion limited rate expression, Eq. 2.

The rate of formation of θ' is best described by an Avrami expression with n = 1.1 [84]. S' formation has also been modelled using the Avrami equation with n = 1.0 [75]. For η' phase formation and growth in as-quenched specimens and aged specimens, the Avrami index has been estimated to be about 2.3–2.8 (±20%) [86].

Alternative expressions for modelling the transformation kinetics are also reported in the literature. For instance, assuming that the particular phase transformation is a temperature- or thermally-activated process, concentration of the species may follow the Arrhenius behaviour. In this case, the transformation rate equation is [9, 117]:

$$\frac{d\left(C/C_{final}\right)}{dt}=f(\frac{C}{C_{final}})k_0\exp\left(-\frac{E_A}{KT}\right) \qquad \text{Eq. 4}$$

Jena [9] states that precipitation reactions that occur by nucleation and growth yield sigmoidal behaviour and are best described either by the Avrami model, Eq. 1, or by Eq. 4 when:

$$f(\frac{C}{C_{final}})=\left(\frac{C}{C_{final}}\right)^r\left(1-\frac{C}{C_{final}}\right)^m \qquad \text{Eq. 5}$$

where coefficients r and m are constants. Jena [9] reported the best fit values of r, m, k_0 and E_A for several phase transformations in the precipitation sequences of the AlCuMg family, namely GPBZ precipitation, GPZ dissolution, dissolution of GPBZ-dislocation complexes and S' precipitation. A good fit to a JMAK model with n = 1.0 was also obtained for the latter transformation. Though the model by Jena combines kinetics and thermodynamics considerations, its physical basis is not described. Finally,

Yannacopoulos [86] applied a rate expression based on chemical reactions obeying an m-order Eyring rate to formation and dissolution of GPZ, as well as to formation of other precipitates. The activation energies were calculated via the Kissinger method, which is valid for transformations involving a single precipitation process during heating at constant heating rate [121].

1.9.2 Kinetic parameters for phase transformations in AA 7075

A summary of the values found in the literature for the kinetic parameters of the phase transformations involved in the precipitation path (ageing sequence) of AA 7075 is presented in this section. For some of the transformation processes no information was found in the literature regarding the kinetics and/or activation energies. The possible causes for the absence of literature reporting on these issues are:

- The calculation of the activation energy is not possible due to a particular reason, e.g. in DSC scans, when the peak corresponding to the particular phase transformation is overlapped [84].
- The corresponding phase transformation is thermodynamically controlled, so the kinetic factors are not important [9].
- No researcher has analysed the kinetics of the particular transformation for AA 7075 (or for AA 2024) to the author's knowledge. In some cases, information on activation energies of other AlZnMg (or AlCuMg) alloys is presented instead, when available.

Next follows a summary of the findings on kinetic parameters for AA 7075:

1. GPZ formation:
    a. For Zergal 4[8] the activation energy for the reconstruction of GPZ is in the range 0.59-0.67 eV/atom [16].
    b. For AlZnMgZr alloy the (isothermal) activation energy is reported to be 0.35 eV/atom when using a method based on hot micro-hardness data, and 0.75 eV/atom when using data from variable heating rate DSC scans [86]. In this paper, other values are reported too from previous DSC studies: 0.41 eV/atom [122], 0.67 eV/atom [123], and 0.65–1.08 eV/atom.
2. GPZ dissolution[9]:
    a. Reported activation energies are [82]:
        i. For AA 7075-T6: 135000 J/mole (1.40 eV/atom).
        ii. For AA 7075-T6 followed by Retrogression and Re-ageing (RRA): 145000 J/mole (1.50 eV/atom).
        iii. For AA 7075-T85: 150000 J/mole (1.55 eV/atom).

[8] Zergal 4 is a commercial AlZnMgCu alloy, with composition Al–6.0 wt.% Zn–2.0 wt.% Mg–1.0 wt.% Cu.
[9] The activation energies for GPZ formation and for GPZ dissolution are expected to be different. In the GPZ formation process there is an excess of solute while in the dissolution process there is a lack of solute. Nevertheless, both processes are related to atomic mobility of the same species, thus their activation energies should be of a similar order of magnitude.

   b. For Zergal 4, for GPZ dissolution and simultaneous η' formation, i.e. transformation GPZ-η', the activation energy is 0.32 eV/atom [16, 124].
   c. For AA 7075 aged 6 months at RT and for AA 7075-T651, the activation energies using a first order diffusion expression and a 3D volume diffusion limited rate expression were 75000 J/mole (0.78 eV/atom) and 123000 J/mole (1.27 eV/atom), respectively [84].
   d. Reported activation energies are [86, 96]:
      i. For AA 7075 naturally aged: 0.93-0.99 eV/atom.
      ii. For AA 7075-T6: 1.23 eV/atom.
      iii. For AA 7091: 0.99 eV/atom.
   e. For AlZnMgZr alloy the (isothermal) activation energy is reported to be 0.92 eV/atom when using data from variable heating rate DSC scans [86].
3. η' formation:
   a. For AlZnMgZr alloy the activation energy for η' formation and growth for as-quenched specimens and aged specimens is reported to be 0.57, 0.59 and 0.62 eV/atom [86]. The Avrami expression with n = 2.3–2.8 was used.
   b. It is difficult to find references that report kinetic parameters for this phase transformation. The reason is that, although it is kinetically controlled, the precipitation of η' is not good for kinetics analysis since its peak in DSC thermograms appears overlapped with those of η' dissolution and η formation, as occurs for AA 7075 [84].
4. η' dissolution: No references have been found that report kinetic parameters for this phase transformation. The reason is the same as for η' formation [84].
5. η formation: No references have been found that report kinetic parameters for this phase transformation. The reason is the same as for η' formation [84].
6. η dissolution: No references have been found that report kinetic parameters for this phase transformation. The reason is that η dissolution is controlled by thermodynamics, so the kinetic factors are not important in this case [9, 84].

1.9.3 Kinetic parameters for phase transformations in AA 2024

Analogously, next follows a summary of the literature data on kinetic parameters for AA 2024:

1. GPZ or GPBZ formation:
   a. For an AlCuMg alloy, the activation energy of GPBZ formation is 52300–55600 J/mole (0.54-0.58 eV/atom) or 64000 J/mole (0.66 eV/atom), and the pre-exponential coefficient is 5.7×10^{5} s^{-1}. These results were obtained from resistivity measurements by Jena [9], using Eq. 4 and Eq. 5, where r = 0 and m = 1. The latter values agree with what is expected if nucleation occurs at the early stages of GPBZ precipitation and particle radius increases by diffusion controlled growth.

   b. For AA 2124, the activation energy is reported to be 73300 J/mole (0.76 eV/atom) when using DSC data, and 76200 J/mole (0.79 eV/atom) when analyzing DIC data [73]. Hence, activation energies from DSC and DIC agree fairly well.
   c. For an AlCuMg alloy, the activation energy of GPBZ formation is 67000 J/mole (0.69 eV/atom) [77]. Charai reports also values from other researchers: 65000 J/mole (0.67 eV/atom).

2. GPZ or GPBZ dissolution:
   a. For GPBZ dissolution in AlCuMg alloy the activation energy is 123900 J/mole (1.28 eV/atom), and the pre-exponential coefficient is 1.1×10^{10} s^{-1} [9].
   b. For AA 2219-T31 and AA 2219 aged at low temperature, the activation energies using a first order diffusion expression and a 3D volume diffusion limited rate expression were 79500 J/mole (0.82 eV/atom) and 126000 J/mole (1.31 eV/atom), respectively [84].
   c. For AA 2124, the activation energy is 159900 J/mole (1.66 eV/atom) [73].
3. θ" formation:
   a. For AlCu alloys (AA 2024 and AA 2618) the activation energy is 129000 J/mole (1.34 eV/atom) [75].
   b. For AA 2124, the activation energy is reported to be 131000 J/mole (1.36 eV/atom) when using DSC data, and 128000 J/mole (1.33 eV/atom) when analyzing DIC data [73].
4. θ" dissolution: No references have been found that report kinetic parameters for this phase transformation.
5. θ' formation:
   a. For AlCu alloys (AA 2024 and AA 2618) the activation energy is 117000 J/mole (1.21 eV/atom) [75, 112].
   b. For AA 2219-T31 and AA 2219-T42, the reaction rate for θ' formation was calculated using an Avrami expression with n = 1.1, resulting in an activation energy of 117000 J/mole (1.21 eV/atom) [84]. The reported pre-exponential coefficients are 1.15×10^{9} and 3.40×10^{9} s^{-1}.
   c. For AA 2124, the activation energy is reported to be 113900 J/mole (1.18 eV/atom) when using DSC data, and 128000 J/mole (1.33 eV/atom) when analyzing DIC data [73].
   d. For AlCu alloys, values of 0.75 and 1.10±0.10 eV/atom were reported [98]. Starink recalls also the following results from other researchers: 1.20±0.13, 1.25±0.09 and 1.02±0.02 eV/atom.
6. θ' dissolution: No references have been found that report kinetic parameters for this phase transformation. The reason is that, although it is dominated by kinetics, the dissolution of θ' is not good for kinetics analysis since its peak in DSC thermograms appears overlapped with those of other phase transformations, as occurs for AA 2219 [84].
7. θ formation: No references have been found that report kinetic parameters for this phase transformation. The reason might be the same as for θ' dissolution [84].
8. θ dissolution: No references have been found that report kinetic parameters for this phase transformation. The reason is probably that θ dissolution is controlled by thermodynamics, so the kinetic factors are not important in this case [9, 84].

9. S" formation: No references have been found that report kinetic parameters for this phase transformation. The reason is that precipitation of S" is not good for kinetics analysis [77].
10. S" dissolution: No references have been found that report kinetic parameters for this phase transformation.
11. S' formation:
    a. For AlCuMg alloys (AA 2024 and AA 2618) the activation energy is 129900 J/mole (1.35 eV/atom) [9, 75], close to that for diffusion of solute atoms and consistent with other reported values [84]. The pre-exponential coefficient is 2.55×10^{9} s^{-1}.
    b. For an AlCuMg alloy, the activation energy of S' formation is 134000 J/mole (1.39 eV/atom) [77].
12. S' dissolution: No references have been found that report kinetic parameters for this phase transformation. The reason is that S' dissolution is controlled by thermodynamics, so the kinetic factors are not important in this case [9].
13. S formation: No references have been found that report kinetic parameters for this phase transformation.
14. S dissolution: No references have been found that report kinetic parameters for this phase transformation.

1.9.4 Summary of phase transformation kinetics for AA 7075 & AA 2024

Tables 11 and 12 summarize the models reported in Section 1.9.1 that have been proposed for the reaction rates of the various phase transformations involved in the precipitation sequences of AA 7075 and AA 2024. The activation energies of the mentioned phase transformations are also included in these tables, as reviewed in Sections 1.9.2 and 1.9.3.

Table 11 Proposed models and activation energies for transformations in ageing sequence of AA 7075.

Transformation	Model	E_A [eV/atom]	Reference	Observations
GPZ formation	$F = F_f - (F_f - F_i)\exp(\frac{-t}{t_C})$	0.59–0.67	[16]	Commercial AlZnMgCu
		0.35–1.08	[86]	AlZnMgZr alloy
	$t_C = t_0 \exp(\frac{E_A}{KT})$ m-order Eyring rate Eq.			
GPZ dissolution		1.40	[82]	AA 7075-T6
	Eq. 3 & Eq. 2	0.78 & 1.27	[84]	AA 7075, 6 months at RT
		1.23	[96]	AA 7075-T6
η' formation	Avrami Eq., n = 2.3–2.8	0.57–0.62	[86]	AlZnMgZr alloy
η' dissolution	–	–	[84]	Not good for kinetics analysis
η formation	–	–	[84]	Not good for kinetics analysis
η dissolution	–	–	[9, 84, 96]	Thermodynamically controlled

Table 12 Proposed models and activation energies for transformations in ageing sequence of AA 2024.

Transformation	Model	E_A [eV/atom]	Reference	Observations
GPZ/GPBZ	Arrhenius-type Eq.	0.54–0.66	[9]	AlCuMg alloy
Formation	Avrami Eq.	0.76 & 0.79	[73]	AA 2124
		0.67 & 0.69	[77]	AlCuMg alloy
GPZ/GPBZ	Arrhenius-type Eq.	1.28	[9]	AlCuMg alloy
Dissolution	Eq. 3 & Eq. 2	0.82 & 1.31	[84]	AA 2219-T31 & AA 2219
		1.66	[73]	AA 2124
θ” formation	–	1.34	[75]	AA 2024 & AA 2618
		1.33 & 1.36	[73]	AA 2124
θ” dissolution	–	–	–	No references were found
θ’ formation		1.21	[75]	AA 2024 & AA 2618
	Avrami Eq., n = 1.1	1.21	[84]	AA 2219-T31 & AA 2219
		1.18 & 1.33	[73]	AA 2124
		0.75 & 1.10	[98]	AlCu alloy
		1.02 & 1.20	[125]	
		1.25	[126]	
θ’ dissolution	–	–	[84]	Not good for kinetics analysis
θ formation	–	–	[84]	Not good for kinetics analysis
θ dissolution	–	–	[9, 84, 98]	Thermodynamically controlled
S” formation	–	–	[77]	Not good for kinetics analysis
S” dissolution	–	–	–	No references were found
S’ formation	Arrhenius-type Eq.	1.35	[75]	AA 2024 & AA 2618
	Eq. 4 & Avrami Eq., n = 1.0		[9]	AlCuMg alloy
		1.39	[77]	Not good for kinetics analysis
S’ dissolution	–	–	[9]	Thermodynamically controlled
S formation	–	–	–	No references were found
S dissolution	–	–	–	No references were found

2 EXPERIMENTAL

In this chapter, the materials and methods used to conduct the experimental research are first reviewed. Second, the experimental results obtained for AA 7075-T6, AA 2024-T3 and pure Al are presented.

2.1 MATERIALS & METHODS

In this section, we briefly present the tested materials, the features of the samples and the following experimental techniques: DMA, DSC and TEM. The particularities of the experimental set up are described. Finally, the Time-Temperature Superposition (TTS) principle is commented.

2.1.1 Tested specimens

The tested specimens were rectangular plates of 60 mm in length, 8 to 15 mm in width and 2 mm in thickness. These plates were machine cut from sheet of as-received, commercial AA 7075-T6, AA 2024-T3 and sheet of 99.5% pure Al in the H24 temper. The mechanical properties and chemical composition of the alloys are shown in Tables 13, 14 and 15, respectively, as provided by the manufacturer.

Table 13 Mechanical properties of AA 7075-T6 and AA 2024-T3.

Aluminium alloy	Yield stress	UTS	Elongation	Brinell Hardness
AA 7075-T6	502 MPa	583 MPa	12%	161
AA 2024-T3	377 MPa	485 Mpa	15%	123

Table 14 Chemical composition in wt.% of AA 7075-T6 and AA 2024-T3.

Aluminium alloy	Si	Fe	Cu	Mn	Mg	Zn	Ti	Pb	Cr	Ni	Others
AA 7075-T6	0.06	0.15	1.50	0.01	2.58	6.00	0.05		0.19		
AA 2024-T3	0.18	0.28	4.46	0.64	1.35	0.04	0.05		0.01		0.01

Table 15 Chemical composition in at.% of AA 7075-T6 and AA 2024-T3.

Aluminium alloy	Si	Fe	Cu	Mn	Mg	Zn	Ti	Pb	Cr	Ni	Others
AA 7075-T6	0.06	0.08	0.67	0.01	2.99	2.59	0.03		0.10		
AA 2024-T3	0.18	0.14	1.95	0.32	1.54	0.02	0.03		0.01		0.00

2.1.2 Dynamic-Mechanical Analyser (DMA)

A TA Instruments Q800 DMA was used to measure the viscoelastic response of the studied materials. The DMA is able to apply a mechanical excitation of selected frequency and amplitude under controlled

temperature conditions, while recording displacements and stiffness. This allows the evaluation and characterization of intrinsic and extrinsic mechanical properties of the material, namely the creep response or the relaxation or viscoelastic behaviour (e.g. the storage modulus *E'*, the loss modulus *E"* and the loss tangent) as a function of frequency and temperature [45]. Moreover, this thermal analysis technique is sensitive to phase transformations, so it may be used to gather information on formation and dissolution of precipitate phases [54].

For the conventional tests, aimed at measuring the viscoelastic response of the studied materials, the DMA was configured to sequentially apply dynamic loading with frequencies of 100, 30, 10, 3 and 1 Hz, under isothermal conditions, at different temperatures, from 35 to 375 ºC in step increments of 5 ºC[10]. A 3-Point Bending (3PB) clamp was used for applying the loads. During the tests, data were isothermally recorded and, aside from other interesting parameters, the storage and loss moduli were computed for each of the frequencies at each temperature step. Unfortunately, the manufacturer of the DMA does not provide information on the instrument error, but the model equations used for the computations are provided instead. For example, the DMA computes the storage modulus using the measured stiffness and the input dimensions of the samples, so the error in this case depends on the experimental error in measuring the stiffness and sample dimensions. We conducted an error propagation analysis (see Annex A). The main conclusions are that an error of 1% in stiffness or in sample width propagates into an error of 1% in storage modulus, while an error of 1% in sample length or thickness propagates respectively into an error of 3% in storage modulus. Thus, special care must be taken in measuring the thickness only, since for the 3PB clamp type the length is fixed and is equal to the distance between the two supports.

Finally, a series of control tests were also performed with the DMA[11] on AA 7075-T6. Each of these tests consisted in a sequence of three cycles of heating from 35 to 100ºC in step increments of 5 ºC, followed by cooling in air at RT. The test frequencies were 100, 10 and 1 Hz and the clamp type was also 3PB. The objective of these tests was to ascertain whether GPZ precipitation was completed or not in the studied samples prior to the realization of the conventional DMA tests. For this purpose, the storage and loss moduli are measured and, if they behave reversibly, this means that no irreversible process (e.g. a microstructural transformation) occurs in the test temperature region. Thus, for instance, if the viscoelastic response is reversible from 35 to 100 ºC we may assure that GPZ precipitation is complete.

2.1.3 Differential Scanning Calorimeter (DSC)

DSC measures the energy necessary to establish a nearly zero temperature difference between a material and an inert reference, as the two specimens are subjected to identical temperature regimes in an environment heated or cooled at a controlled rate. DSC allows characterizing the enthalpies of phase transformations, and their kinetics via the Kissinger method [73, 84]. The enthalpies are associated to the

[10] The temperature increase with time is stepwise. When in the text we refer to the heating rate in our DMA tests, we mean the slope of the linear regression of the time-evolution of the test temperature, i.e. approximately 1 ºC/min.
[11] These control DMA tests will be termed "reversibility tests" from now on.

areas of the specific exothermic or endothermic regions of the thermograms curve in the corresponding temperature range [82]. Essentially, there are two types of DSC systems [127]:

- Power compensation DSC: In this case, the temperatures of the sample and the reference are controlled independently using separate, identical furnaces. The temperatures are made identical by varying the power input to the furnaces. The energy required is a measure of the enthalpy or heat capacity changes in the sample relative to the reference.
- Heat-flux DSC: In this case, the sample and reference are enclosed in a single furnace and connected by a low resistance heat flow path. Enthalpy or heat capacity changes in the sample cause a difference in its temperature relative to the reference. The temperature difference is recorded and related to enthalpy changes in the sample using calibration experiments.

In this work, the calorimetric measurements on AA 7075-T6 have been performed using a NETZSCH DSC 404, under dynamic pure argon atmosphere. DSC scans ran from 50 to 475 ºC at a heating rate of 5 ºC/min. For all samples, a second scan was always made in order to subtract the DSC baseline.

2.1.4 Transmission Electron Microscope (TEM)

TEM allows elucidation of the microstructure and phase identification. It operates on the same basic principles as the light microscope but uses a beam of electrons instead of light. Thus, the TEM is capable of resolving objects at a significantly higher resolution than light microscopes, thanks to the much lower De Broglie wavelength of electrons respect to light. The electron beam is transmitted through a very thin specimen (previously polished). After the interaction of the electron beam with the sample, the image is formed onto, for instance, a fluorescent screen or a layer of photographic film, or is detected by a sensor, like a charge-coupled device (CCD) camera. At lower magnifications, the contrast observed in TEM images is due to differences in the absorption of electrons in the specimen, which arise due to differences in the thickness and composition of the material. At higher magnifications, wave interactions modulate the intensity of the image and analysis of observed images is required [128].

2.1.5 The Time-Temperature Superposition (TTS) Principle

When the rate-limiting step of a relaxation process is that of movement over an energy barrier, the temperature dependence of the reciprocal of the relaxation time (i.e. the relaxation rate) follows an Arrhenius equation [45]. As a consequence, the dynamic response functions may be treated as if they were functions of temperature (while frequency is constant) instead of functions of frequency (while temperature, and thus the mechanical relaxation time, are constant) [1]. For example, the effect of increasing temperature on the viscoelastic response of materials is similar to the effect of reducing frequency. This is the basis for the TTS principle, which establishes the relationship between temperature

and time on the relaxation and deformation responses of viscoelastic materials subjected to constant stress/strain or to dynamic loading [7, 129, 130].

Based on the TTS principle, master curves can be obtained by superimposing the modulus spectra (storage and loss moduli) at different temperatures. This can be achieved by shifting horizontally (i.e. along the frequency axis) the isothermal curves of the moduli using a shift factor a_T. This factor defines the ratio of relaxation time or frequency at a given temperature to that at an arbitrary chosen reference temperature. The relation between the shift factor and temperature is typically described by the Williams-Landel-Ferry (WLF) equation (e.g. for amorphous polymers) or by the Arrhenius expression [129].

A master curve may be used to transform material properties from the frequency domain to the temperature domain, and vice versa [2, 131]. In principle, it allows also extrapolating the viscoelastic behaviour to any temperature or frequency. But in reality, the master curve for a given shift factor is only valid generally within a limited temperature range, because the shift factor, aside from temperature, may depend also on aging (i.e. the microstructure) and the relaxation mechanisms of the viscoelastic spectrum. For example, the shift factor will exhibit different temperature dependencies from a temperature interval to another, and thus there will be different master curves, if phase transformations occur in between or different relaxation mechanisms intervene. This can be used to detect the occurrence of phase transformations from DMA data [129].

2.2 EXPERIMENTAL RESULTS FOR AA 7075-T6

In this section, it is first reported the experimental storage modulus, loss modulus and loss tangent for AA 7075-T6. Second, we present DSC thermograms and the results of the reversibility tests obtained with the DMA for AA 7075-T6.

2.2.1 Storage modulus

Fig. 9 shows the storage modulus for AA 7075-T6 as a function of temperature, from 35 to 375 ºC, for mechanical excitations of frequencies 100, 30, 10, 3 and 1 Hz. As a general trend, the storage modulus decreases initially with temperature for all the studied frequencies. The slope becomes more pronounced at about 150–190 ºC, and an inflexion appears around 220–250 ºC. There is a local maximum around 300–330 ºC, after which the storage modulus decreases again. It can be observed that the storage modulus depends more significantly on frequency at high temperatures, i.e. above 100 ºC, being almost insensitive to frequency below this temperature threshold. In addition, at high temperatures, the decrease in the storage modulus at low frequencies is larger than that at higher frequencies. For higher frequencies, the inflexion seems to appear at lower temperatures while the maximum is shifted towards higher temperatures. Finally, the isothermal curves of storage modulus vs. frequency for various temperatures are presented in Fig. 10. Plotting moduli data against frequency is interesting particularly as

a first step for application of the TTS principle, and also for the study of the relaxation spectra, in the case of the loss modulus.

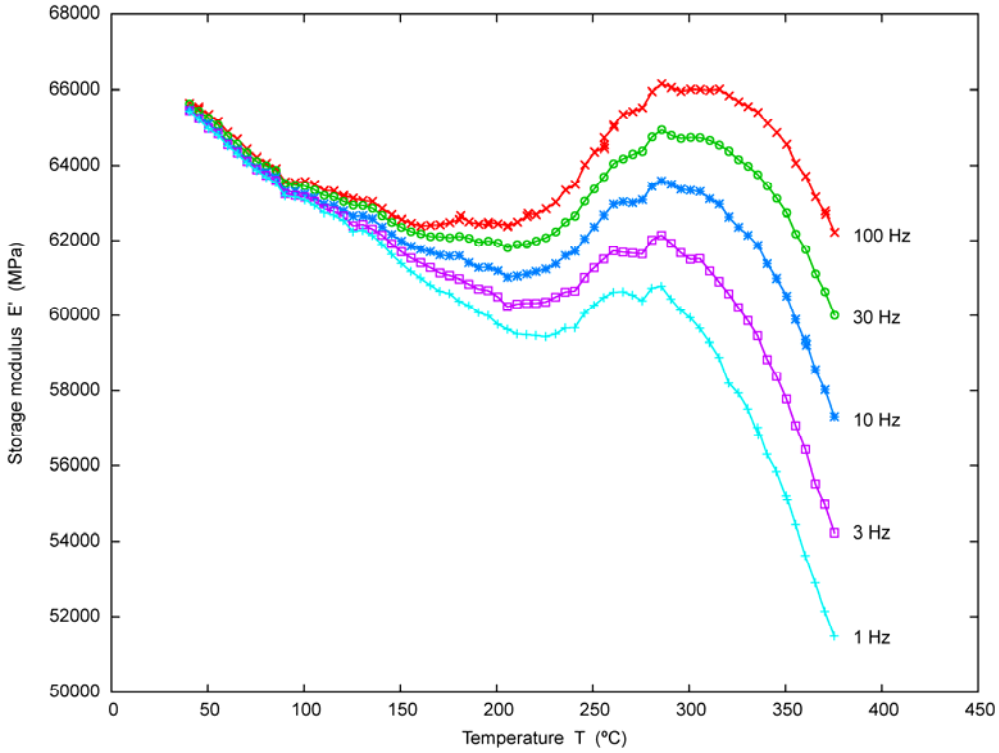

Fig. 9 Storage modulus *E'* vs. temperature *T* from DMA tests on AA 7075-T6 at 100, 30, 10, 3 and 1 Hz, from 35 to 375 ºC.

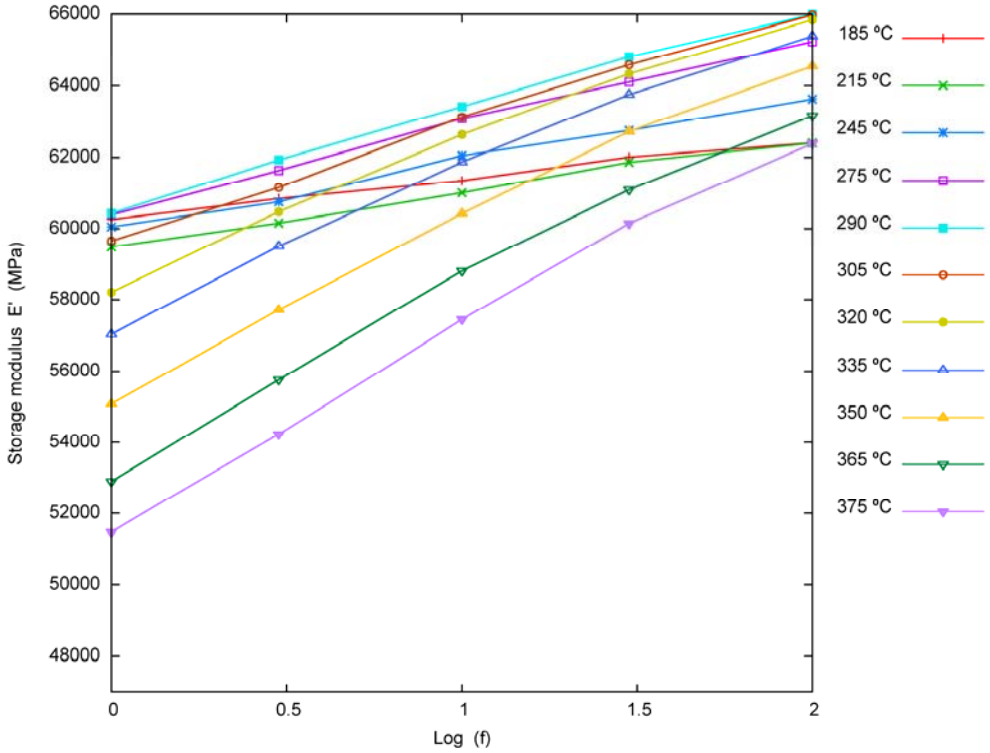

Fig. 10 Storage modulus *E'* vs. logarithm of the frequency *f* from DMA tests on AA 7075-T6 at temperatures ranging from 185 to 375ºC and frequencies ranging from 1 to 100 Hz.

2.2.2 Loss modulus

Fig. 11 shows the loss modulus for AA 7075-T6 as a function of temperature, from 35 to 375 ºC, for mechanical excitations of frequencies 100, 30, 10, 3 and 1 Hz. As a general trend, the loss modulus exhibits no significant changes at low temperatures, where it is virtually constant. It starts to increase at about 120–140 ºC, with decreasing slopes as the mechanical excitation frequency is increased. The higher the frequency, the higher the temperature at which the modulus starts to increase. Finally, it is worth to mention that, on the one hand, for all the tests the loss modulus increases monotonically, i.e. no peak is observed in the studied temperature range. On the other hand, at low temperatures (e.g. below 160 ºC approximately) the loss modulus is smaller for lower frequencies of mechanical excitation, while at higher temperatures it is smaller for higher frequencies. Finally, the isothermal curves of loss modulus vs. frequency for various temperatures are presented in Fig. 12. A peak can be observed in two curves.

2.2.3 Loss tangent

Fig. 13 shows the loss tangent for AA 7075-T6 as a function of temperature, from 35 to 375 ºC, for mechanical excitations of frequencies 100, 30, 10, 3 and 1 Hz. As a general trend, the loss tangent exhibits qualitatively the same behaviour as the loss modulus for AA 7075-T6 (see Section 2.2.2) as the relative change in the loss modulus is much higher than the relative change in the storage modulus in the tested range of temperatures.

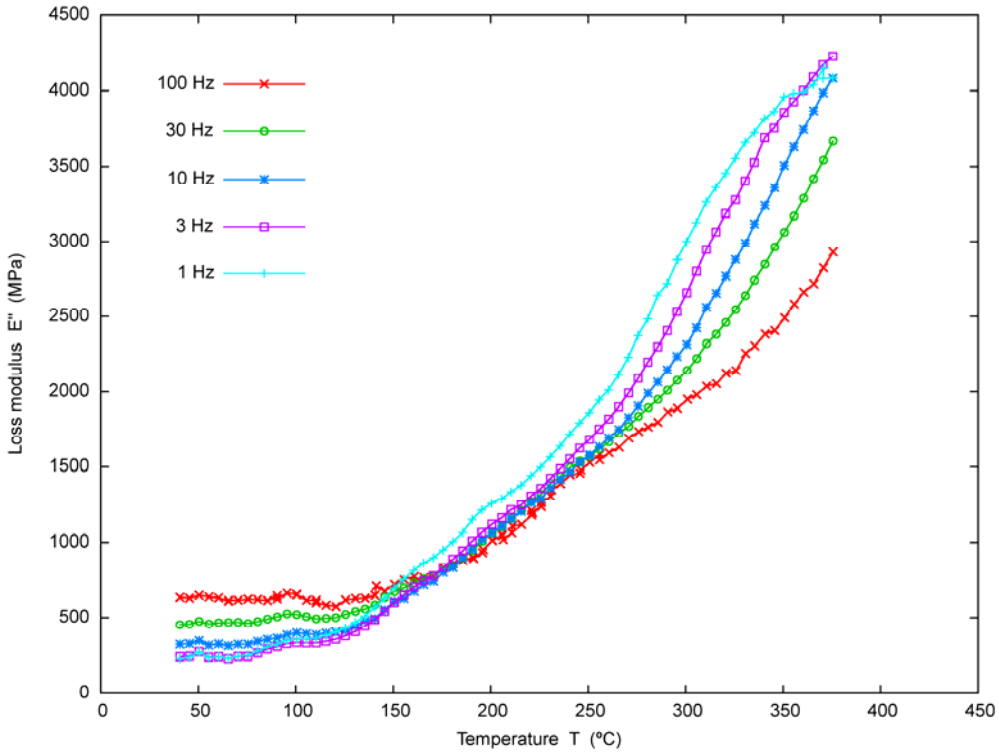

Fig. 11 Loss modulus *E''* vs. temperature *T* from DMA tests on AA 7075-T6 at 100, 30, 10, 3 and 1 Hz, from 35 to 375 ºC.

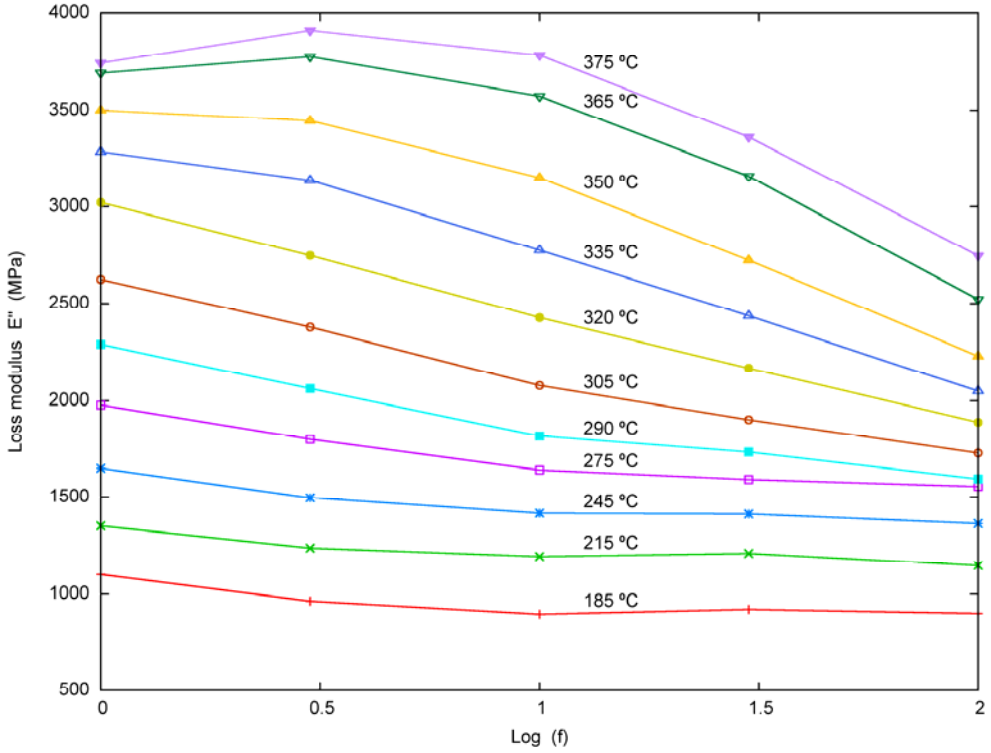

Fig. 12 Loss modulus *E"* vs. logarithm of the frequency *f* from DMA tests on AA 7075-T6 at temperatures ranging from 185 to 375ºC and frequencies ranging from 1 to 100 Hz.

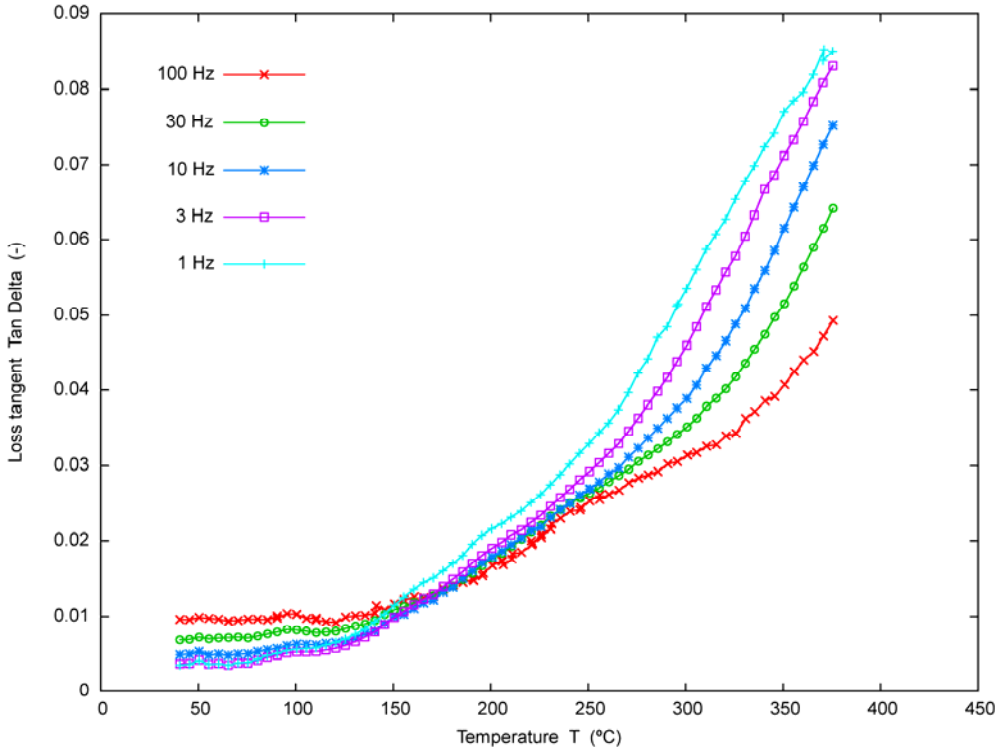

Fig. 13 Loss tangent *Tan δ* vs. temperature *T* from DMA tests on AA 7075-T6 at 100, 30, 10, 3 and 1 Hz, from 35 to 375 ºC.

2.2.4 DSC thermograms

The results obtained after DSC scans on two samples of as-received AA 7075-T6 are shown in Fig. 14. The scans ran from 50 to 475 ºC at a heating rate of 5 ºC/min. It can be observed that the peaks are relatively low, which means that the phase transformations have relatively low enthalpies. There is an endothermic peak at 114 ºC, an exothermic peak centred at 200 ºC and another endothermic peak around 245–250 ºC. These peaks may correspond to GPZ dissolution, η' phase formation and η' phase dissolution, respectively. Finally, both scans show also a reversible process at around 400 °C.

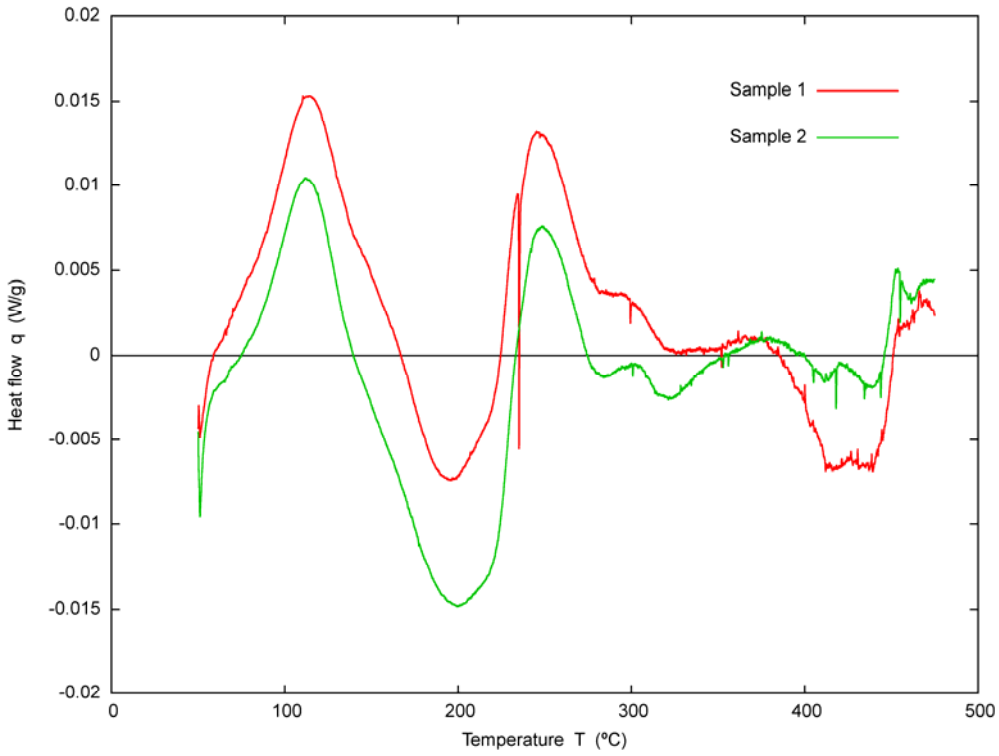

Fig. 14 Specific heat flow *q* vs. temperature *T* from DSC scans on AA 7075-T6 from 50 to 475 ºC at a heating rate of 5 ºC/min.

2.2.5 Reversibility tests

AA 7075-T6 samples were subjected to the so-called reversibility tests with the DMA. Fig. 15 shows the storage modulus obtained after one of these 3-cycles DMA tests at 1 Hz. To eliminate the discrepancies in the storage moduli due to the instrument error, the ratio of storage modulus-to-storage modulus at 45 ºC was calculated for each cycle, and it is presented in Fig. 16 for comparison purposes.

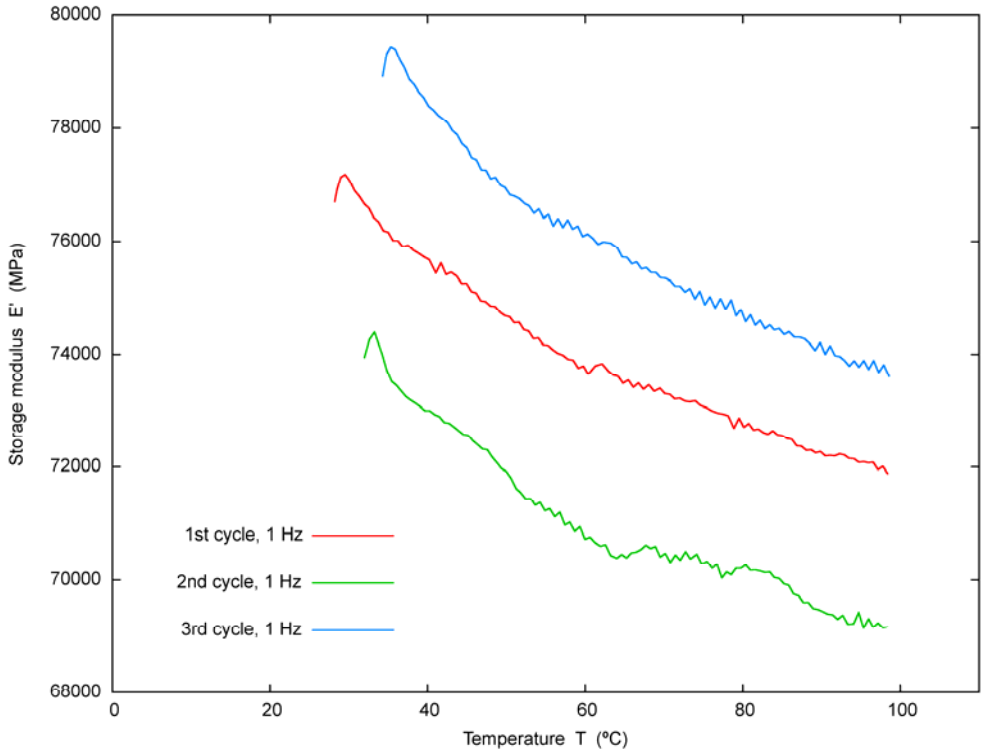

Fig. 15 Storage modulus *E'* vs. temperature *T* from reversibility test on AA 7075-T6 at 1 Hz, from 35 to 100 ºC.

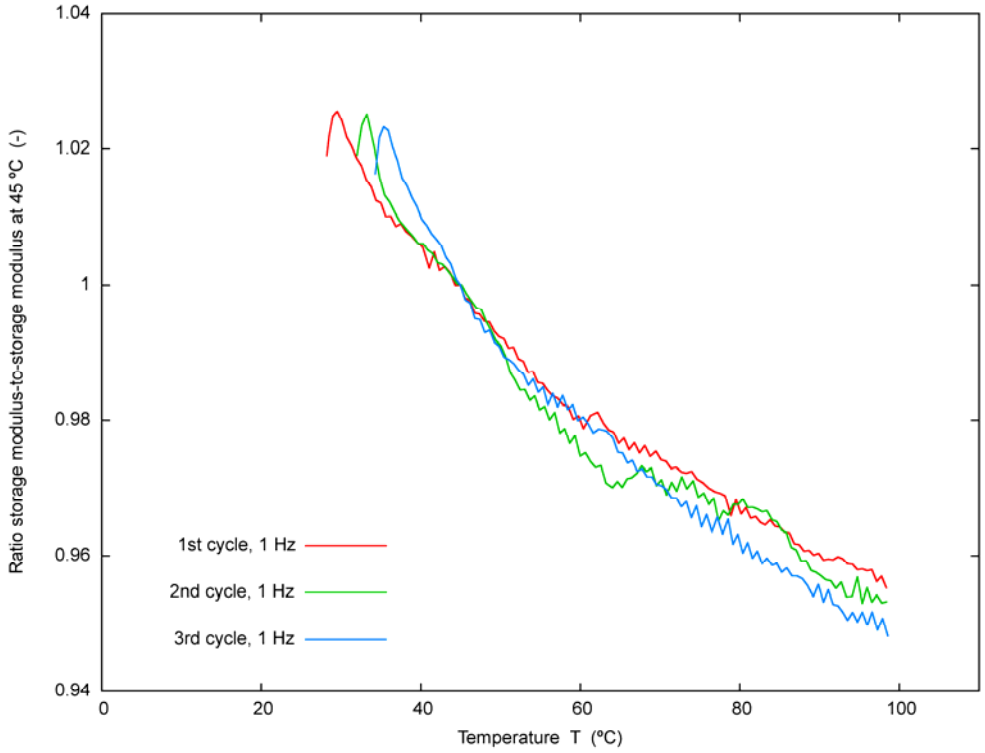

Fig. 16 Ratio of storage modulus-to-storage modulus at 45 ºC vs. temperature *T* from reversibility test on AA 7075-T6 at 1 Hz, from 35 to 100 ºC.

2.3 EXPERIMENTAL RESULTS FOR AA 2024-T3

In this section, it is first reported the experimental storage modulus, loss modulus and loss tangent for AA 2024-T3. Second, we present a DSC thermogram from the literature and the results.

2.3.1 Storage modulus

Fig. 17 shows the storage modulus for AA 2024-T3 as a function of temperature, from 35 to 375 ºC, for mechanical excitations of frequencies 100, 30, 10, 3 and 1 Hz. Qualitatively, the behaviour is similar to that for AA 7075-T6 (see Section 2.2.1). As a general trend, the storage modulus also decreases initially. Similarly to AA 7075-T6, the slope becomes more pronounced at about 150–190 ºC, and the inflexion appears around 200–240 ºC. The local maximum is observed around 280–300 ºC, and it is slightly delayed in temperature as the frequency increases, as occurs for AA 7075-T6. Again, the storage modulus depends more significantly on frequency at high temperatures, being almost insensitive to frequency at low temperatures. Also, at high temperatures, the decrease in the storage modulus at low frequencies is larger than that at higher frequencies. Finally, the isothermal curves of storage modulus vs. frequency for various temperatures are presented in Fig. 18.

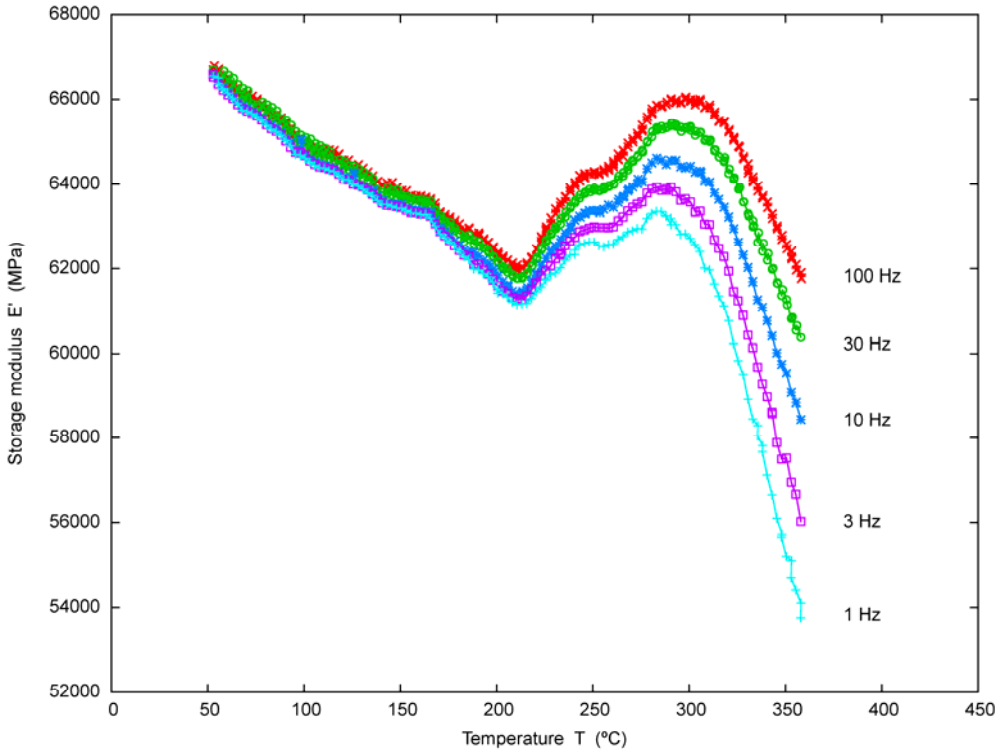

Fig. 17 Storage modulus *E'* vs. temperature *T* from DMA tests on AA 2024-T3 at 100, 30, 10, 3 and 1 Hz, from 35 to 375 ºC.

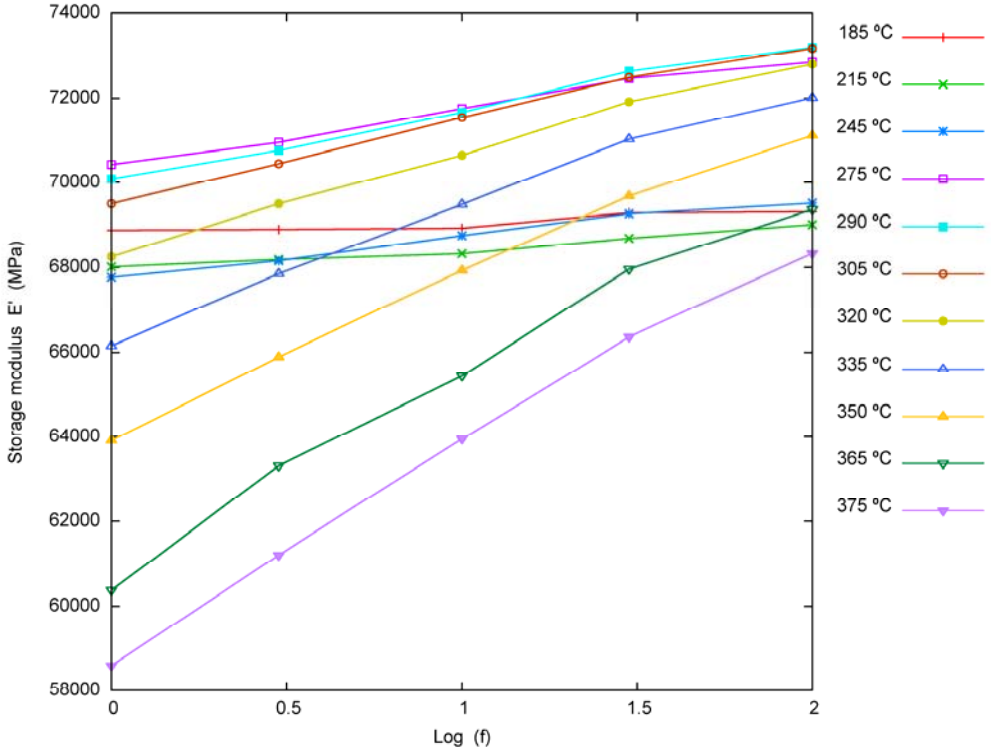

Fig. 18 Storage modulus *E'* vs. logarithm of the frequency *f* from DMA tests on AA 2024-T3 at temperatures ranging from 185 to 375ºC and frequencies ranging from 1 to 100 Hz.

2.3.2 Loss modulus

Fig. 19 shows the loss modulus for AA 2024-T3 as a function of temperature, from 35 to 375 ºC, for mechanical excitations of frequencies 100, 30, 10, 3 and 1 Hz. The behaviour of the loss modulus is also qualitatively similar to that for AA 7075-T6 (see Section 2.2.2). Particularly, after exhibiting no significant changes at low temperatures for all frequencies, it starts to rise at about 200–220 ºC with decreasing slopes as the mechanical excitation frequency is increased. Again, the higher the frequency, the higher the temperature at which the modulus starts to increase. For most of the tests, the loss modulus increases with temperature monotonically. At low temperatures (e.g. below 275 ºC approximately) the loss modulus is also smaller for lower frequencies of mechanical excitation, while at higher temperatures it is smaller for higher frequencies. Finally, the isothermal curves of loss modulus vs. frequency for various temperatures are presented in Fig. 20. No peak is observed in this case.

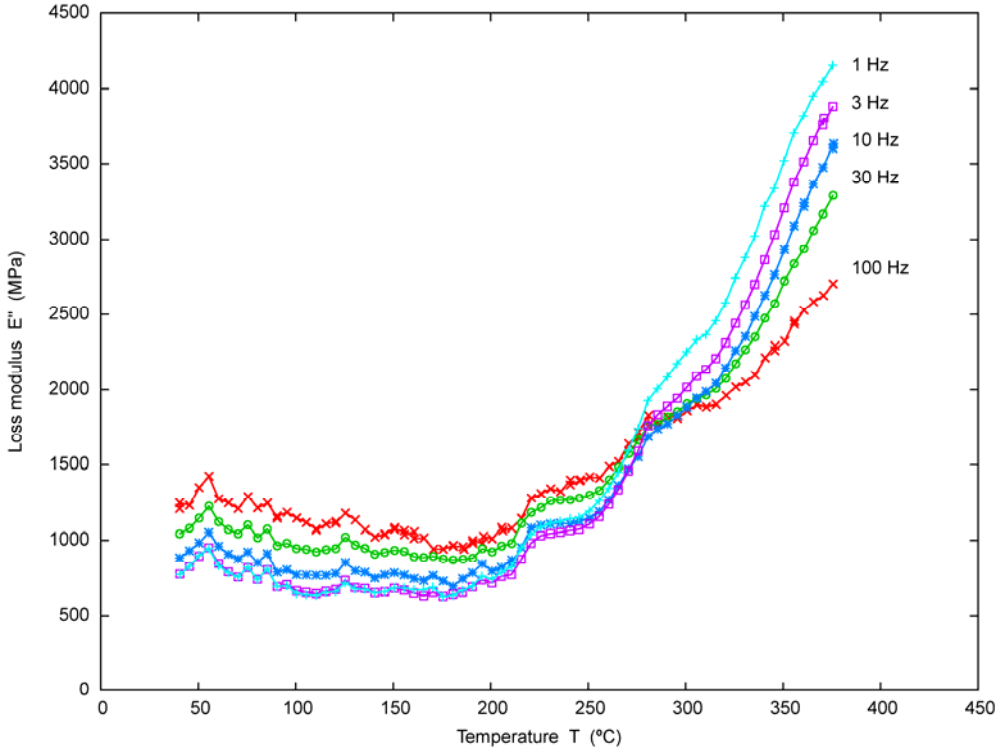

Fig. 19 Loss modulus *E"* vs. temperature *T* from DMA tests on AA 2024-T3 at 100, 30, 10, 3 and 1 Hz, from 35 to 375 ºC.

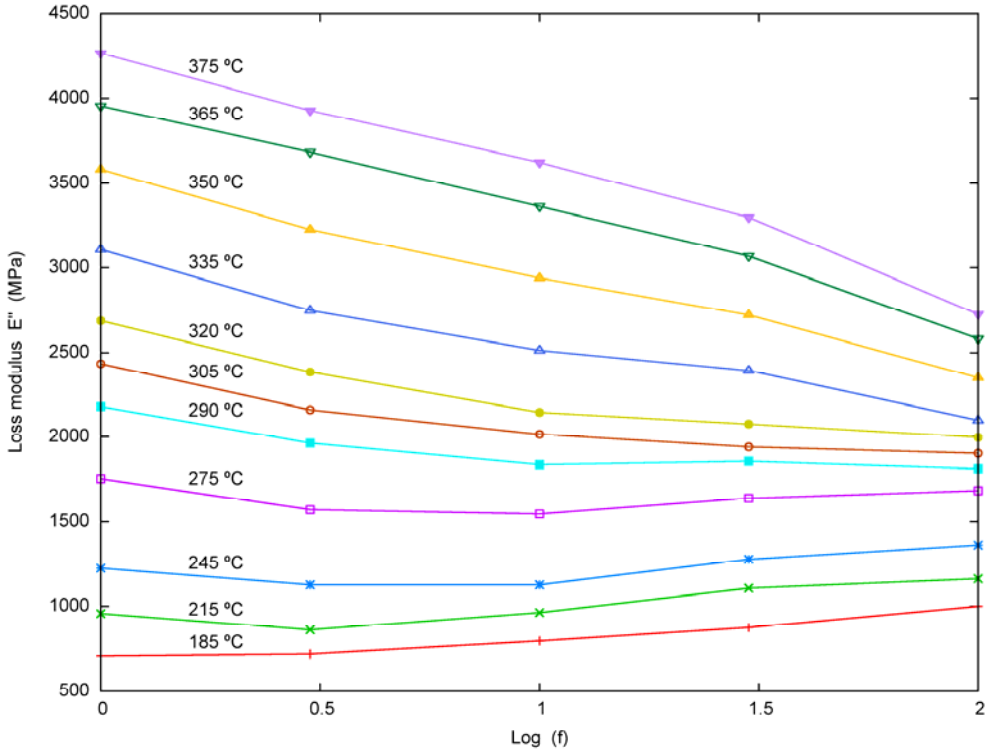

Fig. 20 Loss modulus *E"* vs. logarithm of the frequency *f* from DMA tests on AA 2024-T3 at temperatures ranging from 185 to 375ºC and frequencies ranging from 1 to 100 Hz.

2.3.3 Loss tangent

Fig. 21 shows the loss tangent for AA 2024-T3 as a function of temperature, from 35 to 375 ºC, for mechanical excitations of frequencies 100, 30, 10, 3 and 1 Hz. As for AA 7075-T6, the loss tangent exhibits qualitatively the same behaviour as the loss modulus for AA 2024-T3 (see Section 2.3.2).

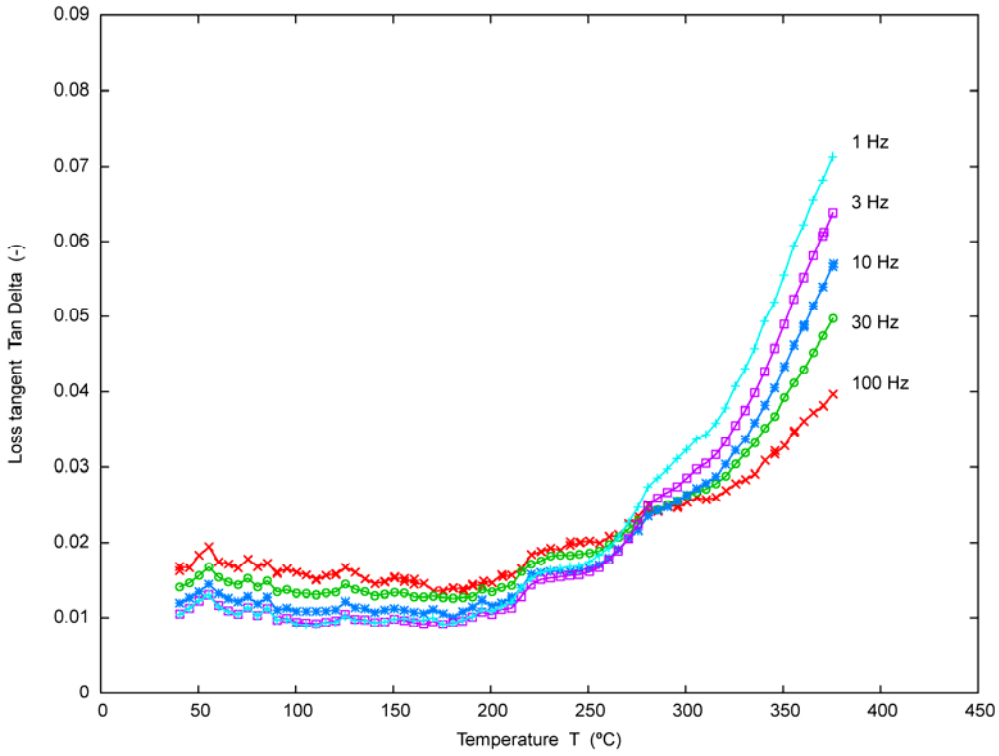

Fig. 21 Loss tangent *Tan δ* vs. temperature *T* from DMA tests on AA 2024-T3 at 100, 30, 10, 3 and 1 Hz, from 35 to 375 ºC.

2.3.4 DSC thermograms

Fig. 22 shows an experimental DSC scan on an AlCuMg alloy, together with a simulated scan obtained using a model proposed by the author of that work [115]. The scans ran from 100 to almost 500 ºC at a heating rate of 20 ºC/min. There is a small endothermic reaction at 150–250 °C, a large exothermic peak at 250–320 °C and a wide endothermic reaction running trough at 320–470 °C. According to the author, these peaks may correspond to GPZ dissolution and S phase precipitation and dissolution, respectively.

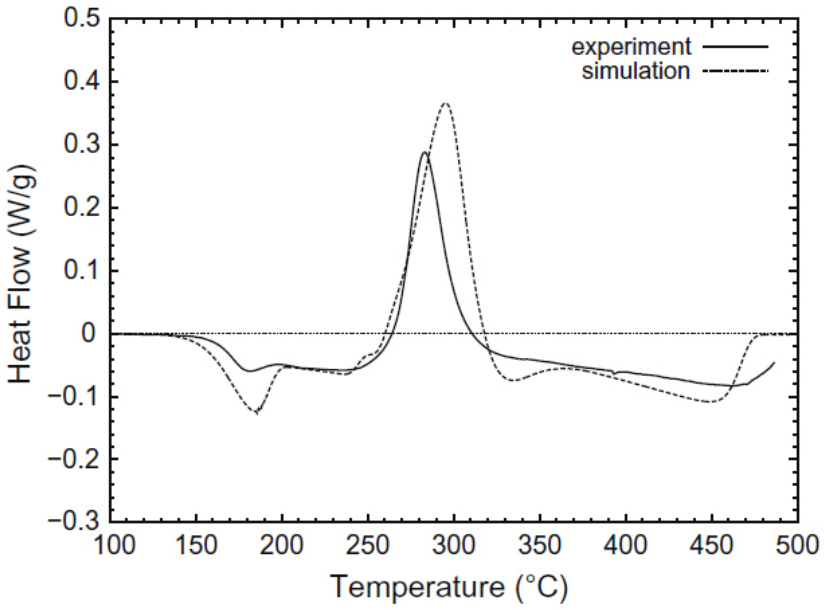

Fig. 22 Specific heat flow q vs. temperature T from experimental and simulated DSC scans on AA 2024-T3 from 100 to 500 ºC at a heating rate of 20 ºC/min [115] (printed with permission from Elsevier).

2.4 EXPERIMENTAL RESULTS FOR PURE ALUMINIUM

In this section, it is reported the experimental storage modulus, loss modulus and loss tangent for the pure Al samples. Capitalizing the absence of phase transformations for pure Al, the DMA data on pure Al will be used as baseline reference for comparison purposes with data available in the literature and when discussing on the phenomena observed in the response of AA 7075-T6 and AA 2024-T3.

2.4.1 Storage modulus

Fig. 23 shows the storage modulus for pure Al as a function of temperature, from 35 to 375 ºC, for excitation frequencies of 100, 30, 10, 3 and 1 Hz. The behaviour of the storage modulus is similar in some aspects to that for AA 7075-T6 and AA 2024-T3 (see Sections 2.2.1 and 2.3.1). For example, the storage modulus also decreases initially. The slope at low temperature (below the beginning of GPZ/GPBZ dissolution for the alloys) is what is most interesting to us, as will be explained later on. Also, at high temperatures (above 150 ºC) the storage modulus depends more significantly on frequency, and the decrease in the storage modulus at low frequencies is larger than that at higher frequencies. Finally, a dramatic decrease in storage modulus is observed, which begins at 230–280 ºC. This abrupt drop in storage modulus is shifted to higher temperatures as frequency increases.

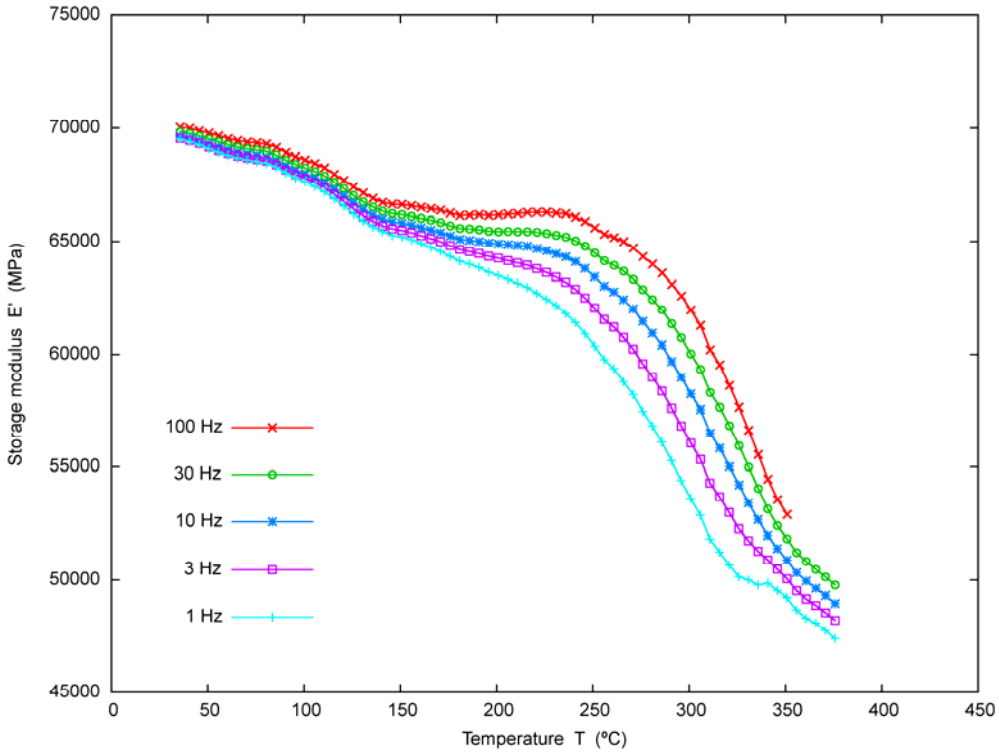

Fig. 23 Storage modulus *E'* vs. temperature *T* from DMA tests on pure Al (in the H24 temper) at 100, 30, 10, 3 and 1 Hz, from 35 to 375 ºC.

Table 16 shows the values of the storage modulus temperature gradient for pure Al at low temperatures, obtained by linear regression of the storage modulus vs. temperature data between 35 and 100 ºC, for each frequency. These values will be compared to the slopes calculated by simulations using the proposed storage modulus model on pure Al, to assess the error of the simulations (see Section 3.6).

Table 16 Rate of storage modulus loss with temperature for pure Al by linear regression of DMA data.

Frequency [Hz]	Storage modulus temperature gradient [MPa·°C^{-1}]
100	-23.1±0.5
30	-25.2±0.4
10	-26.4±0.5
3	-27.9±0.5
1	-29.7±0.8

2.4.2 Loss modulus

Fig. 24 shows the loss modulus for pure Al as a function of temperature, from 35 to 375 ºC, for excitation frequencies of 100, 30, 10, 3 and 1 Hz. The behaviour of the loss modulus is noticeably different to that for AA 7075-T6 and AA 2024-T3 (see Sections 2.2.2 and 2.3.2). At low temperatures the slopes of the loss modulus are similar for all the studied frequencies and not very steep. At 170–260 ºC the slopes increase sharply. This slope variation is shifted towards higher temperatures with increasing excitation

frequency. Contrary to what was observed for the alloys, the loss modulus for pure Al exhibits a peak, which is achieved practically at the same temperature for all the frequencies, around 300–310 ºC. The peak is larger (both in width and height) for lower frequencies. There is also a transition interval around 200–240 ºC between the low temperature region where the loss modulus is smaller for lower loading frequencies and the high temperature region where it is smaller for higher frequencies. Finally, there is a sharp decrease centred at 340 ºC, where the loss modulus behaviour with frequency is inverted again.

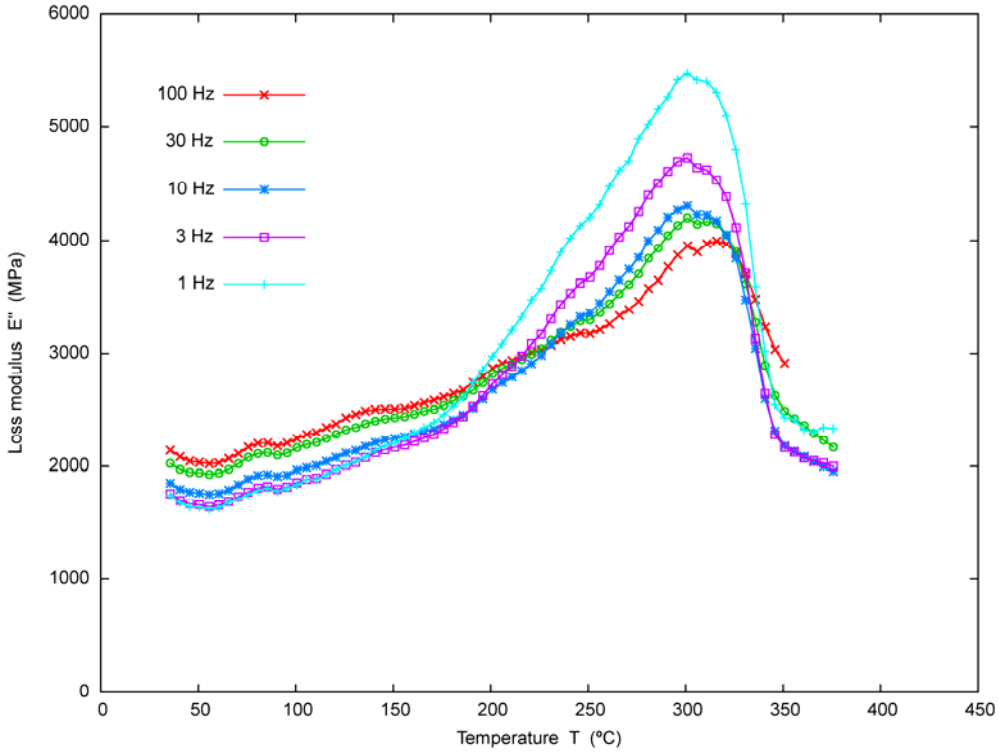

Fig. 24 Loss modulus *E"* vs. temperature *T* from DMA tests on pure Al (in the H24 temper) at 100, 30, 10, 3 and 1 Hz, from 35 to 375 ºC.

2.4.3 Loss tangent

Fig. 25 shows the loss tangent for pure Al as a function of temperature, from 35 to 375 ºC, for excitation frequencies of 100, 30, 10, 3 and 1 Hz. As a general trend, the loss tangent exhibits qualitatively the same behaviour as the loss modulus for pure Al (see Section 2.4.2).

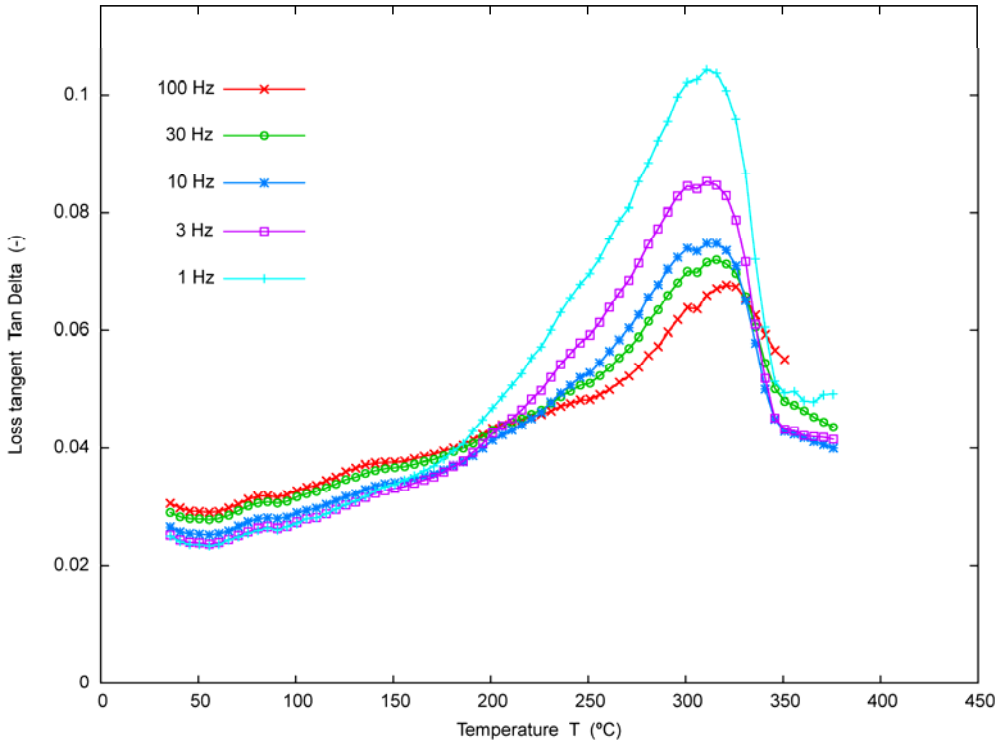

Fig. 25 Loss tangent *Tan δ* vs. temperature *T* from DMA tests on pure Al (in the H24 temper) at 100, 30, 10, 3 and 1 Hz, from 35 to 375 ºC.

2.5 APPLICATION OF TTS PRINCIPLE TO DMA RESULTS

The TTS principle has proven useful in obtaining master curves for amorphous materials [7], so we attempted applying a similar approach to the experimental data obtained for the studied alloys. In particular, the isothermal curves of storage and loss moduli vs. frequency (see Fig. 10, 12, 18 and 20) were superimposed by shifting along the frequency axis using an Arrhenius-type shift factor a_T [129]:

$$\ln a_T(T) = \frac{E_A}{K}\left(\frac{1}{T} - \frac{1}{T_0}\right) \qquad \text{Eq. 6}$$

where the arbitrary chosen reference temperature T_0 was 215 ºC, and E_A is an apparent activation energy associated to the mechanical relaxations. This way, for the storage modulus, it was possible to identify a master curve for a low temperature region (approximately from RT to 100–150 ºC) and, for the storage and loss moduli, another curve for a high temperature region (around 350 ºC). It was not possible to obtain any master curve for data between 150 and 300 ºC, though. The activation energies to obtain the master curves were determined by empirical fit (see Tables 17 and 18). For AA 7075-T6, the master curve for the storage modulus in the low temperature region is shown in Fig. 26, while the master curves for the storage and loss moduli in the high temperature region are shown in Fig. 27.

Table 17 Activation energy in the Arrhenius-type expression for the shift factor for AA 7075-T6 data.

	Activation energy in the Arrhenius expression for the shift factor	
Temperature region	Storage modulus data	Loss modulus data
Low temperature	0.30 eV/atom	No master curve was obtained[a]
High temperature	0.60 eV/atom	0.60 eV/atom

[a] Only values of activation energy below 0.01 eV/atom (with little physical significance) resulted in an acceptable degree of superposition of the loss modulus curves. Therefore, this result was disregarded.

Table 18 Activation energy in the Arrhenius-type expression for the shift factor for AA 2024-T3 data.

	Activation energy in the Arrhenius expression for the shift factor	
Temperature region	Storage modulus data	Loss modulus data
Low temperature	0.30 eV/atom	No master curve was obtained[a]
High temperature	0.80 eV/atom	0.80 eV/atom

[a] Only values of activation energy below 0.01 eV/atom (with little physical significance) resulted in an acceptable degree of superposition of the loss modulus curves. Therefore, this result was disregarded.

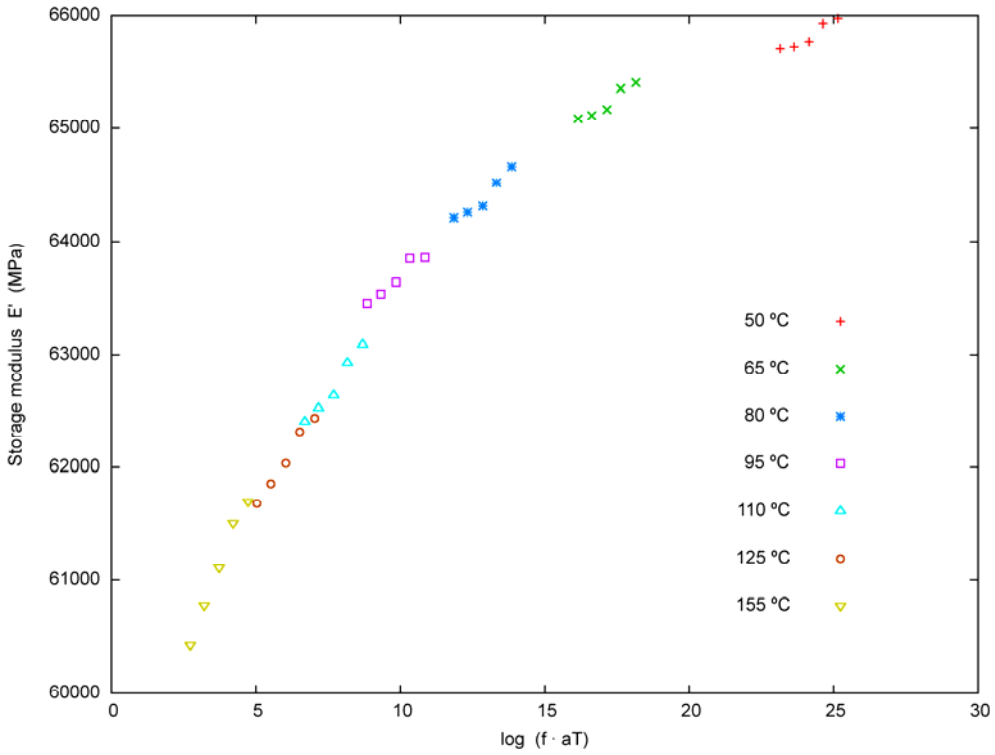

Fig. 26 Master curve showing the storage modulus E' vs. the logarithm of frequency f times the shift factor a_T. The curve resulted from horizontal shifting of curves from DMA tests on AA 7075-T6 at temperatures ranging from 50 to 155 ºC.

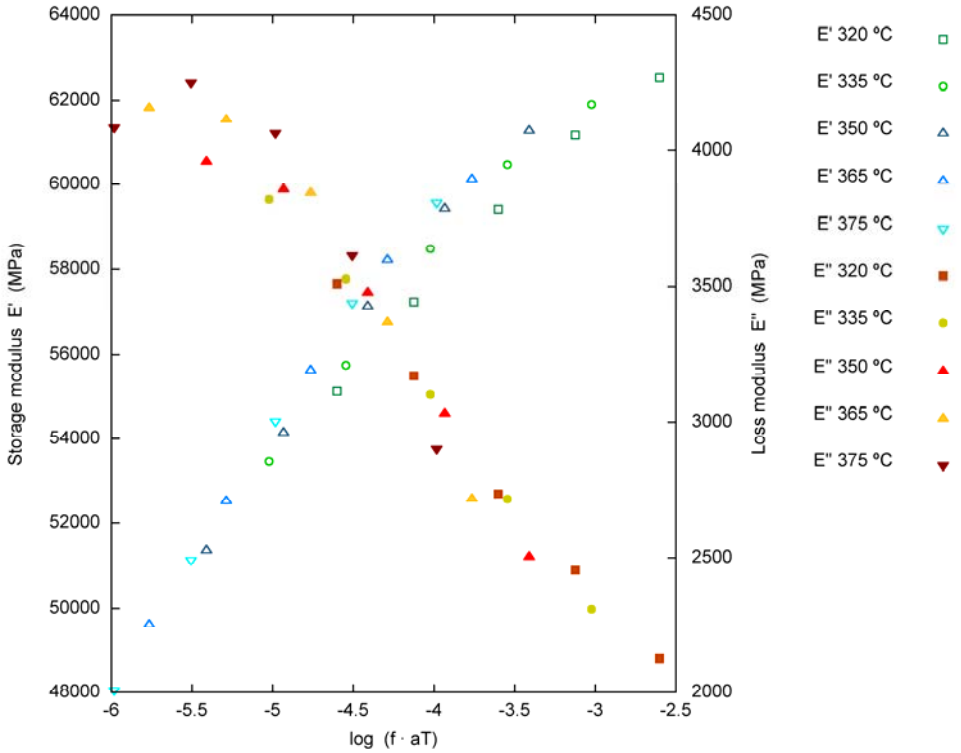

Fig. 27 Master curves showing the storage modulus *E'* and loss modulus *E''* vs. the logarithm of frequency *f* times the shift factor a_T. The curves resulted from horizontal shifting of curves from DMA tests on AA 7075-T6 at temperatures above 320 ºC.

3 MODEL

In this chapter, a model for the storage modulus is first described. Second, the rate equations used to model the evolution of various phase transformations are reviewed. Next, the solving process is explained. Finally, the model results obtained for AA 7075-T6, AA 2024-T3 and pure Al are presented.

3.1 MODELLING OF THE STORAGE MODULUS

In agreement with the DMA test results and research in the literature for aluminium alloys and other materials [1, 2, 54], it is assumed that the viscoelastic response of the studied alloys depends mainly on temperature and the frequency of the mechanical excitation, but also on the microstructure and thus the phase transformations.

According to the literature [52, 53, 132, 133], the static elastic modulus of pure Al and AA 2024 decreases linearly with temperature. Deviations from this linear behaviour were reported close to 0 K, well below the region of applicability of the model to be developed. Also, Wolfenden [55] observed a highly quasi-linear decrease of the dynamic elastic modulus with temperature, measured at a high frequency (80 kHz) from RT to 475 ºC, for pure Al and for AA 6061 reinforced with alumina.

Fig. 28 shows a comparison of static and high frequency dynamic elastic modulus data available in the literature with dynamic elastic modulus data obtained with the DMA for AA 2024-T3 and pure Al at 1 Hz. As expected, our DMA results for pure Al fall between the static and the high frequency dynamic values of the elastic modulus in the literature, but they depart from linearity showing a pronounced decrease of the dynamic elastic modulus between 250 and 300 °C. This is also coincident with the loss modulus peak shown in Fig. 24 at all frequencies. Wolfenden assumed a linear behaviour from RT to 475 ºC and explained this in terms of the Granato-Lücke theory for dislocation damping [134], but his data are too scattered to be explained with a single mechanism in all the considered temperature range, as it is shown by the DMA measurements reported in this work.

On the contrary, we consider that the low frequency elastic modulus is sensitive also to micrometric mechanisms such as boundary migration during recrystallization and grain growth, as shown by Zhang [135]. This mechanism is likely to be much more relevant in fatigue processes. However, as previously indicated, the microstructural evolution of AA 7075-T6 and AA 2024-T3 is controlled by the successive redissolution and precipitation of minority phases and it is likely that boundary migration does not play a significant role in the behaviour of the dynamic elastic moduli of these alloys. Consequently, for modelling purposes, we assumed that in absence of microstructural transformations the storage moduli of the studied materials decrease linearly with temperature.

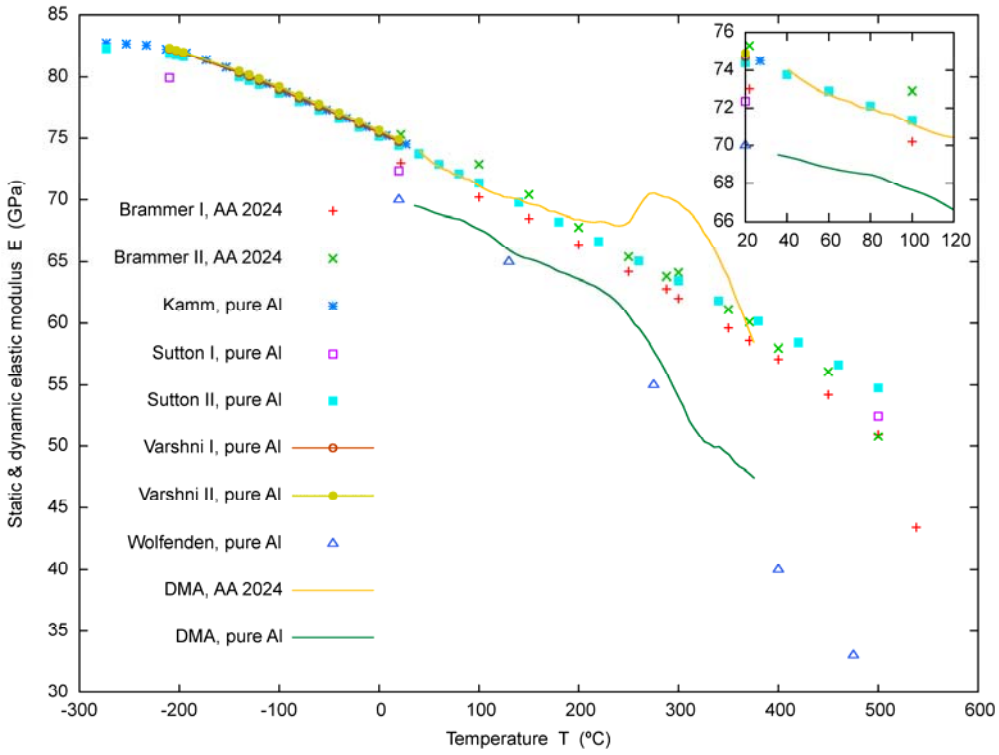

Fig. 28 Elastic modulus *E* (static and dynamic) vs. temperature *T*. Static elastic modulus data was obtained from the literature for pure Al [52, 132, 133] and for AA 2024 [53]. The dynamic elastic modulus was obtained from the literature for pure Al at 80 kHz [55] and from DMA tests for AA 2024-T3 and pure Al at 1 Hz. The data presented in lines with points have been computed using models proposed by the corresponding authors, while all the other series correspond to experimental data.

As per the modelling of the effects of the microstructure, we considered first the influence of GPZ/GPBZ. According to previous research on precipitation sequences and hardening mechanisms on AlZnMg alloys, the mechanical response of these alloys below 220 ºC (and thus the viscoelastic behaviour) is controlled by the presence and decomposition of GPZ [70], e.g. hardening is proportional to GPZ content [81, 86]. This hypothesis is also supported by TEM and DSC studies in the literature and DSC scans performed by us. Namely, this research shows that, on the one side, the microstructure of AA 7075-T6 at RT consists primarily of GPZ [82, 96] and some η' precipitates [71, 82, 96], and that, on the other side, the only transformations occurring below 220 ºC for AlZnMg alloys are basically:

- GPZ formation: at temperatures ranging from RT to 77 ºC (see Table 6).
- GPZ dissolution: at temperatures ranging from 100 to 219 ºC (see Table 6).

Analogously, we assumed that the mechanical response of AlCuMg alloys below 220 ºC is controlled by the presence and decomposition of GPZ/GPBZ, and that the storage modulus grows with GPZ/GPBZ content. On the one hand, the former hypothesis is supported on research by Ozawa [136], which affirms that, for a sample aged up to 150 ºC, GPZ I dissolution and GPZ II formation are close to completion, while presence of θ' is negligible. Thus, as per the θ-phase based ageing sequence, we may assume that the microstructure of AA 2024-T3 below 220 ºC consists primarily of GPZ.

On the other hand, TEM and DSC studies show that the only transformations occurring below 220 ºC for AlCuMg alloys are basically:

- GPZ/GPBZ formation: at temperatures ranging from RT to 90 ºC (see Table 9).
- GPZ/GPBZ dissolution: at temperatures ranging from 100 to 297 ºC (see Table 9).

In addition, it is assumed that GPZ/GPBZ precipitation is complete and no further GPZ/GPBZ formation was possible in the samples. This hypothesis is based, on the one side, on the fact that both alloys under investigation have aged at RT for extended periods of time in the laboratory, thus enabling sufficient time for the completion of GPZ/GPBZ formation. For instance, GPZ precipitation for an AlCuMg alloy is completed after 500 min of natural ageing at RT [8, 137], and GPZ I in AlZnMg alloys form also by natural ageing at RT[12] [16, 87]. On the other side, AA 7075-T6 had been previously subjected as part of its temper to a thermal treatment consisting in ageing at 120 ºC for 24 hours [79, 82], and thus enabling widespread GPZ II precipitation. Moreover, after performing reversibility tests in AA 7075-T6 samples (see Section 2.2.5), we observed that the viscoelastic response is reversible (see Fig. 16), showing that no further microstructural transformations (i.e. irreversible processes), and particularly no GPZ precipitation, occurs between 35 and 100 ºC. Finally, assuming that GPZ formation causes a storage modulus increase, no variation can be observed below 100 ºC in Fig. 15 indicating GPZ precipitation.

The effect of high temperature transformations was also modelled. For this purpose, we considered that:

- For AlZnMg alloys (see Table 6):
  - Precipitation of η': at temperatures ranging from 100 to 306 ºC.
  - Dissolution of η': at 257 ºC.
- For AlCuMg (see Table 9):
  - Precipitation of θ': at temperatures ranging from 200 to 313 ºC.
  - Dissolution of θ': at temperatures ranging from 300 to 550 ºC.
  - Precipitation of S': at temperatures ranging from 120 to 350 ºC.
  - Dissolution of S': at temperatures above 350 ºC.

Therefore, a model is proposed for the storage modulus of AA 7075-T6 and AA 2024-T3, accounting for the effects of the microstructural transformations cited above. In particular, we noticed that, on the one hand, the temperatures reported in the literature for GPZ/GPBZ dissolution are roughly coincidental with an increase in the slope of the storage modulus[13]. On the other hand, the reported temperatures for the formation of η' phase in AlZnMg alloys and θ'/S' phase in AlCuMg[14] alloys agree closely with the storage modulus increase leading to the local maximum (for pure Al there is no transformation and no maximum

[12] Nevertheless, slow hardening has been observed to continue for several years in some AlZnMg alloys at relatively low temperature [70], indicating on-going variations of the microstructure.
[13] The results of some tests present also a slight reduction in the storage modulus slope below 100 ºC. First, we thought it was probably due to GPZ/GPBZ formation, but later we concluded that GPZ/GPBZ formation was complete prior to performing the tests. Thus, we have not been able yet to find a convincing explanation for this.
[14] From now on we may recall phases η', θ' and S' using the term "secondary precipitates".

is observed). Also, the reported temperatures for dissolution of η' and θ'/S' phases are roughly coincidental with the subsequent decrease. Thereby, aside from the linear decrease attributable to the temperature dependence of the elastic constants, we assume that the storage modulus variations below 350 ºC are caused by GPZ dissolution and η' formation and dissolution for AA 7075-T6, or GPZ/GPBZ dissolution and θ'/S' formation and dissolution for AA 2024-T3. Consequently, we propose an analytical model for the evolution of the storage modulus *E'* as a function of temperature *T*, the frequency of the dynamic loading *f*, GPZ/GPBZ concentration, denoted as C_1, and the concentration of the corresponding secondary precipitates, denoted as C_2:

$$E'(f,T) = E'_{RT}(f) + E'_0(f)\left(T - RT\right) + E'_1(f)C_1(T) + E'_2(f)C_2(T) \qquad \text{Eq. 7}$$

where E'_{RT} is the storage modulus at RT, E'_0 accounts for the linear decrease in the storage modulus with temperature, E'_1 reflects the contribution of GPZ/GPBZ, and E'_2 accounts for the contribution of the corresponding secondary phases during precipitation. These coefficients are determined by non-linear fit of the model to experimental data, as will be explained in Section 3.3.

Due to the insufficient resolution of the test data, it is not possible to identify individually the contributions of some overlapping transformations. For this reason and for the sake of model simplicity, for AA 7075-T6 the third term on the right hand side of Eq. 7 accounts for the joint effect of GPZ I and GPZ II. For AA 2024-T3, this term accounts for the joint effect of GPZ I, GPZ II and GPBZ, and the last term accounts for the joint effect of θ' and S'. These trade solutions stem from the yet unknown isolated effect of each of these particular phases on the storage modulus, to the author's knowledge, and because we considered that the resolution of the experimental data was not fine enough to resolve a more complex model in which the contribution of these phase transformations was considered separately[15]. Thus, for AA 7075-T6, C_1 stands for the combined GPZ I plus GPZ II concentration, while for AA 2024-T3, C_1 accounts for the combined GPZ I, GPZ II plus GPBZ concentration, and C_2 for the combined θ' plus S' concentration.

Also, on the one side, the transformations involving phase θ" are not included in the model because θ" are precisely GPZ II [72], which are already accounted for. On the other side, the transformations involving phase S" are disregarded because the existence of this phase is still unresolved [8] and we prioritized the simplicity of the model. Finally, dissolution of η', θ' and S' phases and formation and dissolution of η, θ and S phases, are not accounted for because they may overlap and/or develop mainly out of the test temperature range. Summarizing, the proposed model does not account for the effects of GPZ/GPBZ formation, dissolution of η', θ' and S' phases, nor formation or dissolution of θ", S", η, θ and S phases. Therefore, the validity of the model is limited to temperatures below the onset of secondary precipitates dissolution, i.e. from RT to around 300 ºC.

[15] For example, the reader may consider the case of θ' and S' phase formation, with very similar kinetic parameters.

3.2 MODELLING OF TRANSFORMATION REACTION RATES

For the reaction rate of GPZ/GPBZ dissolution, we considered various models as proposed in the literature. First, we considered this transformation to be a thermally-activated process following Arrhenius behaviour, as stated by Jena [9, 117], thus obeying this expression:

$$\frac{dC_1}{dt} = -C_1 k_0 \exp\left(-\frac{E_A}{KT}\right) \qquad \text{Eq. 8}$$

We considered also a 3D diffusion controlled rate expression, Eq. 2, and a first order diffusion rate expression, Eq. 3[16] [84]. These three rate equations were all implemented in the non-linear fitting process and cross-checked to ascertain which one provided a better fit to experimental data.

As per the modelling of the precipitation rate of η' and θ'/S' phases, only the Avrami equation was used. For AA 2024, it is reasonable to use this equation to represent the evolution of the transformed fraction of the combined θ'/S' phases since the kinetics of formation of these phases exhibit very similar characteristic temperatures, activation energies and Avrami indexes. In any case, we assumed that the driving mechanisms do not change over the whole transformation. Following Papazian's work, the form of the Avrami equation implemented in the proposed model to obtain the transformed fraction was:

$$\left[-\ln(1-\frac{C_2}{C_{2,final}})\right]^{1/n} = \frac{k_0 E_A}{K\phi}\int_{\frac{E_A}{KT}}^{\infty}\frac{e^{-x}}{x^2}dx \qquad \text{Eq. 9}$$

3.3 INTEGRATION OF THE MODEL

The integration of the rate equations for GPZ/GPBZ dissolution and secondary precipitates formation was performed inside the least-squares non-linear fitting of the storage modulus model to experimental data, using a commercial software package[17]. For this purpose, a very efficient numerical procedure was designed. The full procedure is presented in Annex C, while it can be summarized as follows:

- Procedure start.
- Read the experimental DMA data obtained for a given sample, and select:
  - The desired frequencies to be analysed.
  - The range of experimental data to be considered for the non-linear fit.
- Read the initial estimates for the model coefficients and kinetic parameters, which will be used as starting values in the minimization procedure.

[16] From now on, in the main text or figures we may refer to Eq. 2 and Eq. 3 as Pap. I and Pap. II, respectively.
[17] MATLAB from The MathWorks Inc.: http://www.mathworks.com

- Select the GPZ/GPBZ dissolution rate equation to be used (Eq. 2, 3 or 8).
- Define the objective function to be minimized, Eq. 10:

$$\psi = \frac{1}{N_{\exp}} \sum_{1}^{N_{\exp}} \left(\frac{E'_{\mathrm{mod}} - E'_{\exp}}{E'_{\exp}} \right)^2 \qquad \text{Eq. 10}$$

  where N_{exp} is the number of experimental observations. The procedure consists in:
  - Integration of Eq. 7 using the initial values provided for the model coefficients and kinetic parameters for the selected rate equations.
  - Determination of the quadratic error between the storage modulus measured by the DMA and that computed by the model at each frequency and temperature step.
  - Return of the sum of those quadratic errors.
- Call the built-in minimization routine to minimize the objective function.
- Save the model coefficients and kinetic parameters resulting from the minimization procedure.
- Plot graphs of the experimental and computed storage modulus, the temperature- and time-evolution of the concentration of GPZ/GPBZ and secondary precipitates, etc.
- End of procedure.

This procedure allowed us to treat the pre-exponential coefficients, the activation energies and the Avrami indexes in the rate equations as fitting parameters, in addition to the four model coefficients E'_{RT}, E'_0, E'_1 and E'_2 for each frequency, for a total of 5 + 4*z* fitting parameters (being *z* the number of frequencies solved simultaneously). For each simulation reported in this paper, five frequencies were analysed (100, 30, 10, 3 and 1 Hz), for a total of 25 fitting parameters.

3.4 MODEL RESULTS FOR AA 7075-T6

In this section, the results obtained for AA 7075-T6 after integration of the rate equations and fitting of the storage modulus model to experimental data are presented. Table 19 shows the initial values of the fitting parameters as used in this solving process.

Table 19 Initial parameters for the integration and fitting of the transformation rate equations and the proposed storage modulus model, for AA 7075-T6.

Parameter	Value	Reference
Initial GPZ concentration	5%	[79, 81, 87, 88]
E_A for GPZ dissolution	1.21 eV/atom	[82, 84, 96]
k_0 for GPZ dissolution	1.10×10^{10} s^{-1}	N/A
Final η' concentration	5%	N/A
E_A for η' formation	1.26 eV/atom	In disagreement with [86]
k_0 for η' formation	2.28×10^{9} s^{-1}	N/A
Avrami index for η' formation	1.00	In disagreement with [86]
Coef. E'_{RT} (for all frequencies)	70.0×10^{9} Pa	Elastic modulus for Al is 72.4 GPa
Coef. E'_0 (for all frequencies)	-1.5×10^{7} Pa·°C^{-1}	[52, 53, 55, 132, 133]
Coef. E'_1 (for all frequencies)	1.0×10^{10} Pa	N/A
Coef. E'_2 (for all frequencies)	1.0×10^{10} Pa	N/A

These values were either directly taken or calculated from data available in the literature, or were simply the result of an educated guess:

- GPZ dissolution:
  - Initial GPZ concentration: Data on particle densities, sizes and shapes for AA 7075-T6 was used to calculate this value (see Sections 1.6.1 and 1.8). The particle surface density was assumed to be 4×10^{4} per μ^2 [79, 88]. This is equivalent to a volume particle density of 8×10^{6} particles per μ^3, which agrees with values measured by Hansen [87]. Since GPZ are more abundant than η' precipitates in AA 7075-T6 at RT, we assumed that 75% of those particles are GPZ. Finally, we considered that GPZ are spheres of 2.5 nm diameter [81] (this is close to the average diameter in the literature), resulting in an initial GPZ volume concentration of roughly 5%. This is consistent also with the atomic Zn content (2.59%) and Mg content (2.99%). After the integration process and with the temperature increase, the final GPZ concentration will be 0%, which is reasonable considering that GPZ I dissolve and GPZ II transform into η' phase.
  - Activation energy: The initial value is close to the average of the activation energies in the literature (see Table 11): 1.17 eV/atom.
  - Pre-exponential coefficient: No references were found reporting about this value, so we used the same value as for GPZ dissolution in AA 2024-T3 (see Section 3.5).
- η' phase formation:
  - Final η' phase concentration: To the author's knowledge, there is no data on this issue in the literature. In view of the value calculated for the initial GPZ concentration, we assumed a final concentration of 5% for the η' phase. Also, although the η' phase may be present in AA 7075-T6 at RT, an initial concentration of 0% was assumed. The reason is that what has physical significance is the magnitude of the concentration variation, because it causes the observable changes in modulus, rather than the particular initial and final absolute concentrations. These are only relevant for determining the relative

contribution of η' precipitates to the total storage modulus, and thus they only affect the fit value of E'_{RT}.

- Activation energy: No simulation converged when initialized with the activation energies reported by Yannacopoulos [86]. Higher activation energies were used instead, and their appropriateness is discussed in Section 4.2.3.
- Pre-exponential coefficient: No references were found reporting about this value, so we used the same value as for secondary precipitation in AA 2024-T3 (see Section 3.5).
- Avrami index: No simulation converged when initialized with the Avrami indexes reported by Yannacopoulos [86]. Lower indexes were used instead, and their appropriateness is discussed in Section 4.2.3.

- Model coefficients:
  - E'_{RT}: The initial value is close to the typical static elastic modulus of pure Al (72.4 GPa) and to the storage modulus measured for AA 7075-T6 at RT at any frequency.
  - E'_0: The initial value is of the order of magnitude of the static elastic modulus temperature gradients for pure Al [52, 132, 133] and AA 2024 [53], and also of the order of magnitude of the dynamic elastic modulus temperature gradient for AA 6061 [55].
  - E'_1: The initial value was arbitrary chosen bearing in mind that the term $E'_1 \cdot C_1$ be of an order of magnitude 0.1–10 GPa.
  - E'_2: The initial value was arbitrary chosen bearing in mind that the term $E'_2 \cdot C_2$ be of an order of magnitude 0.1–10 GPa.

The procedure established for validating the simulations was based on the fitted values of the kinetic parameters. For each data set corresponding to a test, a series of around 15 simulations were run. The first simulation integrated the model from RT to 100 ºC. In each subsequent simulation the upper limit of integration was increased in steps of 15 ºC approximately, such that for the last simulation the studied temperature range was about RT–325 ºC. Obviously, for the first simulations in this sequence the results exhibit high instability because only a small fraction (or no fraction at all) of GPZ dissolution and secondary precipitation is manifested in the experimental storage modulus data, so the error in the fitting and determination of the kinetic parameters is large. Thus, the criterion for acceptance of the results provided by one of these simulation sets was that the kinetic parameters exhibit stability (i.e. a constant value) in a major part of the set, and especially in the last five simulations (see Fig. 29). This way the robustness of the solution provided by the integration process is granted. Attention must be paid also to simulations with the upper integration limit above 300 ºC, because secondary precipitates dissolution may begin and, as this is not accounted for by proposed model, the solution may be affected.

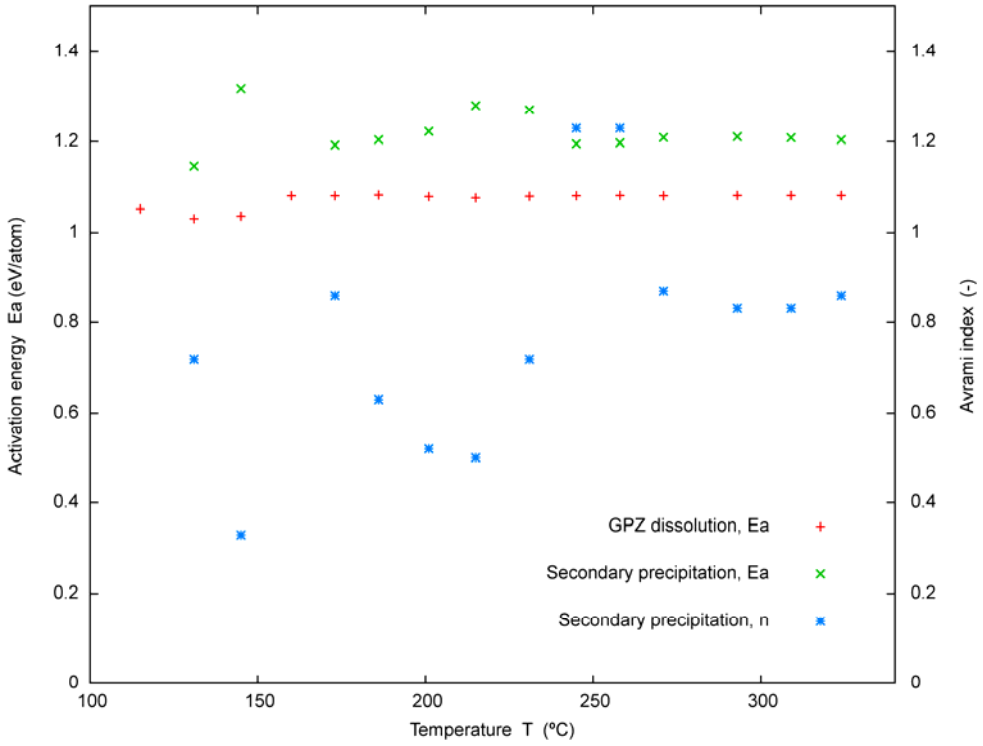

Fig. 29 Activation energies E_A for GPZ dissolution and secondary precipitation, and Avrami index for secondary precipitation vs. temperature T of the upper integration limit, for a sequence of simulations covering from RT–100 ºC to RT–325 ºC.

Fig. 30 shows the temperature dependence of the computed storage modulus compared to experimental data, for a test on AA 7075-T6 at a frequency of 10 Hz.

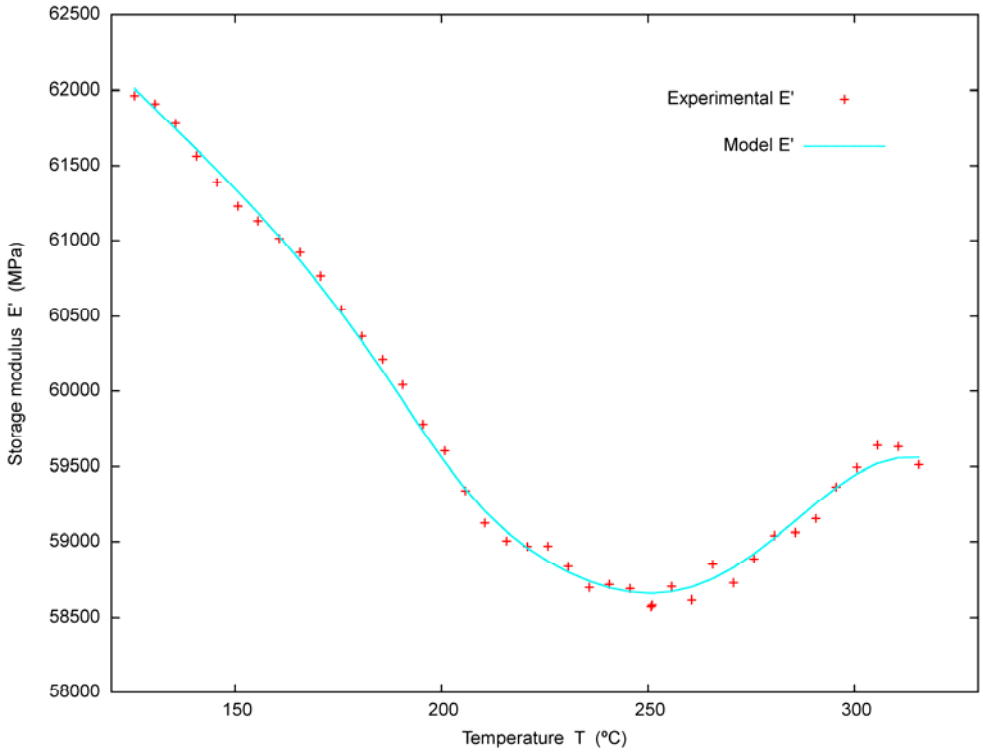

Fig. 30 Experimental and computed storage modulus E' vs. temperature T, for AA 7075-T6, at an excitation frequency of 10 Hz.

Fig. 31 shows the evolution of the concentrations of GPZ and η' phase with temperature, as well as the storage modulus vs. time for another test on AA 7075-T6, as computed using the proposed model. Both concentration curves exhibit a characteristic sigmoidal shape.

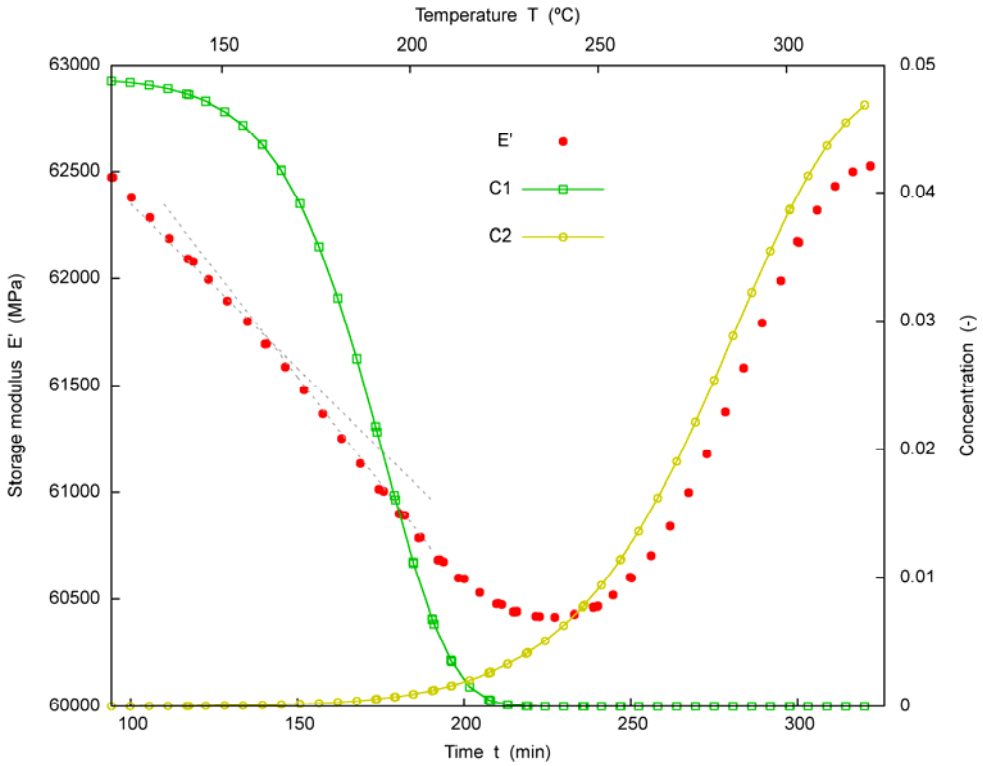

Fig. 31 Model results of storage modulus E' vs. time t, and GPZ concentration C_1 and η' phase concentration C_2 vs. temperature T. These data correspond to AA 7075-T6 at a frequency of 100 Hz.

For AA 7075-T6, the final values of the physical parameters of interest (i.e. the pre-exponential coefficient and activation energy of GPZ dissolution when using Jena's and Papazian's rate equations, as well as those of η' phase formation, together with the Avrami exponent) are listed in Table 20.

Table 20 Best-fit values obtained after integration and fitting of the transformation rate equations and the proposed storage modulus model, for AA 7075-T6.

		Model used for GPZ dissolution rate		
Transformation	Kinetic parameter	Jena (Eq. 8)	Pap. I (Eq. 2)	Pap. II (Eq. 3)
GPZ dissolution	Activation energy, E_A	1.21 eV/atom	1.13 eV/atom	1.06 eV/atom
	Pre-exponential coef., k_0	1.15×10^{10} s^{-1}	1.38×10^{10} s^{-1}	1.38×10^{10} s^{-1}
η' formation[a]	Activation energy, E_A	1.26 eV/atom	1.26 eV/atom	1.26 eV/atom
	Pre-exponential coef., k_0	8.76×10^{9} s^{-1}	8.83×10^{9} s^{-1}	8.38×10^{9} s^{-1}
	Avrami index, n	0.77	0.84	0.76

[a] The fitting of the Avrami equation parameters varies if the GPZ dissolution rate equation is changed.

The coefficients E'_0, E'_1 and E'_2 of the storage modulus model are plotted as a function of the excitation frequency in Fig. 32. E'_{RT} is not plotted because it is virtually constant with frequency.

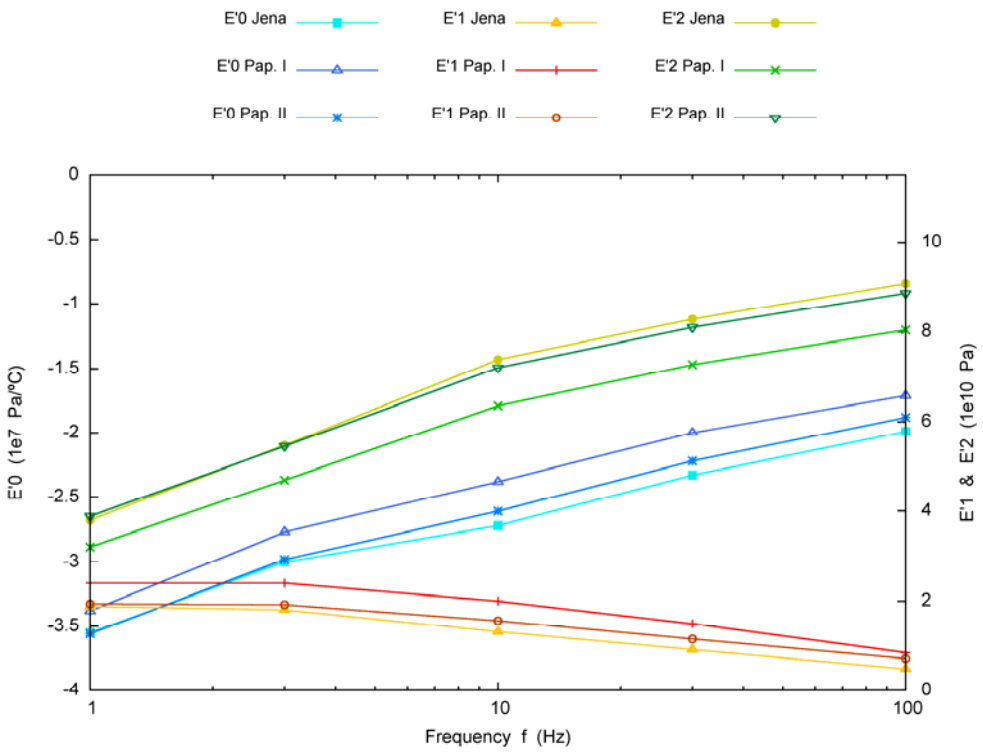

Fig. 32 Coefficients E'_0, E'_1 and E'_2 of the storage modulus model vs. frequency f for AA 7075-T6.

3.5 MODEL RESULTS FOR AA 2024-T3

In this section, the results obtained for AA 2024-T3 after integration of the rate equations and fitting of the storage modulus model to experimental data are presented. Table 21 shows the initial values of the fitting parameters as used in this solving process.

Table 21 Initial parameters for the integration and fitting of the transformation rate equations and the proposed storage modulus model, for AA 2024-T3.

Parameter	Value	Reference
Initial GPZ/GPBZ concentration	5%	[101]
E_A for GPZ/GPBZ dissolution	1.06–1.27 eV/atom	[9, 73, 84]
k_0 for GPZ/GPBZ dissolution	1.10×10^{10} s^{-1}	[1, 9, 73]
Final θ'/S' concentration	5%	N/A
E_A for θ'/S' formation	1.11 eV/atom	[9, 73, 75, 77, 84, 98, 125, 126]
k_0 for θ'/S' formation	2.28×10^{9} s^{-1}	[84]
Avrami index for θ'/S' formation	1.10	[84]
Coef. E'_{RT} (for all frequencies)	70.0×10^{9} Pa	Elastic modulus for Al is 72.4 GPa
Coef. E'_0 (for all frequencies)	-1.5×10^{7} Pa·°C^{-1}	[52, 53, 55, 132, 133]
Coef. E'_1 (for all frequencies)	1.0×10^{10} Pa	N/A
Coef. E'_2 (for all frequencies)	1.0×10^{10} Pa	N/A

These values were derived following a similar procedure as that for AA 7075-T6 (see Section 3.4):

- GPZ/GPBZ dissolution:
  - Initial GPZ/GPBZ concentration: The microstructure of AA 2024-T3 at RT consists mainly of GPZ/GPBZ. GPBZ volume fractions are around 0.4–3.2% [101]. We assumed that the initial GPZ concentration may be of a similar order of magnitude, and that the total initial combined fraction is 5%, such that symmetry is maintained with the case of AA 7075-T6. This is also consistent with the alloy atomic Cu content (1.95%) and Mg content (1.55%).
  - Activation energy: The initial values are respectively close and equal to the average of the activation energies in the literature (see Table 12): 1.27 eV/atom.
  - Pre-exponential coefficient: The initial value is that reported by Jena [9], which is of the same order of magnitude of values reported by other researchers.
- θ'/S' phase formation:
  - Final θ'/S' phase concentration: The θ' and S' phases are virtually not present in AA 2024-T3 at RT. That is why we may assume that the concentration of these phases is null, initially. Also, S phase volume fractions are around 0.7–3.8% [101]. So we assumed that the final phase concentrations of both θ' and S' may be of a similar order of magnitude, and that the total final combined fraction is 5%, such that symmetry is again maintained with the case of AA 7075-T6.
  - Activation energy: The initial value is close to the averages of the activation energies in the literature for θ' and S' phase formation (see Table 12): 1.14 and 1.37 eV/atom.
  - Pre-exponential coefficient: The initial value is equal to the average of the coefficients reported by Papazian for θ' phase formation, and close to that reported for S' phase formation [84].
  - Avrami index: The initial value is equal to the Avrami index reported by Papazian [84].
- Model coefficients: These values were derived following the procedure explained in Section 3.4.

For validating the simulations, we used the same procedure as in Section 3.4, based on the values of the kinetic parameters. On the one hand, Fig. 33 shows an example of the model results after the fitting procedure. Particularly, it is presented the temperature dependence of the computed storage modulus compared to experimental data, for a test on AA 2024-T3 at an excitation frequency of 3 Hz.

On the other hand, Fig. 34 shows the evolution of the concentrations of GPZ/GPBZ and θ'/S' phases with temperature and the storage modulus vs. time for another test on AA 2024-T3, as computed using the proposed model and approach. Both concentration curves exhibit a characteristic sigmoidal shape.

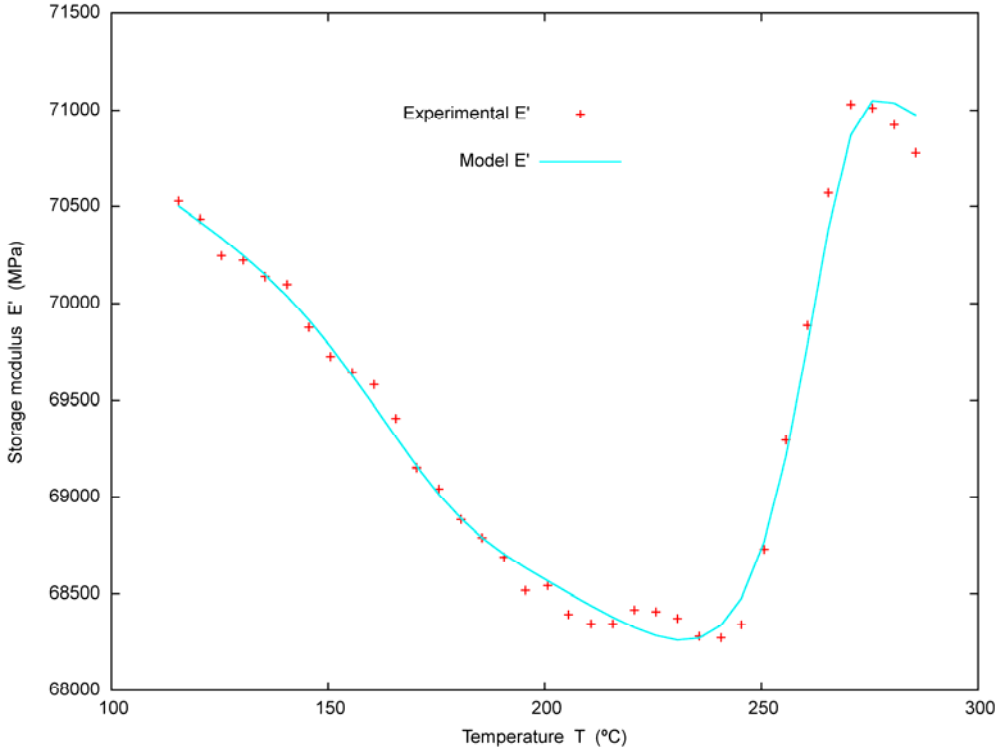

Fig. 33 Experimental and computed storage modulus *E'* vs. temperature *T*, for AA 2024-T3, at an excitation frequency of 3 Hz.

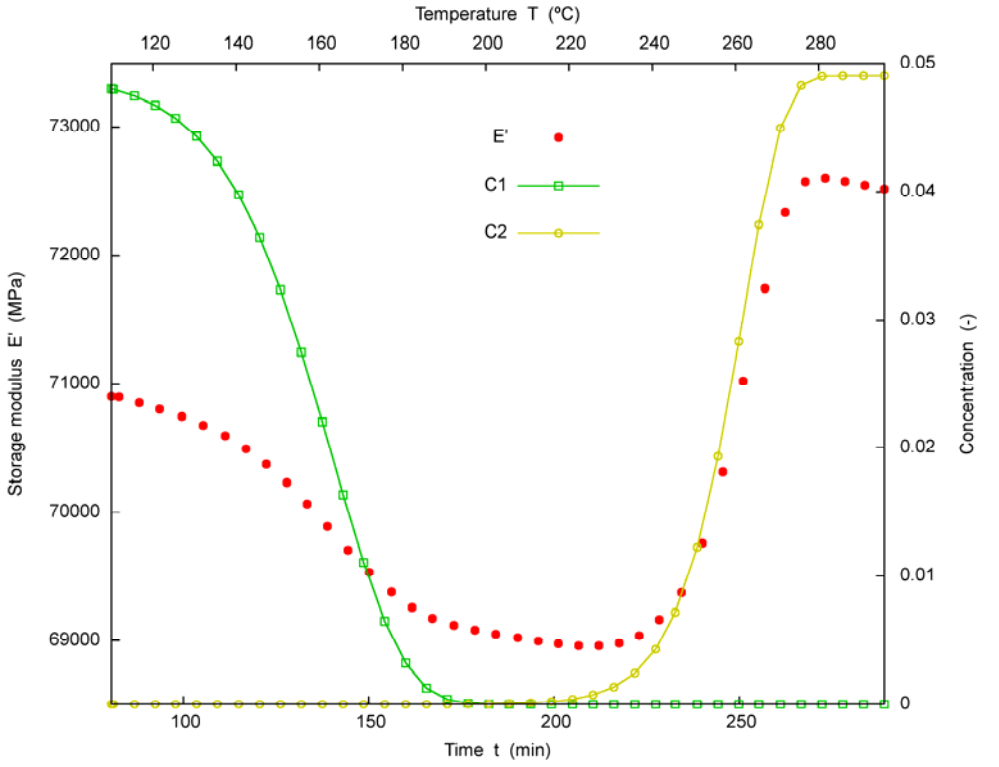

Fig. 34 Model results of storage modulus *E'* vs. time *t*, and GPZ/GPBZ concentration C_1 and θ'/S' phases concentration C_2 vs. temperature *T*. These data correspond to AA 2024-T3 at a frequency of 30 Hz.

For AA 2024-T3, the final values of the physical parameters of interest (i.e. the pre-exponential coefficient and activation energy of GPZ/GPBZ dissolution when using Jena's and Papazian's rate equations, as well as those of θ'/S' phases formation, together with the Avrami exponent) are listed in Table 22.

Table 22 Best-fit values obtained after integration and fitting of the transformation rate equations and the proposed storage modulus model, for AA 2024-T3.

		Model used for GPZ/GPBZ dissolution rate		
Transformation	Kinetic parameter	Jena (Eq. 8)	Pap. I (Eq. 2)	Pap. II (Eq. 3)
GPZ/GPBZ dissolution	Activation energy, E_A	1.18 eV/atom	1.07 eV/atom	0.97 eV/atom
	Pre-exponential coef., k_0	4.53×10^{10} s^{-1}	1.00×10^{10} s^{-1}	6.11×10^{9} s^{-1}
θ'/S' formation[a]	Activation energy, E_A	1.23 eV/atom	1.23 eV/atom	1.25 eV/atom
	Pre-exponential coef., k_0	1.88×10^{10} s^{-1}	1.75×10^{10} s^{-1}	2.75×10^{10} s^{-1}
	Avrami index, n	1.29	1.30	1.30

[a] The fitting of the Avrami equation parameters varies if the GPZ/GPBZ dissolution rate equation is changed.

The coefficients E'_0, E'_1 and E'_2 of the storage modulus model are plotted as a function of the excitation frequency in Fig. 35. E'_{RT} is not plotted because it is virtually constant with frequency.

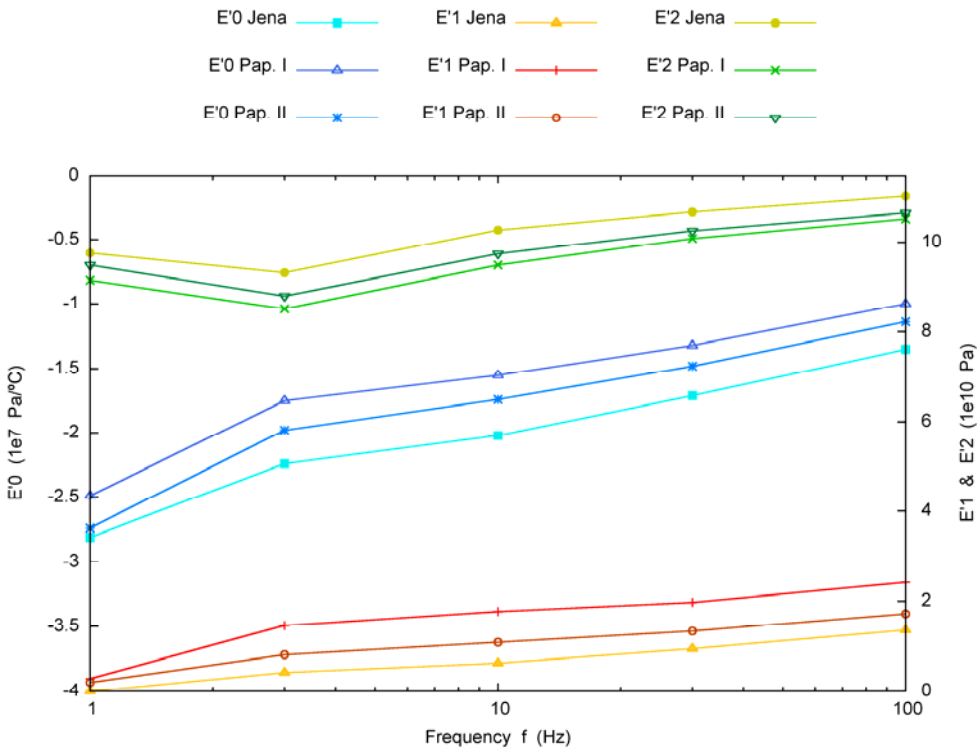

Fig. 35 Coefficients E'_0, E'_1 and E'_2 of the storage modulus model vs. frequency f for AA 2024-T3.

3.6 MODEL RESULTS FOR PURE ALUMINIUM

In this section, the results obtained for pure Al after fitting of the storage modulus model to experimental data are presented. First, Table 23 shows the initial values of the fitting parameters. Contrary to the

previous cases, for pure Al no phase transformations take place, so the terms of the model that account for the contribution of GPZ/GPBZ and secondary precipitates were not activated. Thus, the only initial values that apply are E'_{RT} and E'_0, which were derived following the procedure explained in Section 3.4.

Table 23 Initial parameters for the fitting of the proposed storage modulus model, for pure Al.

Parameter	Value	Reference
Coef. E'_{RT} (for all frequencies)	70.0×10^{9} Pa	Elastic modulus for Al is 72.4 GPa
Coef. E'_0 (for all frequencies)	-1.5×10^{7} PaK^{-1}	[52, 53, 55, 132, 133]

In this case, the goal of the simulations was simply to compute the rate of storage modulus loss with temperature in the temperature interval 35–100 ºC, for each frequency. These values are shown in Table 24, and are checked against those obtained by linear regression of the DMA data (from Table 16), such that performance of the fitting may be assessed. The error is only about 2.2% in average, and is probably due to slight differences in the evaluated temperature intervals.

Table 24 Rate of storage modulus loss with temperature for pure Al.

	Storage modulus temperature gradient [MPa·°C^{-1}]	
Frequency [Hz]	From linear regression of DMA data	From model results
100	-23.1±0.5	-22.08
30	-25.2±0.4	-24.59
10	-26.4±0.5	-25.80
3	-27.9±0.5	-27.51
1	-29.7±0.8	-29.51

4 DISCUSSION

In this chapter, the experimental results, the model results and the main findings derived from this research work are discussed.

4.1 DISCUSSION OF EXPERIMENTAL RESULTS

The experimental results have shown that the viscoelastic responses of the studied alloys are qualitatively similar, and that they depend significantly on environmental conditions such as temperature and the excitation frequency, and also on the microstructure, as expected. First, the DMA results on storage and loss moduli are discussed. Next, possible relaxation phenomena contributing to the internal friction are presented. Finally, the results of the application of the TTS principle are commented.

4.1.1 Storage modulus

The absolute values of the experimental storage modulus for AA 7075-T6, AA 2024-T3 and pure Al at RT are greater than those reported by Das [54] for unreinforced AA 6061, but are similar to the values this author reports for SiC particle reinforced AA 6061-T6 matrix composites, and to other values reported in the literature for pure Al [55-57]. Das [54] could not find a satisfactory explanation for the discrepancy between his results for unreinforced AA 6061 and those in the literature and ignored this fact. The experimental dynamic elastic moduli of AA 2024-T3 and pure Al at RT also compare well with static and dynamic elastic modulus data available in the literature for these materials [52, 53, 55, 132, 133] (see Fig. 28). This is expected since frequency has very little effect at low temperatures and the contribution of the loss modulus to the dynamic modulus is very small.

The observed decrease as early as at RT of the storage modulus with temperature for both AA 7075-T6, AA 2024-T3 and pure Al is explained by the dependence of the elastic stiffness constants (and in particular, the elastic modulus) on temperature, which is a well known phenomenon for metals, and particularly for aluminium [52, 53, 55, 132, 133]. This decrease of the storage modulus is also reported in AA 6061 and AA 6061-T6 [54]. Assuming linearity (only for Das' data this seems not very reasonable), our DMA results and all the storage modulus and static and dynamic elastic modulus data series by the previous researchers exhibit similar slopes with temperature in the vicinity of RT (see Fig. 28). Even for Wolfenden's data [55] the slope is similar at RT if we consider only the first two points in his data series, which are the ones closer to RT. As shown also in Fig. 28, Wolfenden's data compare well with our DMA results for pure Al. Both series show a change of slope that Wolfenden probably did not notice due to his data being so scattered. Thus, we consider that this researcher erroneously assumed linearity in an excessively broad temperature range, leading to a larger negative slope.

As expected, the studied materials seem stiffer at higher frequencies [1], i.e. the decrease of the storage modulus with temperature at low frequencies is larger compared to that at high frequencies (see Fig. 9 and 17). This is typically explained by the Arrhenius-type behaviour of the relaxation rate ν_r:

$$\nu_r = \nu_{r0} \exp\left(-\frac{E_A}{KT}\right) \qquad \text{Eq. 11}$$

which causes a reduction of the mechanical relaxation time as temperature increases [1, 129]. That is, at lower frequencies, with increasing temperature, the shorter relaxation times cause responses with larger phase lags, resulting in a greater decrease of the storage modulus. The Arrhenius behaviour of the relaxation rate explains also why the viscoelastic behaviour becomes more prominent[18] as temperature increases, i.e. why the storage and loss moduli depend more significantly on the excitation frequency at higher temperatures. This has already been observed in amorphous alloys [129].

The experimental results on storage modulus expose also the influence of the microstructure and phase transformations on the viscoelastic behaviour, in agreement with previous research [1, 54]. This issue is discussed in detail in Section 4.2.2. Finally, the isothermal curves of storage modulus vs. frequency (see Fig. 10 and 18) confirm some of the conclusions reported above. Namely, the storage modulus increases with frequency for all the studied temperatures, and this increase is more pronounced as temperature increases, i.e. the higher the temperature, the steeper the slope. Further comments on these curves appear in Section 4.1.3.

4.1.2 Loss modulus & loss tangent

The loss modulus and loss tangent are commented simultaneously in this section because for the studied alloys these parameters exhibit qualitatively the same behaviour, and because both are intimately linked to the internal friction. The absolute values of the experimental loss modulus and loss tangent for AA 7075-T6 and AA 2024-T3 at RT are similar to those reported by Das [54] for 20 vol.% SiC fibre, AA 6061-T6 matrix composite, at low temperatures. Our loss moduli grow faster with temperature, though. For example, the loss moduli are 50 to 100% larger and the loss tangent are 70 to 200% larger, for 100 and 1 Hz respectively, at a temperature of 375 ºC. The differences may be due to Das using a non-constant (resonant) frequency or a faster heating rate in their DMA scans, but this cannot be verified because the author does not report on these matters.

The loss moduli and loss tangents are small (and virtually constant) at low temperatures, indicating that the internal friction is low (see Fig. 13 and 21). The ramp increase they both exhibit reflects that more energy is dissipated through viscoelastic processes, i.e. internal friction, as temperature increases. For the loss modulus, the ramp starts at about 120–140 ºC for AA 7075-T6 and 200–220 ºC for AA 2024-T3,

[18] In other words, the viscoelastic behaviour obtained over a short frequency interval at high temperature is equivalent to that obtained for a longer interval at a lower temperature [116].

and for the loss tangent, it starts at about 200 ºC for AA 7075-T6 and 220 ºC for AA 2024-T3. Possible relaxation phenomena that may cause this raise of internal friction are commented in Section 4.1.3. The Arrhenius behaviour of the relaxation rate explains why the presumed internal friction peak causing the ramp increase, and thus the beginning of the ramp itself, are shifted to higher temperatures as frequency increases. It explains also why the slopes of these ramps decrease as the mechanical excitation frequency is increased, and this, together with the delay in the ramp increase, is the reason why at higher temperatures (e.g. above 160 ºC for AA 7075-T6 above 275 ºC for AA 2024-T3) the loss modulus and loss tangent are smaller for higher frequencies of mechanical excitation. The reason is that the effect of reducing the frequency is similar to increasing the temperature. This is consistent with the behaviour of the storage modulus as explained above. That is, at higher frequencies, materials behave stiffer and have less energy losses. Conversely, the loss modulus is smaller for lower frequencies at low temperatures. A hypothesis for the origin of this unexpected behaviour is explained below.

On the one side, Zhu [24] reported for an aluminium alloy that the fatigue strength decreases with temperature, and that this behaviour of fatigue strength follows closely the temperature dependence of yield and tensile strength. Also, Liaw [27] suggested that fatigue limits and lives of steels decrease due to the temperature increase caused by plastic deformation. On the other side, the viscoelastic response plays a key role both on the fatigue response and the yield stress behaviour [1]. Thus, it is likely that the decrease of yield and fatigue behaviour observed in aluminium alloys as temperature increases be due to the internal friction increase. Extrapolating this assumption to the studied alloys, in view of the internal friction results in the test temperature range, the yield and fatigue strength of AA 7075-T6 and AA 2024-T3 may also decrease with temperature.

Furthermore, if it is assumed that the internal friction variations with loading frequency may also modify the fatigue response, our results suggest that below 150 ºC the yield and fatigue strength will diminish with increasing frequency, while at high temperatures these properties will increase. There is controversy about the effect of frequency on the fatigue response. This is why our presumptions agree with part of the research reported in the literature, but not with all of it. For example, there is agreement with results from low frequency investigations for aluminium alloy RR58 at 150 ºC [39] and for AA 2650-T6 at 175 °C [40], pointing that fatigue life is sensitive to frequency and that it increases with loading frequency. There is agreement also with results for E319 cast aluminium alloy at 150 and 250 ºC, pointing that fatigue life at 20 kHz was 5 to 10 times longer than that at 75 Hz [24]. Nevertheless, this behaviour is attributed to environmental effects on FCG rate, rather than intrinsic temperature or frequency effects.

The isothermal curves of loss modulus vs. frequency confirm that, in the studied intervals, the loss modulus for a given frequency increases with temperature (see Fig. 12 and 20). Generally, these curves may exhibit one or more peaks. In this case, one peak can be observed only for AA 7075-T6 in the curves for 365 and 375 ºC. In view of the shapes of the other high temperature curves, we can presume that they all present this peak but it is centred at a frequency below the studied range. Our results would then agree with the theory, which states that peaks shift progressively towards lower frequencies and become broader (e.g. due to a wider distribution of relaxation times) with decreasing temperature [1, 45, 129]. This

is again explained by the Arrhenius-type behaviour of the relaxation rate, resulting in larger mechanical relaxation times and less pronounced relaxation behaviours as temperature diminishes. These curves illustrate also the differences in the behaviour at low and high temperatures commented when discussing the loss modulus vs. temperature curves. We now may presume that this is caused by the advent of a peak centred at a frequency above the studied range. This peak, in the temperature domain, would be located below the studied temperature range and would explain the observed intersection of the loss modulus vs. temperature curves.

To check whether the suggested peaks exist out of the studied frequency range, it became evident the need for acquiring loss modulus data at a wider range of frequencies than 1 to 100 Hz. Thus, we also performed DMA tests at frequencies equal to and slightly higher than the minimum nominal frequency of the used DMA (0.01 Hz), and at frequencies equal to and slightly smaller than the maximum nominal frequency (200 Hz). Unfortunately, the results did not seem reliable. They exhibited high instability and did not follow the common trends observed for the frequencies 100, 30, 10, 3 and 1 Hz. This was probably due to the DMA working close to its operational limits. In any case, provided that these tests be successful, it is likely that many peaks would still not be observable in the 0.01–200 Hz range, due to the Arrhenius-type behaviour of the relaxation rate. For an adequate characterization of these peaks, tests may be necessary at frequencies ranging from several orders of magnitude below 0.01 Hz to several orders of magnitude above 100 Hz. To perform these tests at very low and very high frequencies, testing equipment other than the DMA would be necessary.

In the temperature domain, tests below RT to identify the peak suggested above are not possible given the present capacities of the DMA we used[19]. Also, tests reaching higher temperatures were performed to check whether peaks observed in the frequency domain become narrower and more prominent, and also to check, in the temperature domain, whether the loss modulus presents a peak at temperatures higher than 375 ºC, in opposition to the observed monotonical behaviour below 375 ºC. Most of the attempts were not successful because the samples yielded. Some tests up to 450 ºC succeeded, though, but yet no peaks were observed. Hence, these results were disregarded, too.

Finally, we must analyse the behaviour of the loss tangent. Maxima in the loss tangent are related to transformation processes [54], but the DMA data presented here show a monotonically increasing behaviour. This is due to the superposition of the peaks corresponding to successive microstructural transformations. This fact is hidden in the AA 7075-T6 data (see Fig. 13), but it is revealed in the AA 2024-T3 case (see Fig. 21) where quasi-local minima are observed at about 220°C and 300°C, roughly coincident with the completion of GPZ/GPBZ dissolution and θ'/S' formation, respectively.

[19] Cryogenic cooling in the Liquid Nitrogen-RT range is available for the TA Instruments Q800 DMA and may be acquired in the future.

4.1.3 Relaxation phenomena

For the ideal case of the standard anelastic solid (for which a single relaxation process takes place), the isothermal curves of storage modulus vs. frequency would exhibit a sigmoidal shape, and for multiple relaxations these curves would be a composition of sigmoidals [1]. Also, for frequencies tending to zero, the storage modulus would be at its minimum (relaxed case), while at very high frequencies it would be at its maximum (unrelaxed case), i.e. the material behaves stiffer. While the presented isothermal curves (see Fig. 10 and 18) do not deviate largely from this expected behaviour, it cannot be concluded whether their shape is sigmoidal or a combination of sigmoidals, and thus whether only one or more relaxation processes are taking place.

As regards to the isothermal curves of internal friction vs. frequency (see Fig. 12 and 20), a peak appears when the test time scale (which is inversely proportional to the applied frequency) matches the time scale for a relaxation process [1, 45, 138]. For the obtained isothermal curves, a peak can be observed only for AA 7075-T6 in the curves at 365 and 375 ºC, which are centred approximately at a frequency of 2.5 and 2.8–3.4 Hz, respectively. For low temperatures, where peaks are broader, we cannot observe the viscoelastic behaviour so well. Anyway, in DMA tests the microstructure and therefore the properties are not stabilized. Thus, the observed peaks may be caused also by transient effects or changes in the microstructure during the tests. That is, the variation of the relaxation behaviour associated to temperature/frequency variations is superimposed to that associated to on-going transformations and variation of precipitate concentration. In addition, the results obtained on the internal friction spectrum correspond to a very narrow frequency range. It would be optimal to have data at a wider range of frequencies, but this was not possible, as explained in Section 4.1.2. Consequently, it is not trivial to determine the exact number and nature of the relaxation processes taking place or to derive more reliable conclusions. Further insight on this issue is given in Section 4.2.5, though.

So far, we can only presume that the measured internal friction may be due to common phenomena reported in the literature for alloys similar to those studied here. For example, for AA 7075-T6 and AA 2024-T3, relaxations associated to atom groupings within GPZ/GPBZ may be present [62]. For the particular case of AA 2024-T3, the internal friction may be caused for example by relaxations associated to θ′ phase [1], once θ′ phase precipitation begins, and relaxations associated to θ phase [63], provided that some θ phase precipitated during the DMA tests (we could not confirm this point). For AA 7075-T6, internal friction may be due to discontinuous precipitation [1] and also secondary phases like in AA 2024-T3. Although AA 2024-T3 and the pure Al samples (supplied in the H24 temper) feature certain degree of cold-work, the Bordoni relaxation is probably not present since it occurs at temperatures well below the studied range. Finally, the alloys and pure Al present also relaxations related to grain boundaries [1, 135]. On the contrary, the Zener relaxation is probably not significant for the studied alloys because the number of atoms in solution is minimal, as GPZ/GPBZ precipitation is complete prior to the tests.

Consequently, the most probable cause for the large increase in internal friction starting at 200 ºC for AA 7075-T6 and 220 ºC for AA 2024-T3 is the onset of relaxation effects related to secondary precipitates and grain boundaries, and to discontinuous precipitation too for AA 7075-T6. Finally, the internal friction peak observed for pure Al samples is sure related mainly to grain boundaries, as it is virtually identical to that reported in the literature, i.e. it is centred at 300 ºC and maximum for 1 Hz [1]. The activation energy computed for this relaxation process is 1.97 eV/atom, higher than that in the literature (1.48 eV/atom).

4.1.4 TTS principle results

For the storage modulus it was possible to identify a master curve for a low temperature region and, for the storage and loss moduli, another curve for a high temperature region. These regions are roughly coincidental with the stable regions (i.e. those where no microstructural transformation occurs) that can be observed typically in DSC thermograms for AA 7075-T6 and AA 2024-T3, and which were confirmed in the modelling of the storage modulus. The first stable region ranges approximately from RT to 100–150 ºC, which is reasonable assuming that GPZ/GPBZ formation is already complete prior to the tests (this is justified in Section 3.1) and that GPZ/GPBZ dissolution has not begun. The second stable region corresponds to temperatures around 350 ºC, before the onset of equilibrium phases dissolution. It was not possible to obtain any master curve using the TTS approach for data between 150 and 300 ºC, probably because this is not a stable region and on-going transformations overlap there.

Summarizing, the different temperature dependencies of the shift factor for the identified master curves, manifested by different activation energies in the Arrhenius expression, is due, on the one hand, to the occurrence of microstructural changes between the mentioned temperature regions (e.g. GPZ/GPBZ dissolution and secondary precipitation). On the other hand, the differences might also be caused by different relaxation mechanisms in one region respect to the other (the material changes, so it does the relaxation mechanisms). Also, as expected, the apparent activation energy for the low temperature region is smaller than that for the high temperature region. Unfortunately, it is not possible to derive further conclusions from the values of these activation energies. Finally, to better verify the validity of the obtained master curves, again it would be convenient to measure the storage and loss moduli at a wider frequency range than 1 to 100 Hz. For example, adding moduli data at higher and smaller frequencies may make more evident the overlapping of the data series, facilitating the visualization of the master curves. Unfortunately, results obtained for frequencies close to the minimum and maximum nominal frequencies of the DMA had to be disregarded, as explained in Section 4.1.2.

4.2 DISCUSSION OF MODEL RESULTS

In this section, it is discussed the proposed storage modulus model, the findings related to GPZ/GPBZ dissolution, secondary precipitation, the kinetic parameters of these transformations, the behaviour of the model coefficients, and finally the existence of a transition frequency marking the advent of fatigue.

4.2.1 Storage modulus

The storage modulus model proposed in Eq. 7 fits the experimental data in the prescribed temperature range (RT to around 300 ºC). In particular, the change of slope at 150–190 ºC, the inflexion around 200–250 ºC and local maximum around 280–330 ºC are properly accounted for. Also, the model allows the characterization of the contribution of GPZ/GPBZ dissolution and η' and θ'/S' phase formation to the storage modulus. Slight deviations observed in the vicinity of the upper limit of the valid temperature interval (i.e. close to the storage modulus maximum) are likely due to the onset of secondary precipitates dissolution and/or η, θ and S phase formation, which are not represented in the model.

In Fig. 36 the storage modulus behaviour with temperature is presented schematically for three different frequencies. This figure shows that the different contributions with frequency of the second and fourth terms on the right hand side of Eq. 7 (i.e. those associated to the linear decrease of storage modulus with temperature and to the secondary precipitates, respectively) explain why the storage modulus local maxima are delayed in temperature as frequency increases, while the inflexions (local minima) are shifted towards lower temperatures as frequency increases[20].

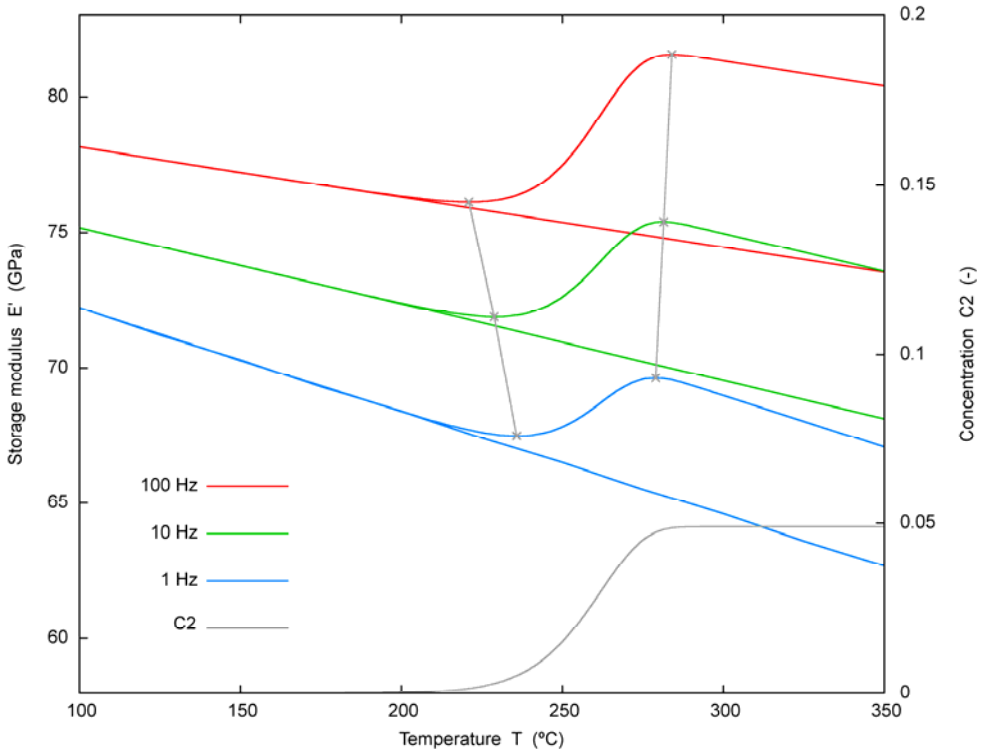

Fig. 36 Schematic representation of the storage modulus E' vs. temperature T based on the model proposed in Eq. 7 at a frequency of 100, 10 and 1 Hz, from 100 to 350 ºC. The concentration of secondary precipitates C_2 vs. temperature T is also plotted. The contribution of these precipitates to the storage modulus is responsible for the local minima and maxima.

[20] For simplicity, the contribution of the third term on the right hand side of Eq. 7 (i.e. that related to GPZ/GPBZ dissolution) has been deliberately omitted in this sketch, assuming that GPZ/GPBZ dissolution is completed around 200 ºC such that it does not affect the relative position of the local minima and maxima.

Moreover, linking the mechanical response to the kinetics of the accounted phase transformations allows us also to test the proposed models for the process of GPZ/GPBZ decomposition. To measure the overall goodness of the fit of the model to experimental data, and thus to assess the performance of each proposed reaction rate model, the error function described by Eq. 10 is used. In Table 25, an example of the values computed for the overall errors using this error function is presented.

Table 25 Overall errors for the fit of the model to experimental data for AA 7075-T6 and AA 2024-T3.

	Model used for GPZ/GPBZ dissolution rate		
Aluminium alloy	Jena (Eq. 8)	Pap. I (Eq. 2)	Pap. II (Eq. 3)
AA 7075-T6	1.30×10^{-6}	1.75×10^{-6}	1.33×10^{-6}
AA 2024-T3	3.81×10^{-6}	3.83×10^{-6}	3.84×10^{-6}

The description of GPZ/GPBZ decomposition with Jena's reaction rate, Eq. 8, leads to the overall best fit for AA 7075-T6, followed closely by the fit obtained when using Eq. 3. The overall best fit for AA 2024-T3 is also obtained when using Jena's reaction rate, Eq. 8, but in this case the goodness of the fit is practically identical for the three models considered. Summarizing, Eq. 8 and 3 are fitting the data well enough and there is no reason to consider one model better than the other. This is expected, as both stem formally from the same basis (i.e. JMAK kinetics with 3D diffusion), so they are physically the same. That is why the error between them (probably due to different sensitivity of the models to the test data) is minimal. The DMA results are then confirming this physical description of the GPZ dissolution process. Thus, the expected value of the activation energy can be taken as the average of those obtained by using Eq. 8 and 3: 1.14±0.11 eV/atom for AA 7075-T6 and 1.07±0.15 eV/Atom for AA 2024-T3. Also, as expected, due to the existence of two parallel ageing paths for AA 2024-T3, and the fact that the model is unable to cope with this increased complexity and to account separately for the effect of each path, the goodness of the fit is smaller for this alloy.

4.2.2 Concentration curves for GPZ/GPBZ dissolution & secondary precipitation

The concentration curves for GPZ/GPBZ dissolution and secondary precipitation exhibit a characteristic sigmoidal shape in agreement with results in the literature [9], indicating that the latter may be nucleation and growth transformations. This result is particularly expected for the case of η' and θ'/S' phase formation, as it is typical of the Avrami equation used to model these transformations. Tables 26 and 27 summarize the characteristic temperatures for the phase transformations accounted for by the model, as found in the literature (see Tables 6 and 9), and as derived from the experimental and model results (see Sections 2.2, 2.3, 3.4 and 3.5).

Table 26 Characteristic temperatures for transformations accounted for by the model for AA 7075-T6.

Transformation	Literature (DSC scans)	DMA test results	Model results
GPZ dissolution	From 100 to 219 ºC	Centred in 150–190 ºC	From 120 to 230 ºC
η' formation	From 100 to 306 ºC	From 220 to 330 ºC	From 150 to above 330 ºC

Table 27 Characteristic temperatures for transformations accounted for by the model for AA 2024-T3.

Transformation	Literature (DSC scans)	DMA test results	Model results
GPZ/GPBZ dissolution	From 100 to 297 ºC	Centred in 150–190 ºC	From 100 to 200 ºC
θ' formation	From 200 to 313 ºC	From 200 to 300 ºC	From 210 to 280 ºC
S' formation	From 120 to 350 ºC	From 200 to 300 ºC	From 210 to 280 ºC

The dissolution of the intermediate S' phase [9] and the stable η and θ phases [84] is dominated by temperature dependent thermodynamic equilibrium between these phases and the matrix. As a consequence, kinetic factors might not be important and these reactions occur always at the same temperature (i.e. peaks hardly shift in DSC scans) regardless of variations in the heating rate.

In contrast, most of the precipitation and dissolution processes involving metastable phases for AlZnMg and AlCuMg (e.g. GPZ/GPBZ dissolution and η' and θ'/S' phase formation), and also the formation of η and θ phase, are kinetically controlled. The formation rates of these transformations are limited by the reaction kinetics and thus the characteristic temperatures (e.g. peak and end temperature in DSC scans), increase with increasing heating rate, i.e. when sufficient time is not allowed for the reaction [9, 84, 96, 98]. The heating rates of 1 ºC/min used in the DMA tests[10] are low in comparison with typical heating rates used in DSC scans (commonly higher than 5 ºC/min). This is the reason why the characteristic temperatures derived from the DMA tests and model results for the transformations kinetically controlled may be shifted towards lower temperatures, compared to those reported in the literature from DSC data.

Bearing this in mind, it can be concluded that there is a good agreement between the results summarized in Tables 26 and 27. Accordingly, the variation of the storage modulus slope observed for both alloys at 150–190 ºC, which is unexplained until now, is ascribed to GPZ/GPBZ dissolution, and it indicates that the storage modulus grows with GPZ/GPBZ content. For AA 7075-T6, this is in agreement with Macchi [70], who pointed out that the mechanical response of AlZnMg alloys below 220 ºC is controlled by GPZ decomposition. Furthermore, we ascribe the storage modulus inflexion at 200–250 ºC and local maximum at 280–330 ºC to the continuation[21] and completion of η' phase precipitation for AA 7075-T6, and to the beginning and completion of θ'/S' phase precipitation for AA 2024-T3. To the author's knowledge, there is no other proposed explanation for these variations. Finally, the decrease in storage modulus after the local maximum may be due to η' (θ'/S') phase dissolution because these phenomena occur roughly in the same temperature range, i.e. above 300 ºC.

4.2.3 Kinetic parameters for GPZ/GPBZ dissolution & secondary precipitation

As regards to GPZ/GPBZ dissolution kinetics for both AA 7075-T6 and AA 2024-T3, the fitted values of the pre-exponential coefficient and the activation energy are coherent with the values reported in the literature [1, 9, 73, 82, 84, 96] (a comparison of activation energies is shown in Fig. 37 and 38).

[21] The term "continuation" is preferred to "beginning" because some η' precipitates are likely to be already present in AA 7075-T6 at RT.

Nevertheless, the activation energy seems to be technique-sensitive, as the reported values fall in a broad range (0.78–1.40 eV/atom for AA 7075, and 0.82–1.66 eV/atom for AA 2024). Another explanation for this dispersion may be that kinetics of dissolution processes depend on the precipitate shape, its formation mechanism and the concentration of solute [139, 140], and the latter parameter may change from a research work to another if different alloys than AA 7075 and AA 2024 were studied. Papazian [84] affirms that the activation energy for Cu GPZ dissolution should be close to that for chemical inter-diffusion in the AlCu systems, which is around 1.24–1.47 eV/atom [84, 141]. While the values obtained for AA 2024-T3 using Papazian's rate expressions, Eq. 2 and 3, are not far from this range, the activation energy obtained when using Jena's rate equation, Eq. 8, is the closest, and it is also the closest to the average of the values found in the literature. In any case it is reasonable to believe that diffusion of Cu in Al plays a key role in GPZ/GPBZ dissolution for AlCuMg alloys.

For AA 7075-T6, again the activation energy obtained when using Jena's rate equation, Eq. 8, is the closest to the average of the values found in the literature. It is noted also that the activation energy of Zn/Mg GPZ dissolution is close to that for migration of Mg and Zn in Al, i.e. around 1.14–1.35 and 1.22 eV/atom, respectively [141]. Diffusion of these species in Al may play a key role in GPZ dissolution for AlZnMg alloys. Summarizing, the models proposed by Papazian apparently lead to a slight underestimation of the activation energy for both AA 7075-T6 and AA 2024-T3. Hence, from this standpoint, the reaction rate proposed by Jena, Eq. 8, is the most appropriate to model GPZ/GPBZ dissolution.

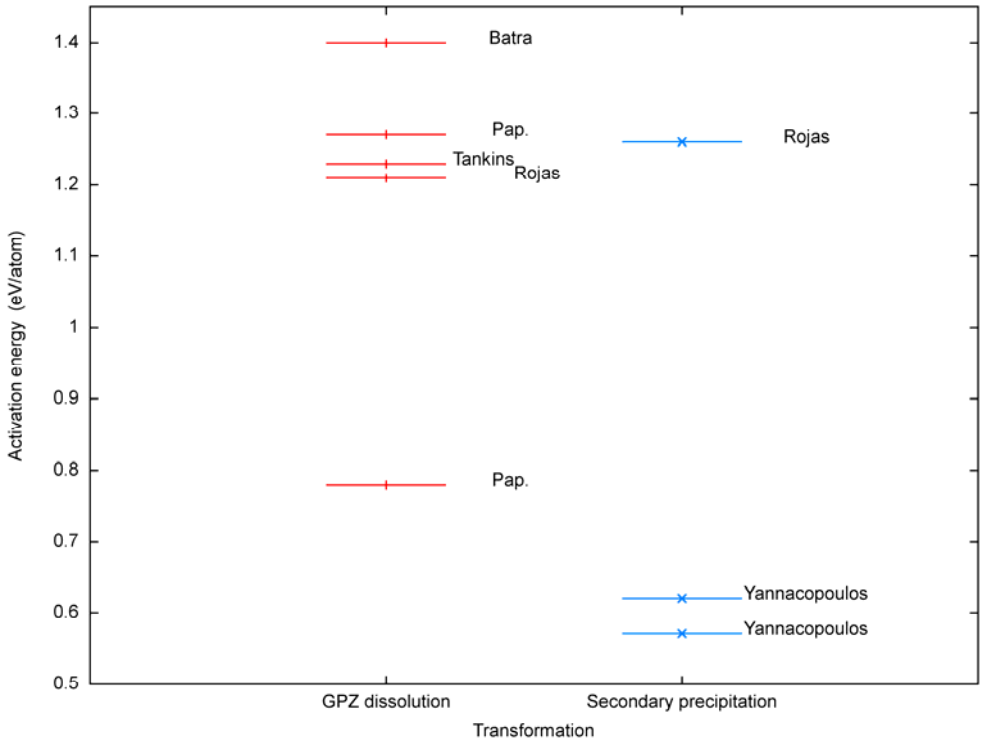

Fig. 37 Comparison of the activation energy E_A computed in this work (using Eq. 8 for GPZ dissolution) and those in the literature for GPZ dissolution and secondary precipitation for AA 7075-T6.

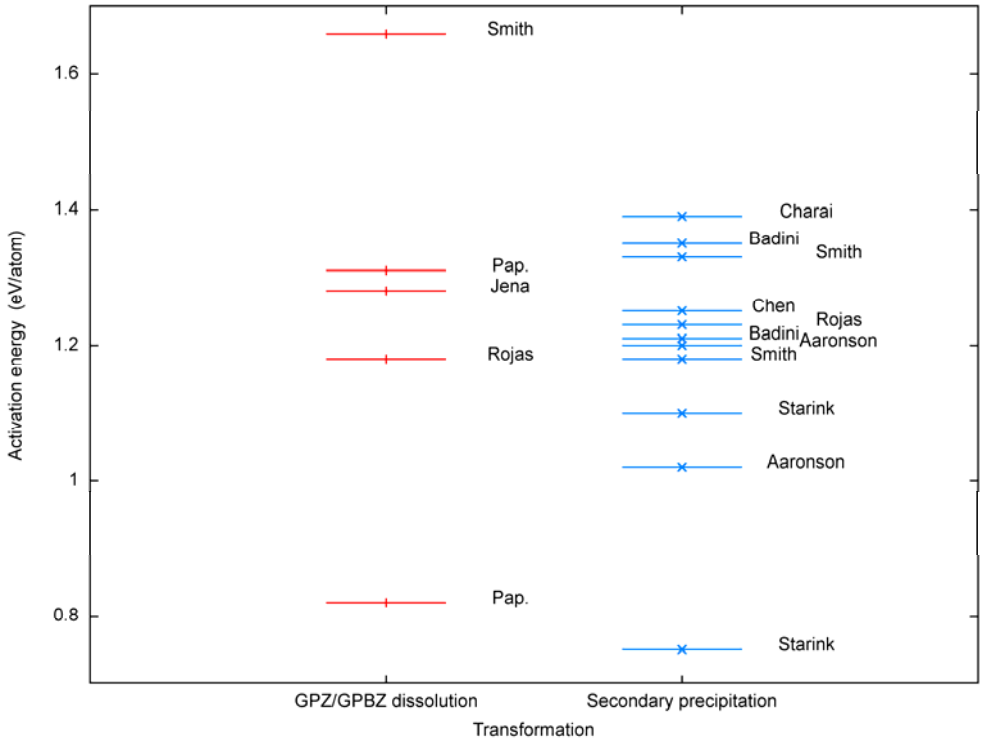

Fig. 38 Comparison of the activation energy E_A computed in this work (using Eq. 8 for GPZ dissolution) and those in the literature for GPZ/GPBZ dissolution and secondary precipitation for AA 2024-T3.

As per the kinetics of η' phase precipitation, there is a noticeable disagreement between the activation energy and Avrami index obtained in this work and those reported by Yannacopoulos [86] (see Table 11). This author obtained activation energies of 0.57-0.62 eV/atom and Avrami exponents of 2.3–2.8 (±20%), while we obtained 1.26 eV/atom and 0.76-0.84, respectively. Avrami exponents around 2.5 correspond to a 3D diffusion controlled transformation with continuous nucleation. The transformation being controlled by diffusion is consistent with the fact that long-range Mg and Zn migration is necessary for it to occur, but a continuous nucleation throughout the transformation seems not feasible in this case given that:

- In tests at constant heating rate, constant nucleation rates generally do not occur [119].
- Precipitation of η' phase occurs via nucleation from, or at, sites of GPZ [16, 70, 93], and these nuclei are already abundant in AA 7075-T6 at RT [96].

Therefore, site saturated nucleation is more probable, as it occurs for other alloys [119]. In turn, Avrami indexes equal to or slightly smaller than 1 (like those that we obtained) are typical of site saturated 2D diffusion controlled precipitation, which agrees with what was mentioned above and also with the plate shape reported for η' particles [69, 88]. As regards to the discrepancy in the activation energy values, as η' phase formation may be limited by the rate of migration of Mg and Zn in Al, it is expected that its activation energy be close to that for diffusion of these species in Al, and the value we obtained is much closer. In addition, the activation energy for η' phase formation should be higher than that for GPZ dissolution, because the former reaction necessarily occurs at higher temperatures, and the value calculated by Yannacopoulos is lower. Consequently, the results that we obtained for the activation

energy and Avrami index of η' phase formation are more consistent than those reported by Yannacopoulos.

As regards to θ'/S' phase precipitation, there is a good agreement between the activation energies computed from the proposed model and those available in the literature [73, 75, 84, 98, 125, 126] (see Table 12). Nevertheless, as in previous cases, there is a large dispersion in the latter values. Starink [98] presented several explanations for the dispersion in measured activation energies for θ' formation:

- Differences in the direction of growth or thickening and lengthening kinetics, e.g. for lengthening the activation energy is lower.
- Mobility of dissolved atoms, related to excess vacancy concentration: Cu diffusion proceeds only via a vacancy mechanism, and the activation energy is lower than that for Cu diffusion in Al and self-diffusion in Al. This indicates presence of large amounts of excess vacancies. In any case, vacancy–solute interactions are critical to many solute aggregation processes [70].
- Interfacial energy: The interfacial energy increases the activation energy obtained from Arrhenius analyses, and this effect grows with decreasing temperature, such that activation energies obtained at lower temperatures are higher.

Starink [98] observed also that, in general, activation energies for θ' formation were lower than that for Cu diffusion in Al and self-diffusion in Al, which is the case for our results. Finally, on the one side, the computed pre-exponential coefficients are larger than those in the literature by approximately an order of magnitude. The reason for this discrepancy is unknown. On the other side, the computed Avrami indexes are slightly larger than those in the literature [9, 84] (see Table 12), but falling in the same range, i.e. 1.0 to 1.5, which is commonly associated to site saturated 2D or 3D diffusion controlled transformations. This is coherent with θ'/S' phase precipitation because, for instance:

- In tests at constant heating rate, constant nucleation rates generally do not occur [119].
- The θ' phase nucleates at dislocations [112] or on the faces of GPZ II [72], and the S' phase nucleates homogeneously at GPBZ, and heterogeneously on dislocations [77]. Therefore, site saturated nucleation is again more probable, as it occurs for other alloys [119], given that numerous nuclei (i.e. GPZ/GPBZ and dislocations) are already abundant in AA 2024-T3 at RT.
- The θ' precipitates are plate-shaped [84, 98].
- The growth kinetics of θ' precipitates [99] and S' precipitates [9] are controlled by diffusion.

4.2.4 Storage modulus model coefficients

Regarding the model coefficients, it is observed that the coefficient E'_{RT} (the storage modulus at RT) is very similar for all the studied frequencies and that it is very close to the elastic modulus of pure Al. Namely, the averaged values are 72.22±1.79 GPa for AA 7075-T6 and 76.37±2.37 GPa for AA 2024-T3. Thus, as expected, varying the excitation frequency has no significant effect on E'_{RT}, since the

viscoelastic response (and particularly, the storage modulus) dependence on frequency weakens as temperature decreases. On the contrary, the coefficient E'_0 (the rate of storage modulus loss with temperature) increases significantly with frequency (i.e. becomes less negative) for both alloys and pure Al. This is coherent with the expected lower decrease of the storage modulus with temperature at high frequencies compared to low frequencies. The values that we obtained for E'_0 are smaller than that reported by Wolfenden (-80 MPa·°C^{-1}) for pure Al at 80 kHz [55], but are very similar if we take into account only Wolfenden's data from RT to 130 ºC.

Some information on the error in the determination of E'_0 might stem from the results for pure Al. In this case, the error between the model coefficient and the slope of the experimental storage modulus with temperature is about 2.2% in average. The error is probably due to slight differences in the evaluated temperature intervals. For the alloys, probably new sources of error in the determination of E'_0 arise, like interferences due to GPZ/GPBZ dissolution, which may begin well below 150 ºC.

The coefficient E'_1 (accounting for the contribution of GPZ/GPBZ) has a different behaviour in the two alloys analysed. Results for AA 2024-T3 show a slightly larger dispersion compared to AA 7075-T6, for the considered reaction rates. This fact may be related to the higher complexity of the precipitation paths of AA 2024-T3 and to the different kinetics observed in the alloys. That is, the pre-exponential coefficient for GPZ dissolution and the Avrami index for secondary precipitation in AA 7075-T6 are smaller than those for AA 2024-T3, indicating that for the former alloy these processes are slower. This allows a much better determination of the coefficients E'_1 and E'_2 (accounting for the contribution of secondary phases during precipitation) for AA 7075-T6. Summarizing, the behaviour of both coefficients is more consistent for AA 7075-T6. For this alloy, E'_1 shows a slight decrease with frequency, while E'_2 increases noticeably with frequency.

Conversely, for AA 2024-T3, E'_1 shows a slight increase with frequency, while again E'_2 increases noticeably with frequency. If the different behaviour of E'_1 for AA 2024-T3 compared to AA 7075-T6 is not due to the increased uncertainty for the reasons explained above, the only explanation we can suggest for this phenomenon is that the tested frequencies excite regions of a size that falls between the characteristic diameters of GPZ for AA 7075-T6 (around 6 nm) and GPZ/GPBZ for AA 2024-T3 (around 25 nm) (see Tables 5 and 8). Thus, with increasing frequency, the smaller GPZ in AA 7075-T6 are increasingly excited and their contribution to the storage modulus decreases, while the contrary occurs for AA 2024-T3. This is an argument of plausibility because we have not been able to find any reference that establishes a correlation between excitation frequency and particle size beyond general comments.

The increase in E'_2 observed in both alloys is consistent with the behaviour of the loss modulus and loss tangent (see Sections 2.2.2 and 2.2.3), showing that dissipation effects decrease as frequency increases in the temperature range corresponding to secondary precipitation.

Nonetheless, the dispersion in the model coefficients for AA 2024-T3 does not affect the values of the fitted kinetic parameters, though it appears that they are average values corresponding to the two

simultaneous dissolution processes (i.e. GPZ and GPBZ dissolution) ant the two subsequent precipitation processes (i.e. θ' and S' formation), respectively, for the two parallel ageing sequences of this AlCuMg alloy. Unfortunately, the accuracy of the experimental data does not allow us to fit a more detailed redissolution/precipitation kinetic model for AA 2024-T3. Finally, it is observed that for both alloys the values of the coefficient E'_2 are higher than those of E'_1, which means that secondary precipitates have a more important effect on stiffness per unit concentration than GPZ/GPBZ.

Finally, it is worth recalling that the calculation of the storage modulus model coefficients and kinetic parameters is based on the integration of the rate equations for GPZ/GPBZ dissolution and secondary precipitation, performed inside the least-squares non-linear fitting of the storage modulus model to experimental data. A problem inherent of this solving process is that occasionally the solution may correspond to a local minimum of the least-squares function, rather than to the absolute minimum. This means that it may be possible to find a set of fitting parameters giving a better fit than that supplied by the solver, such that more accurate values of the model coefficients and kinetic parameters would be obtained, but the solver is unable to find that solution as it stopped and it is stuck in the local minimum. This depends on the initial values provided to the solver, and it may explain also some of the differences between the obtained results for the kinetic parameters and those in the literature.

4.2.5 Transition frequency

Recalling Amiri's work [20], we may assume that it is necessary some degree of hysteresis heating (caused by energy dissipated due to internal friction phenomena) for metals to experience fatigue when subjected to dynamic loading. With excitation frequency tending to zero, the test time scale may become large enough such that it is far from the largest time scale for any of the possible relaxation processes for the particular material. That is, at sufficiently low frequency there may be virtually no phase lag between stress and strain, and the frictional energy loss and hysteresis heating due to relaxation effects are minimal. Thus, it is reasonable to presume that, below a given threshold frequency, the material would practically exhibit a static-like, elastic response (relaxed case), such that creep mechanisms would dominate and fatigue problems would be negligible. This hypothesis would be in line also with research by Henaff [40] and Nikbin [39], suggesting the existence of a critical value of the loading frequency below which, for a given temperature, crack growth is sensitive to frequency and static creep dominates instead of pure fatigue mechanisms.

A procedure to estimate this transition frequency is proposed based on available data on the frequency dependence of the slope of the storage modulus linear decrease with temperature, E'_0. The procedure is illustrated in Fig. 39. The figure shows the coefficient E'_0, obtained from some of the simulations, plotted as a function of the excitation frequency for AA 7075-T6, AA 2024-T3 and pure Al, as well as the slopes computed for pure Al by linear regression of the DMA data. These data are compared to the average values of the rates of loss of static elastic modulus with temperature, obtained by linear regression of data in the literature for pure Al [52] and for AA 2024 [53], between RT and 400 ºC. To calculate this average,

Kamm's [132] and Varshni's data [133] were disregarded because they correspond to temperatures below RT, and Wolfenden's data [55] because they are quite scattered in a broad temperature range, and thus the slope is not representative.

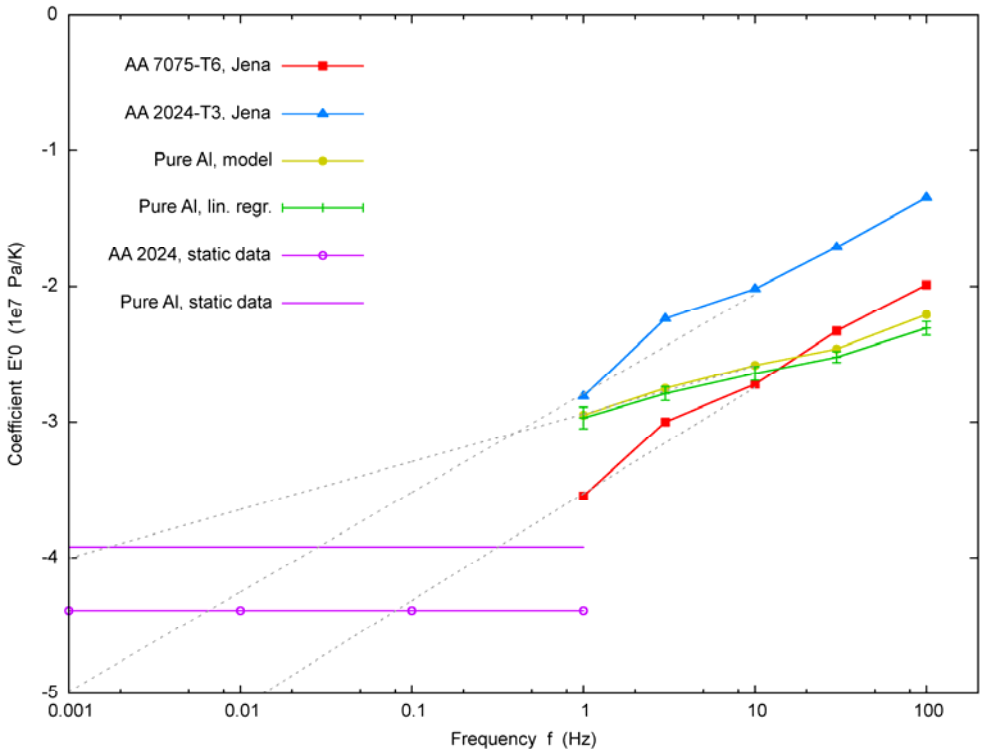

Fig. 39 Coefficient E'_0 of the storage modulus model vs. frequency f for AA 7075-T6, AA 2024-T3 and pure Al, slopes computed for pure Al by linear regression of DMA data from RT to 100 ºC, and average values of the rates of loss of static elastic modulus with temperature, obtained by linear regression of data in the literature for pure Al [52] and for AA 2024 [53]. The dashed lines are logarithmic tendency lines fitted to the data series.

Assuming that at the transition frequency the coefficient E'_0 would equal the rate of loss of static elastic modulus with temperature, this threshold frequency may be estimated by intersection of the latter value with a logarithmic tendency line extrapolating the behaviour of the coefficient E'_0 to lower frequencies. In the example shown in Fig 35, the intersection of the logarithmic tendency line with the static data slope for pure Al gives a transition frequency of approximately 0.002 Hz. For AA 2024-T3, the transition frequency is about 0.007 Hz. For AA 7075-T6, no data on the variation of the elastic stiffness constants with temperature has been found in the literature, but using the data available for pure Al and AA 2024, a transition frequency between 0.3 and 0.08 Hz is obtained. These results are similar to those in the literature: Henaff [40] reported a critical frequency of 0.02 Hz for AA 2650-T6, and Nikbin [39] reported that the transition region is 0.1 to 1.0 Hz for cast aluminium alloy RR58 at 150 ºC. However, to better assess the performance of the proposed procedure, comparison with experimental data on fatigue response at very low frequencies is necessary, and generally there is lack of this type of data [40]. Finally, it is interesting to note that, according to this analysis, for pure Al fatigue problems appear already at lower excitation frequencies, compared to the alloys. This shows that the precipitation structure in the

alloys not only causes hardening but also enables for the alloys to be loaded at a wider range of low frequencies without experiencing fatigue.

The proposed procedure for the determination of the threshold frequency is a major result of this work. Low frequency fatigue experiments are, by definition, very long. Furthermore, there is a deep controversy about the environmental effects, as it is impossible to perform longstanding experiments in constant conditions. Besides, when considering service conditions the environment may be different than that for the performed experiment and the predictions based on test experiments may be thus inaccurate. The determination of the threshold frequency through DMA tests reflects intrinsic properties of the material only. It offers also a standardized method, which allows precise comparison between different alloys. Furthermore, it is quite insensitive to the specific instrumental range available for the tests, provided it is large enough to allow a consistent regression fit.

5 CONCLUSIONS

The viscoelastic responses of AA 7075-T6, AA 2024-T3 and pure Al depend on temperature, the excitation frequency and the microstructure/phase transformations (when present). The responses of the alloys are qualitatively very similar. The decrease of the storage modulus with temperature, observed in the studied materials as early as at RT and assumed to be linear, is explained by the dependence of the elastic stiffness constants on temperature. The Arrhenius-type behaviour of the relaxation rate, causing a reduction of the relaxation time as temperature increases, explains the following behaviours:

- The viscoelastic behaviour depends more significantly on frequency as temperature increases.
- The materials seem stiffer (i.e. the storage modulus is higher) as frequency increases.
- Some phenomena are delayed in temperature as frequency increases, for example:
    - The storage modulus local maximum due to secondary precipitation.
    - The beginning of the ramp increase in internal friction.
- The internal friction ramp slope decreases as frequency increases.
- At high temperatures (above 150 ºC) the materials have less energy losses (i.e. the internal friction is lower) as frequency increases.
- The internal friction peaks shift progressively towards lower frequencies and become broader (e.g. due to a wider distribution of relaxation times) with decreasing temperature.

In the isothermal curves of storage modulus vs. frequency, the minimum values appear for frequencies tending to zero (relaxed case), while the maximum values appear at very high frequencies (unrelaxed case). Instrument limitations do not allow us to conclude whether their shape is sigmoidal or a combination of sigmoidals. In addition, the results obtained on the internal friction peaks (i.e. the relaxation spectrum) correspond to a very narrow frequency range, which does not allow for a proper characterization of the peaks. The microstructure and therefore the viscoelastic properties are not stabilized. Thus, the observed peaks may be caused also by transient effects or the modification of the microstructure during the tests. Due to all these reasons, it is not possible to determine the exact number and type of relaxations taking place, or to obtain useful information about these processes, like their characteristic relaxation times and activation energies. However, it has been established that:

- For AA 7075-T6, the internal friction may be due to relaxations associated to:
    - Atom groupings within GPZ.
    - Grain boundaries.
    - Discontinuous precipitation.
    - Secondary phases.
- For AA 2024-T3, the internal friction may be due to relaxations associated to:
    - Atom groupings within GPZ/GPBZ.
    - Grain boundaries.

    - θ′ phase.
    - θ phase.
- For pure Al, the internal friction may be due to relaxations associated to:
    - Grain boundaries.

For the alloys, the internal friction is low and constant at low temperatures, and exhibits a ramp increase starting at 150-200 ºC, which indicates that more energy is dissipated through viscoelastic processes. The increase is attributed to the onset of relaxations associated to secondary phases (as it starts roughly when secondary precipitation begins) and to grain boundaries. The latter is deduced by comparison with the internal friction behaviour of pure Al, showing a peak at 300 ºC related to grain boundary migration.

Another important outcome of this work is that the decrease of yield and fatigue behaviour observed in aluminium alloys as temperature increases may be due to the internal friction increase. If it is assumed that internal friction variations with loading frequency may also modify the fatigue response, our results suggest that below 150 ºC the yield and fatigue strength will diminish with increasing frequency, while at high temperatures these properties will increase.

The TTS principle has been successfully applied to the measured data, providing master curves for the storage modulus at low temperatures, and for the storage and loss moduli at high temperatures, and enabling extrapolation of the viscoelastic behaviour to any frequency and temperature within the region of validity. The existence of separated master curves for low temperatures and high temperatures is due to the occurrence of microstructural changes in between and variations in the relaxation mechanisms. It is worth to mention that the master curves appear only in the temperature ranges where the microstructure is stable, as confirmed in the modelling of the storage modulus. To the author's knowledge, the TTS principle has not been applied to crystalline materials until now.

A model of the storage modulus evolution is proposed that fits the test data in the prescribed temperature range (RT to 300 ºC). Beyond the qualitative description, the proposed model allowed us to relate the microstructural transformations to the viscoelastic properties of the alloys. In particular, the observed variation in the storage modulus slope at 150–190 ºC is ascribed to GPZ/GPBZ dissolution, while the storage modulus inflexion at 200–250 ºC and local maximum at 280–300 ºC are ascribed to the continuation and completion of η' phase precipitation for AA 7075-T6, and θ'/S' phase precipitation for AA 2024-T3. The decrease in storage modulus after the local maximum may be due to η' (θ'/S') dissolution. Also, some models proposed for GPZ/GPBZ decomposition rate were tested. The best overall fit of the storage modulus model to experimental data and the most accurate activation energies for this transformation are obtained when using Jena's rate equation, Eq. 8. Thus, under these criteria it is concluded that this Arrhenius-type expression describes best the GPZ/GPBZ dissolution process.

The general agreement of the kinetic parameters obtained from the proposed storage modulus model with data available in the literature confirms the validity of the approximation. It confirms also that a combined DSC and DMA analysis is an adequate tool for studying the material microstructure, the

kinetics of phase transformations and the influence of these transformations on the viscoelastic properties of materials (e.g. it is possible to identify the transformations responsible for the maximum damping). It is worth to note that, contrary to DSC analysis, the dynamic-mechanical response is independent of the total enthalpy change of the transformation, thus allowing the analysis of microstructural transformations involving minority phases.

From the observation of the storage modulus model coefficients the following conclusions are derived:

- The storage modulus at RT, E'_{RT}, is not affected by the excitation frequency.
- The rate of storage modulus loss with temperature, E'_0, increases significantly with frequency.
- The coefficient E'_1 shows a different trend with frequency in each alloy. A plausible explanation for this phenomenon is suggested.
- Secondary precipitates have a more important effect on stiffness per unit concentration than GPZ/GPBZ.
- The contribution of secondary precipitates is consistent with the internal friction decrease as frequency increases in the corresponding temperature range.

Finally, it is suggested that some degree of internal friction is necessary for metals to experience fatigue when subjected to dynamic loading, and that, below a given threshold frequency, as the frictional energy loss and hysteresis heating due to relaxation effects are minimal, the material may exhibit a static-like, elastic response, such that creep mechanisms dominate and fatigue problems are negligible. A procedure to estimate this transition frequency is proposed. For pure Al, AA 2024-T3 and AA 7075-T6 the transition frequencies are approximately 0.002, 0.007 and 0.3–0.08 Hz, respectively. According to this analysis, fatigue problems may appear already at lower excitation frequencies for pure Al. Thus, the precipitation structure in the alloys enables for the alloys to be loaded at a wider range of low frequencies without experiencing fatigue. However, to better assess the performance of the proposed procedure, comparison with experimental data on fatigue response at very low frequencies is necessary.

The proposed procedure for the determination of the transition frequency is a major result of this work, as it is environment- and instrument-independent, and requires short-time testing. Consequently, this technique is able to determine the intrinsic threshold frequency of the studied material and allows precise comparison between different alloys.

5.1 ASSESSMENT OF THE OBJECTIVES OF THIS RESEARCH

The first objective of this work has been accomplished, as the effects of temperature, excitation frequency and phase transformations (when present) on the viscoelastic behaviour of AA 7075-T6, AA 2024-T3 and pure Al have been identified and characterized in the temperature range RT–300 ºC. Also, a model has been proposed for the storage modulus in this temperature range, which accounts for the effects of temperature, the frequency and phase transformations involving GPZ/GPBZ and semi-coherent

precipitates. Incoherent precipitates are not accounted for, which is particularly valid for AA 2024-T3 as they form at temperatures higher than 300 ºC, but not so reasonable for AA 7075-T6, as they may form at slightly lower temperatures.

The individual identification and characterization of the mechanical relaxation processes causing the measured internal friction has not been accomplished for the alloys, due to the experimental limitations which do not allow for a reliable univocal correlation of the observed phenomena to the relaxation effects in the literature. Rather, it has only been possible to suggest some relaxation mechanisms that might be present, according to their characteristics as reported in the literature. For the same reason, it has not been possible to develop a model for the loss modulus behaviour, and yet we are unable to explain some of the effects of temperature, frequency and phase transformations on the internal friction.

The second objective of this work has been accomplished partially. Indeed, it was a very ambitious target, and it is probably impossible to fulfil it in a single PhD. Here, a relationship between the fatigue response and the internal friction behaviour with temperature and frequency was suggested. However, a new procedure able to determinate the transition frequency is proposed. Below the transition frequency, materials subjected to dynamic loading exhibit a static-like behaviour, and such fatigue problems may be negligible. This result was not included in the initial goals of this work, and it is then considered a major contribution to the understanding of fatigue behaviour.

5.2 FUTURE WORK

The work reported in this PhD opens several questions that may be continued in the future, like research on new issues that arose during this work or from the reported findings, or the continuation of research that was not completed because of falling too far from the scope that we initially established:

1. Refine the proposed storage modulus model, Eq. 7:
    a. Better description of the viscoelastic behaviour over a wider range of temperatures, e.g. enhance the model such that it accounts for the effects of phase transformations:
        i. At lower temperatures, like GPZ/GPBZ formation, if their precipitation process is not complete prior to testing.
        ii. At higher temperatures, like dissolution of η’ and θ’/S’ phases and formation of η and θ/S phase.
    b. Discrimination of the individual contributions of GPZ, GPBZ, θ’ and S’ phases, from the precipitation paths evolving in parallel for AA 2024.
2. Test more reaction rate models for secondary phase formation, aside from the Avrami equation.
3. TEM/HRTEM studies to measure the temperature evolution of the concentration of precipitates.
4. DMA tests on AA 7075 and AA 2024 with treatments different from the T6 and T3 tempers. The goal would be to identify differences in the viscoelastic behaviour due to the alloy temper, and see how this links with the corresponding microstructure.

5. DMA tests below RT to check, for example, whether the loss modulus peak suggested in Section 4.1.2 exists or not. Only possible after upgrading the DMA.
6. DMA tests at temperatures higher than 375 ºC, to allow the extension of the proposed model.
7. Measure the viscoelastic response of the alloys below and above the DMA operational limits:
    a. To better characterize the peaks in the frequency domain.
    b. To obtain the viscoelastic spectra from experimental response functions, such that information is obtained on the relaxations responsible for the viscoelastic response.
    c. To further investigate the existence of the suggested transition frequency.
8. Develop an analytical model correlating fatigue behaviour to viscoelastic response of the alloys.

REFERENCES

[1] Nowick, A.S., and Berry, B.S., "Anelastic relaxation in crystalline solids," Academic Press, New York; London, 1972, pp. 677.

[2] Rao, M.D., "Recent applications of viscoelastic damping for noise control in automobiles and commercial airplanes," Journal of Sound and Vibration, Vol. 262, No. 3, 2003, pp. 457-474.

[3] Srivatsan, T.S., Kolar, D., and Magnusen, P., "Influence of temperature on cyclic stress response, strain resistance, and fracture behavior of aluminum alloy 2524," Materials Science and Engineering A-Structural Materials Properties Microstructure and Processing, Vol. 314, No. 1-2, 2001, pp. 118-130.

[4] Chung, T.E., and Faulkner, R.G., "Parametric Representation of Fatigue in Alloys and its Relation to Microstructure," Materials Science and Technology, Vol. 6, No. 12, 1990, pp. 1187-1192.

[5] Karaaslan, A., Kaya, I., and Atapek, H., "Tensile strength and impact toughness of an AA 7075-T6 alloy," Mp Materials Testing-Materials and Components Technology and Application, Vol. 50, No. 5, 2008, pp. 256-258.

[6] Soifer, Y.M., Kobelev, N.P., Brodova, L.G., "Internal friction and the Young's modulus change associated with amorphous to nanocrystalline phase transition in Mg-Ni-Y alloy," Nanostructured Materials, Vol. 12, No. 5-8, 1999, pp. 875-878.

[7] Zink, M., Samwer, K., Johnson, W.L., "Validity of temperature and time equivalence in metallic glasses during shear deformation," Physical Review B, Vol. 74, No. 1, 2006, pp. 012201.

[8] Abis, S., Massazza, M., Mengucci, P., "Early ageing mechanisms in a high-copper AlCuMg alloy," Scripta Materialia, Vol. 45, No. 6, 2001, pp. 685-691.

[9] Jena, A.K., Gupta, A.K., and Chatuverdi, M.C., "A differential scanning calorimetric investigation of precipitation kinetics in the Al-1.53 wt% Cu-0.79 wt% Mg alloy," Acta Metallurgica Et Materialia, Vol. 37, No. 3, 1989, pp. 885-895.

[10] Bierwagen, G., "Next generation of aircraft coatings systems," Journal of Coatings Technology, Vol. 73, No. 915, 2001, pp. 45-52.

[11] Vreugdenhil, A.J., Balbyshev, V.N., and Donley, M.S., "Nanostructured silicon sol-gel surface treatments for Al 2024-T3 protection," Journal of Coatings Technology, Vol. 73, No. 915, 2001, pp. 35-43.

[12] Chlistovsky, R.M., Heffernan, P.J., and DuQuesnay, D.L., "Corrosion-fatigue behaviour of 7075-T651 aluminum alloy subjected to periodic overloads," International Journal of Fatigue, Vol. 29, No. 9-11, 2007, pp. 1941-1949.

[13] Starke, E.A., and Staley, J.T., "Application of modern aluminum alloys to aircraft," Progress in Aerospace Sciences, Vol. 32, No. 2-3, 1996, pp. 131-172.

[14] Tylecote, R.F., "A History of Metallurgy," The Metals Society, London, 1988, pp. 182.

[15] European Committee for Standardization (CEN), "UNE-EN 515: Aluminium and aluminium alloys. Wrought products. Temper designations," Asociación Española de Normalización y Certificación (AENOR), Madrid, Spain, 1993, pp. 23.

[16] Ferragut, R., Somoza, A., and Dupasquier, A., "On the two-step ageing of a commercial Al-Zn-Mg alloy; A study by positron lifetime spectroscopy," Journal of Physics-Condensed Matter, Vol. 8, No. 45, 1996, pp. 8945-8952.

[17] Loffler, H., Kovacs, I., and Lendvai, J., "Decomposition Processes in Al-Zn-mg Alloys," Journal of Materials Science, Vol. 18, No. 8, 1983, pp. 2215-2240.

[18] Callister, W.D., "Materials science and engineering: an introduction," John Wiley, New York etc., 1985, pp. 602.

[19] Van Kranenburg, C., "Fatigue crack growth in Aluminium Alloys," Technische Universiteit Delft, Delft, The Netherlands, 2010, pp. 194.

[20] Amiri, M., and Khonsari, M.M., "Life prediction of metals undergoing fatigue load based on temperature evolution," Materials Science and Engineering A-Structural Materials Properties Microstructure and Processing, Vol. 527, No. 6, 2010, pp. 1555-1559.

[21] Hong, Y., Zhao, A., and Qian, G., "Essential Characteristics and Influential Factors for Very-High-Cycle Fatigue Behavior of Metallic Materials," Acta Metallurgica Sinica, Vol. 45, No. 7, 2009, pp. 769-780.

[22] Braun, R., "Transgranular environment-induced cracking of 7050 aluminium alloy under cyclic loading conditions at low frequencies," International Journal of Fatigue, Vol. 30, No. 10-11, 2008, pp. 1827-1837.

[23] Nikitin, I., and Besel, M., "Effect of low-frequency on fatigue behaviour of austenitic steel AISI 304 at room temperature and 25 degrees C," International Journal of Fatigue, Vol. 30, No. 10-11, 2008, pp. 2044-2049.

[24] Zhu, X., Jones, J.W., and Allison, J.E., "Effect of frequency, environment, and temperature on fatigue behavior of E319 cast aluminum alloy: Stress-controlled fatigue life response," Metallurgical and Materials Transactions A-Physical Metallurgy and Materials Science, Vol. 39A, No. 11, 2008, pp. 2681-2688.

[25] Mayer, H., Papakyriacou, M., Pippan, R., "Influence of loading frequency on the high cycle fatigue properties of AlZnMgCu1.5 aluminium alloy," Materials Science and Engineering A-Structural Materials Properties Microstructure and Processing, Vol. 314, No. 1-2, 2001, pp. 48-54.

[26] Furuya, Y., Matsuoka, S., Abe, T., "Gigacycle fatigue properties for high-strength low-alloy steel at 100 Hz, 600 Hz, and 20 kHz," Scripta Materialia, Vol. 46, No. 2, 2002, pp. 157-162.

[27] Liaw, P.K., Wang, H., Jiang, L., "Thermographic detection of fatigue damage of pressure vessel steels at 1,000 Hz and 20 Hz," Scripta Materialia, Vol. 42, No. 4, 2000, pp. 389-395.

[28] Urabe, N., and Weertman, J., "Dislocation Mobility in Potassium and Iron Single-Crystals," Materials Science and Engineering, Vol. 18, No. 1, 1975, pp. 41-49.

[29] Murakami, Y., Nomoto, T., and Ueda, T., "Factors influencing the mechanism of superlong fatigue failure in steels," Fatigue & Fracture of Engineering Materials & Structures, Vol. 22, No. 7, 1999, pp. 581-590.

[30] Mayer, H., "Fatigue crack growth and threshold measurements at very high frequencies," International Materials Reviews, Vol. 44, No. 1, 1999, pp. 1-34.

[31] Laird, C., and Charsley, P., "Ultrasonic Fatigue," The Metallurgical Society of AIME, Philadelphia, USA, 1982,

[32] Papakyriacou, M., Mayer, H., Pypen, C., "Influence of loading frequency on high cycle fatigue properties of b.c.c. and h.c.p. metals," Materials Science and Engineering A-Structural Materials Properties Microstructure and Processing, Vol. 308, No. 1-2, 2001, pp. 143-152.

[33] Yan, N., Wang, Q.Y., Chen, Q., "Influence of loading frequency on fatigue behavior of high strength steel," Progresses in Fracture and Strength of Materials and Structures, 1-4, Vol. 353-358, 2007, pp. 227-230.

[34] Mayer, H., and Laird, C., "Influence of Cyclic Frequency on Strain Localization and Cyclic Deformation in Fatigue," Materials Science and Engineering A-Structural Materials Properties Microstructure and Processing, Vol. 187, No. 1, 1994, pp. 23-35.

[35] Yan, B., Hunsche, A., Neumann, P., "Loop Patch Behavior as Affected by Incremental Loading and Cyclic Frequency in Fatigue," Materials Science and Engineering, Vol. 79, No. 1, 1986, pp. 9-14.

[36] Verkin, B.I., and Grinberg, N.M., "Effect of Vacuum on the Fatigue Behavior of Metals and Alloys," Materials Science and Engineering, Vol. 41, No. 2, 1979, pp. 149-181.

[37] Menan, F., and Henaff, G., "Influence of frequency and waveform on corrosion fatigue crack propagation in the 2024-T351 aluminium alloy in the S-L orientation," Materials Science and Engineering A-Structural Materials Properties Microstructure and Processing, Vol. 519, No. 1-2, 2009, pp. 70-76.

[38] Benson, D.K., and Hancock, J.R., "Effect of Strain Rate on Cyclic Response of Metals," Metallurgical Transactions, Vol. 5, No. 8, 1974, pp. 1711-1715.

[39] Nikbin, K., and Radon, J., "Prediction of fatigue interaction from static creep and high frequency fatigue crack growth data," Advances in Fracture Research, vol. 1-6, 1997, pp. 429.

[40] Henaff, G., Odemer, G., Benoit, G., "Prediction of creep-fatigue crack growth rates in inert and active environments in an aluminium alloy," International Journal of Fatigue, Vol. 31, No. 11-12, 2009, pp. 1943-1951.

[41] Meyers, M.A., and Chawla, K.K., "Mechanical Behavior of Materials," Cambridge University Press, Cambridge, UK, 2009,

[42] Spaepen, F., "Physics of defects," Balian, R. Kleman, M. and Poirier, J.P. eds., North-Holland Pub. Co., Amsterdam, The Netherlands, 1981, pp. 857.

[43] Hopkins, I.L., and Kurkjian, C.R., "Physical acoustics: principles and methods," Mason, W.P. ed., Academic Press, New York, NY, USA, 1965,

[44] Angell, C.A., "Dynamic Processes in Ionic Glasses," Chemical Reviews, Vol. 90, No. 3, 1990, pp. 523-542.

[45] Suh, D.W., and Dauskardt, R.H., "Mechanical relaxation time scales in a Zr-Ti-Ni-Cu-Be bulk metallic glass," Journal of Materials Research, Vol. 17, No. 6, 2002, pp. 1254-1257.

[46] Villuendas, A., Roca, A., and Jorba, J., "Change of Young's modulus of cold-deformed aluminum AA1050 and of AA2024 (T65): A comparative study," THERMEC 2006, Pts 1-5; Materials Science Forum; 5th International Conference on Processing and Manufacturing of Advanced Materials, Vol. 539-543, Trans Tech Publications Ltd., Stafa-Zurich, Switzerland, 2007, pp. 293-298.

[47] Mack, D.J., "Young's Modulus - its Metallurgical Aspects," Transactions of the American Institute of Mining and Metallurgical Engineers, Vol. 166, 1946, pp. 68-84.

[48] Ledbetter, H.M., and Kim, S.A., "Low-Temperature Elastic-Constants of Deformed Polycrystalline Copper," Materials Science and Engineering A-Structural Materials Properties Microstructure and Processing, Vol. 101, 1988, pp. 87-92.

[49] Yamaguchi, K., Adachi, H., and Takakura, N., "Effects of plastic strain and strain path on Young's modulus of sheet metals," Metals and Materials-Korea, Vol. 4, No. 3, 1998, pp. 420-425.

[50] Benito, J.A., Manero, J.M., Jorba, J., "Change of Young's modulus of cold-deformed pure iron in a tensile test," Metallurgical and Materials Transactions A-Physical Metallurgy and Materials Science, Vol. 36A, No. 12, 2005, pp. 3317-3324.

[51] Morestin, F., and Boivin, M., "On the necessity of taking into account the variation in the Young modulus with plastic strain in elastic-plastic software," Nuclear Engineering and Design, Vol. 162, No. 1, 1996, pp. 107-116.

[52] Sutton, P.M., "The Variation of the Elastic Constants of Crystalline Aluminum with Temperature between 63°K and 773°K," Physical Review, Vol. 91, No. 4, 1953, pp. 816-821.

[53] Brammer, J.A., and Percival, C.M., "Elevated-Temperature Elastic Moduli of 2024-Aluminum obtained by a Laser-Pulse Technique," Experimental Mechanics, Vol. 10, No. 6, 1970, pp. 245-&.

[54] Das, T., Bandyopadhyay, S., and Blairs, S., "DSC and DMA Studies of Particulate-Reinforced Metal-Matrix Composites," Journal of Materials Science, Vol. 29, No. 21, 1994, pp. 5680-5688.

[55] Wolfenden, A., and Wolla, J.M., "Mechanical Damping and Dynamic Modulus Measurements in Alumina and Tungsten Fiber-Reinforced Aluminum Composites," Journal of Materials Science, Vol. 24, No. 9, 1989, pp. 3205-3212.

[56] Wolla, J.M., and Wolfenden, A., "Dynamic elastic modulus measurements in materials, ASTM STP 1045," Wolfenden, A. ed., ASTM, Philadelphia, USA, 1990.

[57] Dicarlo, J.A., and Maisel, J.E., "Composite Materials: Testing and Design (Fifth Conference), ASTM STP 674," ASTM, Philadelphia, USA, 1979.

[58] Li, J.F., Peng, Z.W., Li, C.X., "Mechanical properties, corrosion behaviors and microstructures of 7075 aluminium alloy with various aging treatments," Transactions of Nonferrous Metals Society of China, Vol. 18, No. 4, 2008, pp. 755-762.

[59] Krivoglaz, M.A., The Physics of Metals and Metallography, Vol. 10, No. 1, 1960.

[60] Krivoglaz, M.A., The Physics of Metals and Metallography, Vol. 12, No. 31, 1961.

[61] Kohen, M., Fantozzi, G., Fouquet, F., Proceedings ICIFUAS 5, Aachen, Germany, 1973, pp. 276.

[62] Williams, K.J., and Entwistle, K.M., "The Damping of Quench-Ageing Duralumin Vibrating at about 1 Cycle Per Second," Journal of the Institute of Metals, Vol. 87, No. 5, 1959, pp. 141-144.

[63] Cui, P., and Ke, T.S., "Anelastic Relaxation Peak Associated with the Presence of Incoherent Theta-Phase in Al-4wt-Percent-Cu Alloy," Materials Science and Engineering A-Structural Materials Properties Microstructure and Processing, Vol. 150, No. 2, 1992, pp. 281-288.

[64] Schoeck, G., "Internal Friction due to Precipitation," Physica Status Solidi, Vol. 32, No. 2, 1969, pp. 651-&.

[65] Riviere, A., and Pelosin, V., "Low frequency relaxation effect observed on 2024 aluminium alloy," Journal of Alloys and Compounds, Vol. 310, 2000, pp. 173-175.

[66] Belhas, S., Riviere, A., Woirgard, J., "High-Temperature Relaxation Mechanisms in Cu-Al Solid-Solutions," Journal De Physique, Vol. 46, No. C-10, 1985, pp. 367-370.

[67] Riviere, A., Gerland, M., and Pelosin, V., "Influence of dislocation networks on the relaxation peaks at intermediate temperature in pure metals and metallic alloys," Materials Science and Engineering A-Structural Materials Properties Microstructure and Processing, Vol. 521-22, 2009, pp. 94-97.

[68] Mondino, M., and Schoeck, G., "Coherency Loss and Internal Friction," Physica Status Solidi A-Applied Research, Vol. 6, No. 2, 1971, pp. 665-&.

[69] Engdahl, T., Hansen, V., Warren, P.J., "Investigation of fine scale precipitates in Al-Zn-Mg alloys after various heat treatments," Materials Science and Engineering A-Structural Materials Properties Microstructure and Processing, Vol. 327, No. 1, 2002, pp. 59-64.

[70] Macchi, C.E., Somoza, A., Dupasquier, A., "Secondary precipitation in Al-Zn-Mg-(Ag) alloys," Acta Materialia, Vol. 51, No. 17, 2003, pp. 5151-5158.

[71] Viana, F., Pinto, A.M.P., Santos, H.M.C., "Retrogression and re-ageing of 7075 aluminium alloy: microstructural characterization," Journal of Materials Processing Technology, Vol. 93, 1999, pp. 54-59.

[72] Konno, T.J., Kawasaki, M., and Hiraga, K., "Direct imaging of Guinier-Preston zones by high-angle annular detector dark-field scanning transmission electron microscopy," Journal of Electron Microscopy, Vol. 50, No. 2, 2001, pp. 105-111.

[73] Smith, G.W., "Precipitation kinetics in solutionized aluminum alloy 2124. Determination by scanning and isothermal Calorimetry," Thermochimica Acta, Vol. 317, No. 1, 1998, pp. 7-23.

[74] Abis, S., Mengucci, P., and Riontino, G., "A study of ageing in an AlCuMgZn foundry alloy," Materials Science and Engineering A-Structural Materials Properties Microstructure and Processing, Vol. 214, No. 1-2, 1996, pp. 153-160.

[75] Badini, C., Marino, F., and Verne, E., "Calorimetric Study on Precipitation Path in 2024-Alloy and its Sic Composite," Materials Science and Engineering A-Structural Materials Properties Microstructure and Processing, Vol. 191, No. 1-2, 1995, pp. 185-191.

[76] Ringer, S.P., Sakurai, T., and Polmear, I.J., "Origins of hardening in aged Al-Cu-Mg-(Ag) alloys," Acta Materialia, Vol. 45, No. 9, 1997, pp. 3731-3744.

[77] Charai, A., Walther, T., Alfonso, C., "Coexistence of clusters, GPB zones, S ''-, S '- and S-phases in an Al-0.9% Cu-1.4% Mg alloy," Acta Materialia, Vol. 48, No. 10, 2000, pp. 2751-2764.

[78] Badía, J.M., Antoranz, J.M., Tarín, P., "Influence of overaging on the mechanical properties and stress corrosion cracking behaviour of 7075 T6 aluminium alloy." Boletín De La Sociedad Española De Cerámica Y Vidrio, Vol. 43, No. 2, 2004, pp. 224-228.

[79] Sharma, M.M., Amateaub, M.F., and Eden, T.J., "Hardening mechanisms of spray formed Al–Zn–Mg–Cu alloys with scandium and other elemental additions," Journal of Alloys and Compounds, Vol. 416, No. 1-2, 2006, pp. 135-142.

[80] Graf, R., Polmear, I.J., Thomas, G., "The Ageing Characteristics of Ternary Aluminium Zinc Magnesium Alloys," Journal of the Institute of Metals, Vol. 86, No. 13, 1958, pp. 535-538.

[81] Lyman, C.E., and Vandersande, J.B., "Transmission Electron-Microscopy Investigation of Early Stages of Precipitation in an Al-Zn-mg Alloy," Metallurgical Transactions A-Physical Metallurgy and Materials Science, Vol. 7, No. 8, 1976, pp. 1211-1216.

[82] Batra, U., and Prabhakar, S.R., "Differential Scanning Calorimetric Analysis for 7075-Aluminum-Alloy," Transactions of the Indian Institute of Metals, Vol. 48, No. 1, 1995, pp. 55-61.

[83] Stiller, K., Warren, P.J., Hansen, V., "Investigation of precipitation in an Al-Zn-Mg alloy after two-step ageing treatment at 100 degrees and 150 degrees C," Materials Science and Engineering A-Structural Materials Properties Microstructure and Processing, Vol. 270, No. 1, 1999, pp. 55-63.

[84] Papazian, J.M., "Calorimetric Studies of Precipitation and Dissolution Kinetics in Aluminum-Alloys 2219 and 7075," Metallurgical Transactions A-Physical Metallurgy and Materials Science, Vol. 13, No. 5, 1982, pp. 761-769.

[85] Degischer, H.P., Zahra, C.Y., and Zahra, A., "Size Distribution of Metastable Phases in Al-10 and Al-15 Wt-Percent Zn Alloys," Zeitschrift Fur Metallkunde, Vol. 73, No. 10, 1982, pp. 635-640.

[86] Yannacopoulos, S., Kasap, S.O., Hedayat, A., "An Experimental-Study of Phase-Transformations in an Al-Zn-Mg-Zr Alloy - DSC and Hot Microhardness Measurements," Canadian Metallurgical Quarterly, Vol. 33, No. 1, 1994, pp. 51-60.

[87] Hansen, V., Stiller, K., Waterloo, G., "Structures and transformations during artificial aging of an industrial 7xxx-series Al-Zn-Mg-Zr alloy," Aluminum Alloys 2002: Their Physical and Mechanical Properties Pts 1-3, Vol. 396-4, 2002, pp. 815-820.

[88] De Sanctis, M., "Structure and properties of rapidly solidified ultrahigh strength Al---Zn---Mg---Cu alloys produced by spray deposition," Materials Science and Engineering A-Structural Materials Properties Microstructure and Processing, Vol. 141, No. 1, 1991, pp. 103-121.

[89] Park, J.K., and Ardell, A.J., "Microstructures of the Commercial-7075 Al-Alloy in the T651-Temper and T7-Temper," Metallurgical Transactions A-Physical Metallurgy and Materials Science, Vol. 14, No. 10, 1983, pp. 1957-1965.

[90] Lendvai, J., "Precipitation and strengthening in aluminium alloys," Aluminium Alloys: Their Physical and Mechanical Properties, Pts 1-3, Vol. 217, 1996, pp. 43-56.

[91] Berg, L.K., Gjonnes, J., Hansen, V., "GP-zones in Al-Zn-Mg alloys and their role in artificial aging," Acta Materialia, Vol. 49, No. 17, 2001, pp. 3443-3451.

[92] Li, X.Z., Hansen, V., Gjonnes, J., "HREM study and structure modeling of the eta ' phase, the hardening precipitates in commercial Al-Zn-Mg alloys," Acta Materialia, Vol. 47, No. 9, 1999, pp. 2651-2659.

[93] Maloney, S.K., Hono, K., Polmear, I.J., "The effects of a trace addition of silver upon elevated temperature ageing of an Al-Zn-Mg alloy," Micron, Vol. 32, No. 8, 2001, pp. 741-747.

[94] Salamci, E., "Calorimetric and transmission electron microscopy studies of spray deposited Al-Zn-Mg-Cu alloys," Materials Science and Technology, Vol. 20, No. 7, 2004, pp. 859-863.

[95] Papazian, J.M., "Differential Scanning Calorimetry Evaluation of Retrogressed and Re-Aged Microstructures in Aluminum-Alloy 7075," Materials Science and Engineering, Vol. 79, No. 1, 1986, pp. 97-104.

[96] Tankins, E.S., and Frazier, W.E., "Differential Scanning Calorimetric Studies of the Corrosion-Resistant Behavior in the 7000 Series Aluminum-Alloys," Materials Performance, Vol. 26, No. 6, 1987, pp. 37-44.

[97] Silcock, J.M., "The Structural Ageing Characteristics of Al-Cu-mg Alloys with Copper-Magnesium Weight Ratios of 7-1 and 2.2-1," Journal of the Institute of Metals, Vol. 89, No. 6, 1961, pp. 203-210.

[98] Starink, M.J., and Vanmourik, P., "Cooling and Heating Rate Dependence of Precipitation in an Al-Cu Alloy," Materials Science and Engineering A-Structural Materials Properties Microstructure and Processing, Vol. 156, No. 2, 1992, pp. 183-194.

[99] Sankaran, R., and Laird, C., "Effect of Trace Additions Cd, in and Sn on Interfacial Structure and Kinetics of Growth of Theta' Plates in Al-Cu Alloy," Materials Science and Engineering, Vol. 14, No. 3, 1974, pp. 271-279.

[100] Gupta, A.K., Gaunt, P., and Chaturvedi, M.C., "The Crystallography and Morphology of the S'-Phase Precipitate in an AlCuMg Alloy," Philosophical Magazine A-Physics of Condensed Matter Structure Defects and Mechanical Properties, Vol. 55, No. 3, 1987, pp. 375-387.

[101] Dixit, V., Mishra, R.S., Lederich, R.J., "Influence of process parameters on microstructural evolution and mechanical properties in friction stirred Al-2024 (T3) alloy," Science and Technology of Welding and Joining, Vol. 14, No. 4, 2009, pp. 346-355.

[102] Guinier, A., "Interprétation De La Diffusion Anormale Des Rayon-X Par Les Alliages a Durcissement Structural," Acta Crystallographica, Vol. 5, No. 1, 1952, pp. 121-130.

[103] Nicholson, R.B., and Nutting, J., "Direct Observation of the Strain Field Produced by Coherent Precipitated Particles in an Age-Hardened Alloy," Philosophical Magazine, Vol. 3, No. 29, 1958, pp. 531-&.

[104] Nicholson, R.B., Thomas, G., and Nutting, J., "Electron-Microscopic Studies of Precipitation in Aluminium Alloys," Journal of the Institute of Metals, Vol. 87, No. 12, 1959, pp. 429-438.

[105] Sato, T., Kojima, Y., and Takahashi, T., "Observations of the Microstructure of Pre-Precipitates in an Al-3-Percent-Cu Alloy by a Lattice Imaging Technique," Transactions of the Japan Institute of Metals, Vol. 23, No. 8, 1982, pp. 461-472.

[106] Osamura, K., Murakami, Y., Sato, T., "Structure of GP Zones in an Al-1.7 At-Percent Cu Alloy Aged for 14 Years at Room-Temperature," Acta Metallurgica, Vol. 31, No. 10, 1983, pp. 1669-1673.

[107] Sato, T., and Takahashi, T., "High-Resolution Electron-Microscopy on the Layered Structures of GP Zones in an Al-1.7at-Percent-Cu Alloy," Scripta Metallurgica, Vol. 22, No. 7, 1988, pp. 941-946.

[108] Hono, K., Hashizume, T., Hasegawa, Y., "A Study of Multilayer GP Zones in an Al-1.7at-Percent Cu Alloy by Atom-Probe Fim," Scripta Metallurgica, Vol. 20, No. 4, 1986, pp. 487-492.

[109] Hono, K., Satoh, T., and Hirano, K., "Evidence of Multilayer GP Zones in Al-1.7at-Percent-Cu Alloy," Philosophical Magazine A-Physics of Condensed Matter Structure Defects and Mechanical Properties, Vol. 53, No. 4, 1986, pp. 495-504.

[110] Gerold, V., "Uber Die Aushartung Von Aluminium-Silber-Legierungen .9. Rontgenographische Untersuchungen Uber Die Kalthartung," Zeitschrift Fur Metallkunde, Vol. 46, No. 9, 1955, pp. 623-631.

[111] Yoshida, H., Cockayne, D.J.H., and Whelan, M.J., "Study of Guinier-Preston Zones in Aluminum-Copper Alloys using Weak-Beam Technique of Electron-Microscopy," Philosophical Magazine, Vol. 34, No. 1, 1976, pp. 89-100.

[112] Papazian, J.M., "A Calorimetric Study of Precipitation in Aluminum-Alloy 2219," Metallurgical Transactions A-Physical Metallurgy and Materials Science, Vol. 12, No. 2, 1981, pp. 269-280.

[113] Shih, H.C., Ho, N.J., and Huang, J.C., "Precipitation behaviors in Al-Cu-Mg and 2024 aluminum alloys," Metallurgical and Materials Transactions A-Physical Metallurgy and Materials Science, Vol. 27, No. 9, 1996, pp. 2479-2494.

[114] Mittemeijer, E.J., "Analysis of the Kinetics of Phase-Transformations," Journal of Materials Science, Vol. 27, No. 15, 1992, pp. 3977-3987.

[115] Hersent, E., Driver, J.H., and Piot, D., "Modelling differential scanning Calorimetry curves of precipitation in Al-Cu-Mg," Scripta Materialia, Vol. 62, No. 7, 2010, pp. 455-457.

[116] Gersten, J.I., and Smith, F.W., "The Physics and chemistry of materials," John Wiley & Sons, Inc., New York, NY, USA, 2001, pp. 826.

[117] Christian, J.W., "The Theory of transformations in metals and alloys," Pergamon, Oxford, etc., 2002, pp. 1113.

[118] Liu, F., Sommer, F., Bos, C., "Analysis of solid state phase transformation kinetics: models and recipes," International Materials Reviews, Vol. 52, No. 4, 2007, pp. 193-212.

[119] Starink, M.J., and Zahra, A.M., "An analysis method for nucleation and growth controlled reactions at constant heating rate," Thermochimica Acta, Vol. 292, No. 1-2, 1997, pp. 159-168.

[120] Pradell, T., Crespo, D., Clavaguera, N., "Diffusion controlled grain growth in primary crystallization: Avrami exponents revisited," Journal of Physics-Condensed Matter, Vol. 10, No. 17, 1998, pp. 3833-3844.

[121] Kissinger, H.E., "Reaction Kinetics in Differential Thermal Analysis," Analytical Chemistry, Vol. 29, No. 11, 1957, pp. 1702-1706.

[122] Juhasz, A., Lendvai, J., and Kovacs, I., "The Early Stages of Clustering in Al-Zn-mg Alloys," Crystal Research and Technology, Vol. 20, No. 3, 1985, pp. 401-405.

[123] Ceresara, S., and Fiorini, P., "Resistometric Investigation of Aging Process After Quenching and Cold-Work in Al-Zn-Mg Alloys," Materials Science and Engineering, Vol. 10, No. 4, 1972, pp. 205-&.

[124] Dupasquier, A., Folegati, P., Rolando, A., "Solute Transport in an Al-Based Alloy Studied by Positron Annihilation Spectroscopy," Materials Science Forum, Vol. 175-178, 1995, pp. 351-354.

[125] Aaronson, H.I., and Laird, C., "Structure and Migration Kinetics of Alpha - Theta Prime Boundaries in Al-4% Cu. 2. Kinetics of Growth," Transactions of the Metallurgical Society of AIME, Vol. 242, No. 7, 1968, pp. 1437-&.

[126] Chen, Y.H., and Doherty, R.D., "Growth Kinetics of Plate-Shaped Precipitates in Aluminum-Copper and Aluminum-Gold Alloys," Scripta Metallurgica, Vol. 11, No. 9, 1977, pp. 725-729.

[127] Bhadeshia, H.K.D.H., "Differential Scanning Calorimetry."

[128] De Graef, M., "Introduction to conventional transmission electron microscopy," Cambridge University Press, Cambridge, UK, 2003, pp. 718.

[129] Jeong, H.T., Fleury, E., Kim, W.T., "Study on the mechanical relaxations of a Zr36Ti24Be40 amorphous alloy by time-temperature superposition principle," Journal of the Physical Society of Japan, Vol. 73, No. 11, 2004, pp. 3192-3197.

[130] Jeong, H.T., Kim, J.H., Kim, W.T., "The mechanical relaxations of a Mm(55)Al(25)Ni(10)Cu(10) amorphous alloy studied by dynamic mechanical analysis," Materials Science and Engineering A-Structural Materials Properties Microstructure and Processing, Vol. 385, No. 1-2, 2004, pp. 182-186.

[131] Jones, D.I.G., "On Temperature Frequency-Analysis of Polymer Dynamic Mechanical-Behavior," Journal of Sound and Vibration, Vol. 140, No. 1, 1990, pp. 85-102.

[132] Kamm, G.N., and Alers, G.A., "Low‐Temperature Elastic Moduli of Aluminum," Journal of Applied Physics, Vol. 35, No. 2, 1964, pp. 327-330.

[133] Varshni, Y.P., "Temperature Dependence of the Elastic Constants," Physical Review B, Vol. 2, No. 10, 1970, pp. 3952-3958.

[134] Granato, A., and Lucke, K., "Theory of Mechanical Damping due to Dislocations," Journal of Applied Physics, Vol. 27, No. 6, 1956, pp. 583-593.

[135] Zhang, Y., Godfrey, A., and Jensen, D.J., "Local boundary migration during recrystallization in pure aluminium," Scripta Materialia, Vol. 64, No. 4, 2011, pp. 331-334.

[136] Ozawa, T., "Estimation of Activation-Energy by Isoconversion Methods," Thermochimica Acta, Vol. 203, 1992, pp. 159-165.

[137] Hardy, H.K., "The Ageing Characteristics of some Ternary Aluminium Copper Magnesium Alloys with Copper Magnesium Weight Ratios of 7-1 and 2.2-1," Journal of the Institute of Metals, Vol. 83, No. 1, 1954, pp. 17-34.

[138] Ferry, J.D., "Viscoelastic properties of polymers," John Wiley and Sons, New York etc., 1980, pp. 641.

[139] Tanzilli, R.A., and Heckel, R.W., "Numerical Solutions to Finite Diffusion-Controlled 2-Phase Moving-Interface Problem (With Planar Cylindrical and Spherical Interfaces)," Transactions of the Metallurgical Society of Aime, Vol. 242, No. 11, 1968, pp. 2313-&.

[140] Baty, D.L., Tanzilli, R.A., and Heckel, R.W., "Solution Kinetics of Cual2 in an Al-4cu Alloy," Metallurgical Transactions, Vol. 1, No. 6, 1970, pp. 1651-&.

[141] Du, Y., Chang, Y.A., Huang, B.Y., "Diffusion coefficients of some solutes in fcc and liquid Al: critical evaluation and correlation," Materials Science and Engineering A-Structural Materials Properties Microstructure and Processing, Vol. 363, No. 1-2, 2003, pp. 140-151.

[142] Caillard, D., and Martin, J.L., "Microstructure of Aluminum during Creep at Intermediate Temperatures .3. the Rate Controlling Process," Acta Metallurgica, Vol. 31, No. 5, 1983, pp. 813-825.

[143] Washburn, J., "Intersection cross slip," Journal of Applied Physics Letters, Vol. 7, No. 183, 1965.

[144] Caillard, D., "A Model of Creep at Intermediate Temperatures in Aluminum," Philosophical Magazine A-Physics of Condensed Matter Structure Defects and Mechanical Properties, Vol. 51, No. 1, 1985, pp. 157-174.

[145] Ke, T.S., Cui, P., and Su, C.M., "Internal-Friction in High-Purity Aluminum Single-Crystals," Physica Status Solidi A-Applied Research, Vol. 84, No. 1, 1984, pp. 157-164.

[146] Woirgard, J., Amirault, J.P., and de Fouquet, J., "Internal Friction and Ultrasonic Attenuation in Solids," Lenz, D. and Lücke, K. eds., Springer-Verlag, Berlin, Germany, 1973.

[147] No, M.L., Esnouf, C., Sanjuan, J., "Internal-Friction at Medium Temperature in High-Purity Aluminum and its Relation with the Microstructure .1." Acta Metallurgica, Vol. 36, No. 4, 1988, pp. 827-836.

[148] Riviere, A., Gerland, M., and Pelosin, V., "High-temperature mechanical relaxation due to dislocation motion inside dislocation networks," Interaction between Defects and Anelastic Phenomena in Solids, Vol. 137, 2008, pp. 21-28.

[149] Riviere, A., and Gadaud, P., "High-temperature relaxations in aluminum studied by isothermal mechanical spectrometry," Metallurgical and Materials Transactions A-Physical Metallurgy and Materials Science, Vol. 28, No. 8, 1997, pp. 1661-1665.

[150] Riviere, A., and Woirgard, J., "Internal-Friction of Aluminum Following High-Temperature Cyclic Deformation," Scripta Metallurgica et Materialia, Vol. 25, No. 8, 1991, pp. 1911-1916.

ANNEX A. ERROR PROPAGATION ANALYSIS

A study was conducted to assess the propagation of uncertainty in the calculation of the dynamic elastic modulus by the DMA. Next follows a brief summary of this study.

The manufacturer provides the following model equation, which is used by the DMA for calculating the modulus using the measured stiffness and input dimensions of the samples:

$$E = \frac{K_S L^3}{\frac{6wd^3}{12}}\left(1+\frac{6}{10}(1+\nu)\left(\frac{d}{L}\right)^2\right)$$

where K_S is the measured stiffness, L is the sample length, w is the sample width, d is the sample thickness and ν is the Poisson's ratio. The propagation of relative errors is then given by:

$$\left(\frac{\Delta E}{E}\right)^2 = \left|\frac{\partial E}{\partial K_S}\right|^2\left(\frac{\Delta K_S}{E}\right)^2 + \left|\frac{\partial E}{\partial w}\right|^2\left(\frac{\Delta w}{E}\right)^2 + \left|\frac{\partial E}{\partial L}\right|^2\left(\frac{\Delta L}{E}\right)^2 + \left|\frac{\partial E}{\partial \nu}\right|^2\left(\frac{\Delta \nu}{E}\right)^2 + \left|\frac{\partial E}{\partial d}\right|^2\left(\frac{\Delta d}{E}\right)^2$$

After calculating the partial derivatives and introducing reference numerical values for all the variables, the relative error in the modulus was computed in five cases. Particularly, for each independent variable, the propagation of the error was assessed assuming a relative error of 1% for that variable and 0% for the others. The main conclusions derived from this analysis are that an error of 1% in stiffness or in sample width propagates into an error of 1% in storage modulus, while an error of 1% in sample length or thickness propagates respectively into an error of 3% in storage modulus.

ANNEX B. RELAXATIONS ASSOCIATED TO DISLOCATIONS

In this annex, further detail is given on relaxations associated to dislocations, a topic which was briefly introduced in Section 1.4.2. The following models have been proposed for dislocation motion [67]:

- A cross-slip mechanism at dislocation nodes [142], which requires high local stresses. At low temperature (e.g. RT), free dislocation segments are too small to make large relaxations possible. As temperature increases, the length of free segments increases too. Consequently, the peak becomes higher and shifts towards lower frequency. At higher temperatures, local stresses diminish so they no longer enable the relaxation mechanism, and the peak disappears. Low activation energy is expected if the metal has high stacking fault energy. This model is similar to the Washburn mechanism [143], which explains relaxation peaks in single crystals.
- A cross-slip mechanism between different families of dislocation planes arranged in polygonization walls [144].

For pure metals and alloys above RT, the following mechanisms have been observed which may be responsible for internal friction peaks associated to dislocations [67]:

- Climbing of dislocations by vacancy diffusion [145, 146].
- The dislocation motion mechanism proposed by Caillard [144], consisting in cross-slip between different families of dislocation planes arranged in polygonization walls, explains some relaxation peaks at higher temperature in poly-crystals.
- Dislocation sliding controlled by jogs induced by vacancy diffusion along dislocation lines [147].
- Dislocation motion inside:
    - Dislocation (cell) walls.
    - A dislocation network originated at around SiC whiskers [65, 148] (observed in an AlCu alloy).
    - Polygonization boundaries after re-crystallization [148, 149].
    - Dislocation walls created by high temperature alternating stresses [150] (observed in pure Al).

ANNEX C. MATLAB SOLVER CODE

The integration of the rate equations for GPZ/GPBZ dissolution and secondary precipitates formation was performed inside the least-squares non-linear fitting of the storage modulus model to experimental data, using MATLAB from The MathWorks Inc. For this purpose, a numerical procedure was designed. It was briefly introduced in Section 3.3. In this annex, the code is presented in detail.

C.1 SOLVER CODE: MfileNonlinearFitZZv16

```
%% M-file for MATLAB: Non-linear fit - All frequencies
%  Jose I. Rojas
%  2010

%  Main functionalities:
%  - Non-linear fit of proposed storage modulus model to DMA experimental results
%  - Integration of system of Differential Eq. using Runge-Kutta method for a system of Eq.

%  This M-file calls function handle: funDMA01StorageZZv16, which performs:
%  - Non-linear fit of proposed storage modulus model to DMA experimental results


%% Definition of global variables:

clear
clear global k tspan y0 T0 Tf t0 tf Data01 freqHz0 Nfreq freqs
clear global Time Y Choice02 Choice04 out01 nAvrE3 YE3 actEnergE3 preExpE3
clear global gb1 gb2 gb3 gb4 gb5 gb6 poltempKS02 timeS02 tempK02 minminTempC maxmaxTempC
clear global gbn j Nobpinit Nobpend Nobptotal Conc0E2 Conc0E3 E00 timeS tempK poltempKS
clear global TimeArray columnstspan timeMinmin timeMinmax ordnumber xf b0 fit Tk
clear global length startTfloor hr x0E3 iexpE3 betaE3 alphaE3 x0 iexp beta alpha

global k T0 Tf t0 tf Nfreq freqs nAvrE3 YE3 actEnergE3 preExpE3
global Time Y Choice02 Choice04 minminTempC maxmaxTempC ordnumber b0 fit
global gbn Nobpinit Nobpend Nobptotal Conc0E2 Conc0E3 E00 timeMinmin timeMinmax
global length startTfloor hr x0E3 iexpE3 betaE3 alphaE3 x0 iexp beta alpha xf


%% Input variables & initial values of fitting parameters:

%  Entry values through .txt file:     data = textread('filename','format')
display('Choose 1st .txt file with input data: initial values of fitting parameters')
[FileName00,PathName00,FilterIndex] = uigetfile('*.txt');
[Datafitparam, fit, code01, code02] = textread(FileName00,'%f %f %s %s')

%  Kinetics of GPZ dissolution:
actEnergE2 = Datafitparam(1,1);          % [eV/atom] Initial Ea for GPZ dissolution:
                                         %     AA 7075, GPZ formation:    1.21 > 0
                                         %     AA 2024, GPZ formation:    1.06 - 1.27 > 0
preExpE2 = Datafitparam(2,1);            % [1/s] Initial value for pre-exp. factor: 1.10e10

%  Kinetics of secondary precipitation:
actEnergE3 = Datafitparam(3,1);          % [eV/atom] Initial Ea for secondary precipitation:
                                         %     AA 7075, etha' formation:   1.26 > 0
                                         %     AA 2024, theta' formation:  1.11 > 0
preExpE3 = Datafitparam(4,1);            % [1/s] Initial value for pre-exp. factor: 2.28e9
nAvrE3 = Datafitparam(5,1);              % [-] Initial value for Avrami index: nAvrE3 > 0
                                         %     AA 7075, etha' formation:   n = 1.00
                                         %     AA 2024, theta' formation:  n = 1.10

%  Choosing number of frequencies to study:
Choice04 = input('Type in number of frequencies to study:  ');

%  Storage modulus model coefficients:
```

```
%E00 = Datafitparam(6,1)/1e10;          % [Pa] Input should be around 70 GPa
%E01 = Datafitparam(7,1)/1e8;           % [Pa/ºC] Input should be < 0 & around -40 MPa/ºC
%E02 = Datafitparam(8,1)/1e10;          % [Pa] Input should be > 0 & around 1e10 Pa
%E03 = Datafitparam(9,1)/1e10;          % [Pa] Input should be > 0 & around 1e10 Pa
E00E01E02E03 = zeros(4,Choice04);
for i=1:Choice04
   for z=1:4
      E00E01E02E03(z,i) = Datafitparam(5+4*(i-1)+z,1);
   end
end

%  Data for computation of initial precipitate concentration:
%AreaPdensE2 = 4e4;                     % [particles/micron2] For AA 7075-T6
AreaPdensE2 = 1e3;                      % [particles/micron2] Lack data for AA 2024-T3
AreaPdensE3 = 1e3;                      % [particles/micron2]
%PdiamE2 = 25;                          % [Armstrong] For AA 7075-T6
PdiamE2 = 80;                           % [Armstrong] GPZ diameter
PdiamE3 = 80;                           % [Armstrong] Secondary precipitates diameter
FractionGPZ = 0.75;                     % [-] Fraction of particles that are GPZ


%% Constants:

k = 8.617343e-5;                        % Boltzmann Constant [eV/K·atom]
Pi = 3.14159265;                        % Pi number


%% Computation of reference concentrations for GPZ & secondary precipitates:

VolPdensE2 = AreaPdensE2^(3/2);                 % [micron-3] Particles/unit volume
GPZVolPdensE2 = FractionGPZ*VolPdensE2;         % [micron-3] GPZ: 75% of particle content
PreVolPdensE3 = (1-FractionGPZ)*VolPdensE2;     % [micron-3] Precipitates: 25%
Vol1ParticE2 = (4/3)*Pi*(PdiamE2/(2*1e10))^3;   % [m3] Volume of a GPZ particle
Vol1ParticE3 = (4/3)*Pi*(PdiamE3/(2*1e10))^3;   % [m3] Volume of a secondary phase particle
%Conc0E2 = GPZVolPdensE2*(1e6)^3*Vol1ParticE2   % [-] Initial concentration of GPZ (at RT)
Conc0E2 = 0.049;                                % [-] Direct input of initial value of C1
%Conc0E3 = PreVolPdensE3*(1e6)^3*Vol1ParticE3   % [-] Final concentration of precipitates
Conc0E3 = 0.049;                                % [-] Direct input of final value of C2


%% Reading of experimental data: observation points, observed & calculated responses:

%  Data01 is a matrix of rowsData01-by-columnsData01 containing all data:
%     - observation points (T & time)
%     - experimental data measured by the DMA
%     - data calculated by DMA data acquisition software (TA Universal Analysis)
%  Note:  rows:              number n of observation points at which parameters are evaluated
%         columns:           number of evaluated parameters

%  Choosing .txt file to read:
display('Choose 2nd .txt file with input data: experimental results:  ')
[FileName01,PathName01,FilterIndex] = uigetfile('*.txt');
%Data00 = dlmread(FileName01, ' ');             % Reading data in .txt file
Data00 = dlmread(FileName01, '\t');             % Reading data in .txt file
[rowsData00,columnsData00] = size(Data00);      % Control: Size of matrix Data00

%  All parameters measured or computed by TA Universal Analysis software:
timeMin0 = Data00(1:end,1);             % Time [min]
tempC0 = Data00(1:end,2);               % Temp [ºC]
storageModMPa0 = Data00(1:end,3);       % Storage modulus [MPa]
lossModMPa0 = Data00(1:end,4);          % Loss modulus [MPa]
stressMPa0 = Data00(1:end,5);           % Stress [MPa]
tanDelta0 = Data00(1:end,6);            % Tan delta [-]
freqHz0 = Data00(1:end,7);              % Frequency [Hz]
driveForceN0 = Data00(1:end,8);         % Drive force [N]
amplitudemicron0 = Data00(1:end,9);     % Amplitude [microns]
strain0 = Data00(1:end,10);             % Strain [%]
dplmicron0 = Data00(1:end,11);          % Displacement [microns]
staticForceN0 = Data00(1:end,12);       % Static force [N]
positionmm0 = Data00(1:end,13);         % Position [mm]
lengthmm0 = Data00(1:end,14);           % Length [mm]
forceN0 = Data00(1:end,15);             % Force [N]
stiffnessNperm0 = Data00(1:end,16);     % Stiffness [N/m]
pressurekPa0 = Data00(1:end,17);        % Pressure [kPa]


%%  Define the studied frequencies:
```

```
Nfreq = input('Type in number of frequencies sampled in DMA tests:  ');
freqs = zeros(Nfreq,1);
for i=1:Nfreq
   freqs(i,1) = freqHz0(i,1);
end
%  Alternative: freqs = input('Type in Nfreq-by-1 vector of studied frenquecies:  ');


%%  Disregarding wrong data:

if (actEnergE2 < 0) || (preExpE2 < 0) || (actEnergE3 < 0) || (preExpE3 < 0) || (nAvrE3 < 0)
   display('The initial value of an input variable has a mistaken sign')
   break
elseif (E00 < 0) || (E01 > 0) || (E02 < 0) || (E03 < 0)
   display('The initial value of an input variable has a mistaken sign')
   break
else
   %  Nothing happens
end

%  Choosing freq to disregard:
Choice05 = input('Type in the number of frequencies you want to disregard:  ');
if (Choice05 < 0) || (Choice05 > Nfreq)
   display('Error in selected number of frequencies to disregard')
   break
else
   %  Nothing happens
end
floorChoice05 = floor(Choice05);
if (floorChoice05 >= 1) && (floorChoice05 <= Nfreq)
   Data03(1,1) = {Data00};
   freqs01(1,1) = {freqs};
   Choice06 = zeros(floorChoice05,1);
   for i=1:floorChoice05
      Choice06(i,1) = input('Type in a value of a frequency you want to disregard:  ');
      freqHz0 = Data03{1,i}(1:end,7);
      Data03(1,i+1) = {Data03{1,i}(freqHz0<Choice06(i,1)|freqHz0>(Choice06(i,1)+0.001),:)};
      freqs = freqs01{1,i};
      freqs01(1,i+1) = {freqs01{1,i}(freqs<Choice06(i,1)|freqs>(Choice06(i,1)+0.001),:)};
   end
   Data01 = Data03{1,floorChoice05+1};
   freqHz0 = 1;
   freqHz0 = Data01(1:end,7);
   Nfreq = Nfreq-floorChoice05;
   freqs = freqs01{1,floorChoice05+1};
elseif (floorChoice05 < 0) || (floorChoice05 > Nfreq)
   display('Error - Number of frequencies cannot be negative or larger than Nfreq')
   break
else
   Data01 = Data00;
end
global Data01 freqs


%% Split experimental data according to corresponding frequency:

for i=1:Nfreq
   Data02(1,i) = {Data01(freqHz0>=freqs(i,1)&freqHz0<(freqs(i,1)+0.001),:)};

   timeMin1(1,i) = {Data01(freqHz0>=freqs(i,1)&freqHz0<(freqs(i,1)+0.001),1)};
   tempC1(1,i) = {Data01(freqHz0>=freqs(i,1)&freqHz0<(freqs(i,1)+0.001),2)};
   storageModMPa1(1,i) = {Data01(freqHz0>=freqs(i,1)&freqHz0<(freqs(i,1)+0.001),3)};
   lossModMPa1(1,i) = {Data01(freqHz0>=freqs(i,1)&freqHz0<(freqs(i,1)+0.001),4)};
   stressMPa1(1,i) = {Data01(freqHz0>=freqs(i,1)&freqHz0<(freqs(i,1)+0.001),5)};
   tanDelta1(1,i) = {Data01(freqHz0>=freqs(i,1)&freqHz0<(freqs(i,1)+0.001),6)};
   freqHz1(1,i) = {Data01(freqHz0>=freqs(i,1)&freqHz0<(freqs(i,1)+0.001),7)};
   driveForceN1(1,i) = {Data01(freqHz0>=freqs(i,1)&freqHz0<(freqs(i,1)+0.001),8)};
   amplitudemicron1(1,i) = {Data01(freqHz0>=freqs(i,1)&freqHz0<(freqs(i,1)+0.001),9)};
   strain1(1,i) = {Data01(freqHz0>=freqs(i,1)&freqHz0<(freqs(i,1)+0.001),10)};
   dplmicron1(1,i) = {Data01(freqHz0>=freqs(i,1)&freqHz0<(freqs(i,1)+0.001),11)};
   staticForceN1(1,i) = {Data01(freqHz0>=freqs(i,1)&freqHz0<(freqs(i,1)+0.001),12)};
   positionmm1(1,i) = {Data01(freqHz0>=freqs(i,1)&freqHz0<(freqs(i,1)+0.001),13)};
   lengthmm1(1,i) = {Data01(freqHz0>=freqs(i,1)&freqHz0<(freqs(i,1)+0.001),14)};
   forceN1(1,i) = {Data01(freqHz0>=freqs(i,1)&freqHz0<(freqs(i,1)+0.001),15)};
   stiffnessNperm1(1,i) = {Data01(freqHz0>=freqs(i,1)&freqHz0<(freqs(i,1)+0.001),16)};
   pressurekPa1(1,i) = {Data01(freqHz0>=freqs(i,1)&freqHz0<(freqs(i,1)+0.001),17)};
```

```
    numberitems = histc(freqHz0,[freqs(i,1) freqs(i,1)+0.001]);
    numberitemsstorageModMPa3(i) = numberitems(1,1);

    timeMin2 = timeMin1{1,i};
    tempC2 = tempC1{1,i};
    storageModMPa2 = storageModMPa1{1,i};
    lossModMPa2 = lossModMPa1{1,i};
    stressMPa2 = stressMPa1{1,i};
    tanDelta2 = tanDelta1{1,i};
    freqHz2 = freqHz1{1,i};
    driveForceN2 = driveForceN1{1,i};
    amplitudemicron2 = amplitudemicron1{1,i};
    strain2 = strain1{1,i};
    dplmicron2 = dplmicron1{1,i};
    staticForceN2 = staticForceN1{1,i};
    positionmm2 = positionmm1{1,i};
    lengthmm2 = lengthmm1{1,i};
    forceN2 = forceN1{1,i};
    stiffnessNperm2 = stiffnessNperm1{1,i};
    pressurekPa2 = pressurekPa1{1,i};

    [rowsstorageModMPa2,columnsstorageModMPa2] = size(storageModMPa2);

    for j=1:rowsstorageModMPa2
        timeMin3(j,i) = timeMin2(j,1);
        tempC3(j,i) = tempC2(j,1);
        storageModMPa3(j,i) = storageModMPa2(j,1);
        lossModMPa3(j,i) = lossModMPa2(j,1);
        stressMPa3(j,i) = stressMPa2(j,1);
        tanDelta3(j,i) = tanDelta2(j,1);
        freqHz3(j,i) = freqHz2(j,1);
        driveForceN3(j,i) = driveForceN2(j,1);
        amplitudemicron3(j,i) = amplitudemicron2(j,1);
        strain3(j,i) = strain2(j,1);
        dplmicron3(j,i) = dplmicron2(j,1);
        staticForceN3(j,i) = staticForceN2(j,1);
        positionmm3(j,i) = positionmm2(j,1);
        lengthmm3(j,i) = lengthmm2(j,1);
        forceN3(j,i) = forceN2(j,1);
        stiffnessNperm3(j,i) = stiffnessNperm2(j,1);
        pressurekPa3(j,i) = pressurekPa2(j,1);
    end
end


%% Plotting all experimental data:

% Experimental data: Plot of Storage Modulus vs. Observation Points:
for i=1:Nfreq
    figure(i);
    plot(storageModMPa3(storageModMPa3(:,i)>0,i),'or','LineWidth',2)
    %plot(tempC3(tempC3(:,i)>0,i),'or','LineWidth',2)
    %plot(timeMin3(timeMin3(:,i)>0,i),'or','LineWidth',2)
    xlabel('Observation Points [-]')
    ylabel('Storage Modulus [MPa]')
    title('Experimental Data: Storage Modulus vs. Observation Points')
    legend('Storage Modulus [MPa]',1);
    hold off
end
%pause
%for i=1:Nfreq
%    figure(Nfreq+i);
%    plot(tempC3(storageModMPa3(:,i)>0,i),storageModMPa3(storageModMPa3(:,i)>0,i))
%    xlabel('Temperature [ºC]')
%    ylabel('Storage Modulus [MPa]')
%    title('Experimental Data: Storage Modulus vs. Temperature')
%    legend('Storage Modulus [MPa]',1);
%    hold off
%end


%% Select range of experimental data to be considered for non-linear fit:

Nobpinit = input('Type in vector of first observation points to consider:  ');
Nobpend = input('Type in vector of last observation points to consider:  ');
```

```
for i=1:Nfreq
   timeMin4(1,i) = {timeMin3(Nobpinit(i,1):Nobpend(i,1),i)};
   tempC4(1,i) = {tempC3(Nobpinit(i,1):Nobpend(i,1),i)};
   storageModMPa4(1,i) = {storageModMPa3(Nobpinit(i,1):Nobpend(i,1),i)};
   lossModMPa4(1,i) = {lossModMPa3(Nobpinit(i,1):Nobpend(i,1),i)};
   stressMPa4(1,i) = {stressMPa3(Nobpinit(i,1):Nobpend(i,1),i)};
   tanDelta4(1,i) = {tanDelta3(Nobpinit(i,1):Nobpend(i,1),i)};
   freqHz4(1,i) = {freqHz3(Nobpinit(i,1):Nobpend(i,1),i)};
   driveForceN4(1,i) = {driveForceN3(Nobpinit(i,1):Nobpend(i,1),i)};
   amplitudemicron4(1,i) = {amplitudemicron3(Nobpinit(i,1):Nobpend(i,1),i)};
   strain4(1,i) = {strain3(Nobpinit(i,1):Nobpend(i,1),i)};
   dplmicron4(1,i) = {dplmicron3(Nobpinit(i,1):Nobpend(i,1),i)};
   staticForceN4(1,i) = {staticForceN3(Nobpinit(i,1):Nobpend(i,1),i)};
   positionmm4(1,i) = {positionmm3(Nobpinit(i,1):Nobpend(i,1),i)};
   lengthmm4(1,i) = {lengthmm3(Nobpinit(i,1):Nobpend(i,1),i)};
   forceN4(1,i) = {forceN3(Nobpinit(i,1):Nobpend(i,1),i)};
   stiffnessNperm4(1,i) = {stiffnessNperm3(Nobpinit(i,1):Nobpend(i,1),i)};
   pressurekPa4(1,i) = {pressurekPa3(Nobpinit(i,1):Nobpend(i,1),i)};

   Data05{1,i} = [timeMin4{1,i} tempC4{1,i} storageModMPa4{1,i} lossModMPa4{1,i} ...
    ... stressMPa4{1,i} tanDelta4{1,i} freqHz4{1,i} driveForceN4{1,i} ...
    ... amplitudemicron4{1,i} strain4{1,i} dplmicron4{1,i} staticForceN4{1,i} ...
    ... positionmm4{1,i} lengthmm4{1,i} forceN4{1,i} stiffnessNperm4{1,i} pressurekPa4{1,i}];

   timeMinmin(i,1) = min(timeMin4{1,i});
   timeMinmax(i,1) = max(timeMin4{1,i});
end


%% Plotting selected experimental data:

% Experimental Data: Plot of Storage Modulus vs. Time:
for i=1:Nfreq
   %figure(Nfreq+i);
   figure(2*Nfreq+i);
   plot(timeMin4{1,i},storageModMPa4{1,i},'or','LineWidth',2)
   xlabel('Time [min]')
   ylabel('Storage Modulus [MPa]')
   title('Experimental Data: Storage Modulus vs. Time')
   legend('Storage Modulus [MPa]',1);
   hold off
end


%% Observation points: time & T:

timeS(1,Nfreq) = {0};
tempK(1,Nfreq) = {0};
for i=1:Nfreq
   timeS(1,i) = {timeMin4{1,i}*60};                    % Observation points: time [s]
   tempK(1,i) = {tempC4{1,i}+273.15};
end
global timeS tempK


%% Observed responses: storage modulus:

%   y is an n-by-1 vector of observed responses:
storageModExpPa(1,Nfreq) = {0};
for i=1:Nfreq
   storageModExpPa(1,i) = {storageModMPa4{1,i}*1e6};   % Observation points: time [s]
end


%% Initial conditions & other known data:

%  Runge-Kutta: Vector tspan (see below) specifying interval of integration:
for i=1:Nfreq
   t0(i,1) = timeMin4{1,i}(1,1)*60;                    % Initial test time [s]
   tf(i,1) = timeMin4{1,i}(end,1)*60;                  % Final test time [s]
end

%  Runge-Kutta: Vector y0 specifying initial conditions:
C0E2 = zeros(Nfreq,1);
C0E3 = zeros(Nfreq,1);
for i=1:Nfreq
   C0E2(i,1) = Conc0E2;
```

```
   C0E3(i,1) = Conc0E3;
end

%  Law T(t): T is linear with time t:
poltempKS(1,Nfreq) = {0};
for i=1:Nfreq
   poltempKS(1,i) = {polyfit(timeS{1,i},tempK{1,i},1)};
end
global poltempKS

%  Law T(t): T is linear with time t:
for i=1:Nfreq
   T0(i,1) = tempC4{1,i}(1,1)+273.15;                    % Initial test T [K]
   Tf(i,1) = tempC4{1,i}(end,1)+273.15;                  % Final of T test [K]
   Tslope(i,1) = (Tf(i,1)-T0(i,1))/(tf(i,1)-t0(i,1));    % Slope of T vs. time [K/s]
end


%% Recalling the fitting parameters:

%  - actEnergE2     % b(1) gb1      [eV/atom] Ea for GPZ dissolution
%  - preExpE2       % b(2) gb2      [1/s] Pre-exp. factor for GPZ dissolution
%  - actEnergE3     % b(3) gb3      [eV/atom] Ea for secondary precipitation
%  - preExpE3       % b(4) gb4      [1/s] Pre-exp. factor for secondary precipitation
%  - nAvrE3         % b(5) gb5      [-] Avrami index for secondary precipitation
%  - Ert            % b(6) gb6      [Pa] Storage modulus model coef. E0 for 1st freq.
%  - E0             % b(7) gb7      [Pa/ºC] Storage modulus model coef. E1 for 1st freq.
%  - E1             % b(8) gb8      [Pa] Storage modulus model coef. E2 for 1st freq.
%  - E2             % b(9) gb9      [Pa] Storage modulus model coef. E3 for 1st freq.
%  - Ert            % b(10) gb10    [Pa] Storage modulus model coef. E0 for 2nd freq.
%  - ...


%% Initial values of fitting parameters:

%  b0 is a p-by-1 vector of initial values of fitting parameters
%  Some of these values are scaled to order of magnitude 1:

   b0 = zeros(5+(4*Choice04),1);
   for i=1:5
      b0(i,1) = abs(Datafitparam(i,1));                  % Kinetic parameters
   end
   for i=1:Choice04
      b0(5+(4*i-3),1) = abs(Datafitparam(5+(4*i-3),1)/1e10);   % E00
      b0(5+(4*i-2),1) = -abs(Datafitparam(5+(4*i-2),1)/1e8);   % E01
      b0(5+(4*i-1),1) = abs(Datafitparam(5+(4*i-1),1)/1e10);   % E02
      b0(5+(4*i),1) = abs(Datafitparam(5+(4*i),1)/1e10);       % E03
   end
   [rowsb0,columnsb0] = size(b0)


%% Model function definition:

%  fun are function handles, specified by @ sign (as in @myfun) to a function like:
%  - [out01] = funDMA01StorageZZv16(b,X), for the nlinfit command
%  - dy = funDMA02StorageZZv16(t,y), for the solver ode45 command


%% Integration of rate Eq. performed inside least-squares non-linear fitting of model:

%  Integration of system of Diff. Eq. using Runge-Kutta method for a system of Eq.
%  - see funDMA01StorageZZv16
%  - see funDMA02StorageZZv16


%% Non-linear fitting:

%  Returns p-by-1 vector b of coefficient estimates for non-linear regression
%  of responses in y on predictors in X using model specified by function handle fun:
%  Example:                b = nlinfit(X,y,@fun,b0)

%  Choosing type of rate Eq. for GPZ dissolution:
display('Choose type of rate Eq. for GPZ dissolution')
Choice02 = input('Type in: 1) Jena 1989, 2) Eq. 5 Pap. 1982 or 3) Eq. 6 Pap. 1982:  ');
if (Choice02 < 1) || (Choice02 > 3)
   display('Error in selection of number')
   break
```

```
else
   %  Nothing happens
end

if (Choice04 < 1) || (Choice04 > Nfreq)
   display('Error in selection of number')
   break
else
   %  Nothing happens
end

%  Defining the ordinal numbers for the accummulated length of vectors:
ordnumber = zeros(Choice04+1,1);
for i=1:Choice04
   ordnumber(i+1,1) = Nobptotal(1,i)+ordnumber(i,1);
end
ordnumber

%  Defining X: cells timeS(1,i) arranged one after another:
X = zeros(ordnumber(Choice04+1,1),1);
for i=1:Choice04
   for j=1:Nobptotal(1,i)
      X(ordnumber(i,1)+j,1) = timeS{1,i}(j,1);
   end
end
for i=1:Choice04
   X(Nobpinit(i,1),1)
   timeS{1,i}(1,1)
   X(Nobpend(i,1),1)
   timeS{1,i}(end,1)
end

%  Defining y: cells storageModExpPa(1,i) arranged one after another:
y = zeros(ordnumber(Choice04+1,1),1);
for i=1:Choice04
   for j=1:Nobptotal(1,i)
      y(ordnumber(i,1)+j,1) = storageModExpPa{1,i}(j,1)/1e10;
   end
end
for i=1:Choice04
   y(Nobpinit(i,1),1)
   storageModExpPa{1,i}(1,1)/1e10
   y(Nobpend(i,1),1)
   storageModExpPa{1,i}(end,1)/1e10
end

%figure(6);
%plot(tspan)
%xlabel('Observation points [-]')
%ylabel('Time [s]')
%title('Tspan: Time vs. Observation Points')
%pause

%  Initial settings for Pap. models for GPZ concentration Y:
minTempC = zeros(Choice04,1);
maxTempC = zeros(Choice04,1);
for i=1:Choice04
   minTempC(i,1) = min(tempC4{1,i});
   maxTempC(i,1) = max(tempC4{1,i});
end
minminTempC = min(minTempC);
maxmaxTempC = max(maxTempC);
rstartTfloor = floor(minminTempC);                  % Initial T [ºC]
endTfloor = floor(maxmaxTempC);                     % Final T [ºC]
length = endTfloor+1-startTfloor;
xf = inf;                                           % Upper integration limit
hr = Tslope(1,1)*60;                                % [ºC/min] Heating rate
x0 = zeros(ordnumber(Choice04+1,1),1);
iexp = zeros(ordnumber(Choice04+1,1),1);
beta = zeros(ordnumber(Choice04+1,1),1);
alpha = zeros(ordnumber(Choice04+1,1),1);

%  Initial settings for computation of secondary precipitates concentration YE3:
x0E3 = zeros(ordnumber(Choice04+1,1),1);
iexpE3 = zeros(ordnumber(Choice04+1,1),1);
betaE3 = zeros(ordnumber(Choice04+1,1),1);
alphaE3 = zeros(ordnumber(Choice04+1,1),1);
```

```
YE3 = zeros(ordnumber(Choice04+1,1),1);

%  Start time of solving process:
clock01 = clock;

%  Non-linear fitting:
[b,res,Jacob,COVB,mse] = nlinfit(X,y,@funDMA01StorageZZv16,b0);

%  End time of solving process:
clock02 = clock;

if (Choice02 == 1)                                          % When using Jena 1989
   [rowsTime,columnsTime] = size(Time);
else
   %  nothing happens
end

%  Checkings:
[rowsY,columnsY] = size(Y);
[rowsgbn,columnsgbn] = size(gbn);

%  All scaled factors together (as many columns as Choice04):
actEnergE2fSca = abs(b(1));
preExpE2fSca = abs(b(2));
actEnergE3fSca = abs(b(3));
preExpE3fSca = abs(b(4));
nAvrE3fSca = abs(b(5));
E0E1E2E3fSca = zeros(4,Choice04);
for i=1:Choice04
   for z=1:4
      E0E1E2E3fSca(z,i) = b(5+4*(i-1)+z);
   end
end

%  All non-scaled factors together (as many columns as Choice04):
actEnergE2f = abs(b(1));
preExpE2f = abs(b(2));
actEnergE3f = abs(b(3));
preExpE3f = abs(b(4));
nAvrE3f = abs(b(5));
E0E1E2E3f = zeros(4,Choice04);
for i=1:Choice04
   E0E1E2E3f(1,i) = abs(b(5+1+4*(i-1)))*1e10;
   E0E1E2E3f(2,i) = -abs(b(5+2+4*(i-1)))*1e8;
   E0E1E2E3f(3,i) = abs(b(5+3+4*(i-1)))*1e10;
   E0E1E2E3f(4,i) = abs(b(5+4+4*(i-1)))*1e10;
end


%% Computation of model results:

%  Computation of model results in observation points:
%  EQ.:   E' = E'rt + E'0*T + E'1*C1 + E'2*C2
%         E' = b(6) + b(7)*T + b(8)*C1 + b(9)*C2               % For first frequency

chisquare01 = zeros(Choice04,1);
if (Choice02 == 1)                                          % When using Jena 1989
   for j=1:Choice04
      Efit01 = zeros(Nobptotal(1,j),1);
      Yproof = zeros(Nobptotal(1,j),1);
      for i=1:Nobptotal(1,j)
         tt = timeS{1,j}(i,1);
         [ktime,d0] = dsearchn(Time,tt);
         if (d0 == 0)
            Efit01(i,1) = E0E1E2E3f(1,j)+(E0E1E2E3f(2,j)*tempK{1,j}(i,1))+ ...
                          ... (E0E1E2E3f(3,j)*Y(ktime(1,1),1))+(E0E1E2E3f(4,j)*YE3(ordnumber(j,1)+i,1));
            Yproof(i,1) = Y(ktime(1,1),1);
         else
            if (ktime(1,1) == 1)
               Time01 = Time(1,1);
               Time02 = Time(2,1);
               Y01 = Y(1,1);
               Y02 = Y(2,1);
            elseif (ktime(1,1) == rowsTime)
               Time01 = Time(rowsTime-1,1);
               Time02 = Time(rowsTime,1);
               Y01 = Y(rowsTime-1,1);
```

```
            Y02 = Y(rowsTime,1);
         else
            d1 = tt-Time(ktime(1,1)-1,1);
            d2 = Time(ktime(1,1)+1,1)-tt;
            if (d1 > d2)
               Time01 = Time(ktime(1,1),1);
               Time02 = Time(ktime(1,1)+1,1);
               Y01 = Y(ktime(1,1),1);
               Y02 = Y(ktime(1,1)+1,1);
            else                                                % (d1 >= d2)
               Time01 = Time(ktime(1,1)-1,1);
               Time02 = Time(ktime(1,1),1);
               Y01 = Y(ktime(1,1)-1,1);
               Y02 = Y(ktime(1,1),1);
            end
         end
         poltempKS03 = polyfit([Time01; Time02],[Y01; Y02],1);
         Efit01(i,1) = E0E1E2E3f(1,j)+(E0E1E2E3f(2,j)*tempK{1,j}(i,1))+ ...
          ... (E0E1E2E3f(3,j)*polyval(poltempKS03,tt))+(E0E1E2E3f(4,j)*YE3(ordnumber(j,1)+i,1));
         Yproof(i,1) = polyval(poltempKS03,tt);
      end
      chisquare01(j,1) = chisquare01(j,1)+(((Efit01(i,1)/1e6)- ...
       ... storageModMPa4{1,j}(i,1))/storageModMPa4{1,j}(i,1))^2;
   end
   EfitArray(1,j) = {Efit01};
   YArray(1,j) = {Yproof};
   clear Efit01 Yproof tt poltempKS03
 end
else                                                            % When using Pap. 1982
 for j=1:Choice04
   Efit01 = zeros(Nobptotal(1,j),1);
   Yproof = zeros(Nobptotal(1,j),1);
   for i=1:Nobptotal(1,j)
      Efit01(i,1) = E0E1E2E3f(1,j)+(E0E1E2E3f(2,j)*tempK{1,j}(i,1))+ ...
       ... (E0E1E2E3f(3,j)*Y(ordnumber(j,1)+i,1))+(E0E1E2E3f(4,j)*YE3(ordnumber(j,1)+i,1));
      chisquare01(j,1) = chisquare01(j,1)+(((Efit01(i,1)/1e6)- ...
       ... storageModMPa4{1,j}(i,1))/storageModMPa4{1,j}(i,1))^2;
   end
   EfitArray(1,j) = {Efit01};
   YArray(1,j) = {Y((ordnumber(j,1)+1):ordnumber(j+1,1),1)};
   clear Efit01 Yproof tt poltempKS03
 end
end

%  Computation of tempC6: necessary for plotting Concentration vs. T:
if (Choice02 == 1)                                              % When using Jena 1989
   tempC6 = zeros(rowsTime,1);
   for i=1:rowsTime
      tt = Time(i,1);
      [ktime,d0] = dsearchn(timeMin0*60,tt);
      if (d0 == 0)
         tempC6(i,1) = tempC0(ktime(1,1),1);
      else
         if (ktime(1,1) == 1)
            Time01 = timeMin0(1,1)*60;
            Time02 = timeMin0(2,1)*60;
            tempC001 = tempC0(1,1);
            tempC002 = tempC0(2,1);
         elseif (ktime(1,1) == rowsData00)
            Time01 = timeMin0(rowsData00-1,1)*60;
            Time02 = timeMin0(rowsData00,1)*60;
            tempC001 = tempC0(rowsData00-1,1);
            tempC002 = tempC0(rowsData00,1);
         else
            d1 = tt-timeMin0(ktime(1,1)-1,1)*60;
            d2 = timeMin0(ktime(1,1)+1,1)*60-tt;
            if (d1 > d2)
               Time01 = timeMin0(ktime(1,1),1)*60;
               Time02 = timeMin0(ktime(1,1)+1,1)*60;
               tempC001 = tempC0(ktime(1,1),1);
               tempC002 = tempC0(ktime(1,1)+1,1);
            else                                                % (d1 > d2)
               Time01 = timeMin0(ktime(1,1)-1,1)*60;
               Time02 = timeMin0(ktime(1,1),1)*60;
               tempC001 = tempC0(ktime(1,1)-1,1);
               tempC002 = tempC0(ktime(1,1),1);
            end
```

```
        end
        poltempKS04 = polyfit([Time01; Time02],[tempC001; tempC002],1);
        tempC6(i,1) = polyval(poltempKS04,tt);
      end
   end
else                                                    % When using Papazian 1982
   %  Nothing happens
end


%% Goodness of the fit:

%  Chi-square distribution:
chisquare = zeros(1,Choice04);
for i=1:Choice04
   chisquare(1,i) = (1/Nobptotal(1,i))*chisquare01(i,1);
end


%% Writing output data in a .txt file:

%  Preparing matrix of initial values:
InitValues = zeros(15,Choice04);
for i=1:5
   InitValues(i,1) = b0(i,1);
end
for i=1:Choice04
   for z=1:4
      InitValues(5+z,i) = E00E01E02E03(z,i);
   end
   InitValues(12,i) = Nobpinit(i,1);
   InitValues(13,i) = Nobpend(i,1);
   InitValues(14,i) = freqs(i,1);
end
InitValues(10,1) = Conc0E2;
InitValues(11,1) = Conc0E3;
InitValues(15,1) = Choice02;

   Beep                                                 % Warning: simulation is about to end
   beep
   beep
   beep

for i=1:Choice04
   %  Output .txt file: Experimental data:
   [FileName02,PathName02,FilterIndex] = uiputfile('*.txt');
   dlmwrite(FileName02, Data05{1,i}, 'delimiter', '\t', 'precision', 6);

   %  Preparing matrix of data computed using the model:
   ModelData(:,1) = timeMin4{1,i};                      % [min] Test time
   ModelData(:,2) = tempC4{1,i};                        % [ºC] Test T
   ModelData(:,3) = YArray{1,i};                        % [-] GPZ conc.
   ModelData(:,4) = EfitArray{1,i}/1e6;                 % [MPa] Storage modulus
   ModelData(:,5) = YE3((ordnumber(i,1)+1):ordnumber(i+1,1));   % [-] Precipitates conc.

   %  Output .txt file: Model data:
   [FileName03,PathName03,FilterIndex] = uiputfile('*.txt');
   dlmwrite(FileName03, ModelData, 'delimiter', '\t', 'precision', 6);
   clear ModelData
end

%  Output .txt file: Initial values of fitting parameters & other initial conditions:
dlmwrite('Z02AllFreq-InitialValues.txt', InitValues, 'delimiter', '\t', 'precision', 6);

%  Output .txt file: Final values of fitting parameters & other important parameters:
output01 = zeros(12,max([Choice04; 5]));
output01(1,1) = actEnergE2f;
output01(2,:) = [preExpE2f actEnergE2f preExpE3f actEnergE3f nAvrE3f];
output01(3,1) = actEnergE3f;
output01(4,1) = preExpE3f;
output01(5,1) = nAvrE3f;
for i=1:Choice04
   for j=6:9
      output01(j,i) = E0E1E2E3f(j-5,i);
   end
   output01(10,i) = freqs(i,1);
   output01(13,i) = chisquare(1,i);
```

```
end
for i=1:5
   output01(11,i) = clock01(1,i);
   output01(12,i) = clock02(1,i);
end
dlmwrite('Z03AllFreq-Output01.txt', output01, 'delimiter', '\t', 'precision', 6);

%  Output .txt file: Final values of fitting parameters for re-starting the iteration loop:
output02 = zeros(5+4*Choice04,2);
output02(1,1) = actEnergE2f;
output02(2,1) = preExpE2f;
output02(3,1) = actEnergE3f;
output02(4,1) = preExpE3f;
output02(5,1) = nAvrE3f;
for i=1:Choice04
   for z=1:4
      output02(5+4*(i-1)+z,1) = E0E1E2E3f(z,i);
   end
end
for i=1:(5+4*Choice04)
   output02(i,2) = fit(i,1);
end
dlmwrite('Z04AllFreq-Output02.txt', output02, 'delimiter', '\t', 'precision', 6);


%% Plot of experimental data together with non-linear fit data:

%  Plot of exp. & numerical E' vs. T to allow comparison:
for i=1:Choice04
   figure(3*Nfreq+i);
   plot(tempC4{1,i},storageModMPa4{1,i},'or','LineWidth',2,'MarkerEdgeColor','r')
   xlabel('Temperature [ºC]')
   ylabel('Storage Modulus [MPa]')
   title('Non-linear fit: Storage Modulus vs. Temperature')
   hold on
   plot(tempC4{1,i},EfitArray{1,i}/1e6,'-b','LineWidth',2,'MarkerEdgeColor','b')
   legend('Experimental Data [MPa]','Model Data [MPa]',2);
   hold off
   print('-djpeg',3*Nfreq+i)
end

%  Plot of GPZ concentration vs. Time:
if (Choice02 == 1)                                          % When using Jena 1989
   figure(4*Nfreq+1);
   plot(Time/60,Y,'ob','LineWidth',2,'MarkerEdgeColor','b','MarkerFaceColor','w')
   xlabel('Time [min]')
   ylabel('GPZ Concentration [-]')
   title('Computed GPZ Concentration vs. Time')
   legend('GPZ Conc. [-]',1);
   hold off
   print -djpeg fig01GPZConc.jpeg
else                                                        % When using Papazian 1982
   figure(4*Nfreq+1);
   plot(timeS{1,1}/60,Y(1:Nobptotal(1,1),1),'ob','LineWidth',2,'MarkerEdgeColor','b)
   xlabel('Time [min]')
   ylabel('GPZ Concentration [-]')
   title('Computed GPZ Concentration vs. Time')
   if (Choice04 >= 2)
      hold on
      for i=2:Choice04
         plot(timeS{1,i}/60,Y((ordnumber(i,1)+1):ordnumber(i+1,1),1),'ob','LineWidth',2)
      end
   else
      %  Nothing happens
   end
   legend('GPZ Conc. [-]',1);
   hold off
   print -djpeg fig01GPZConc.jpeg
end

%  Plot of GPZ concentration vs. T:
if (Choice02 == 1)                                          % When using Jena 1989
   figure(5*Nfreq+1);
   plot(tempC6,Y,'ob','LineWidth',2,'MarkerEdgeColor','b','MarkerFaceColor','w','MarkerSize',2)
   xlabel('Temperature [ºC]')
   ylabel('GPZ Concentration [-]')
   title('Computed GPZ Concentration vs. Temperature')
```

```
    legend('GPZ Conc. [-]',1);
    hold off
    print -djpeg fig02GPZConc.jpeg
else                                                    % When using Papazian 1982
    figure(5*Nfreq+1);
    plot(tempK{1,1}-273.15,Y(1:Nobptotal(1,1),1),'ob','LineWidth',2)
    xlabel('Temperature [ºC]')
    ylabel('GPZ Concentration [-]')
    title('Computed GPZ Concentration vs. Temperature')
    if (Choice04 >= 2)
        hold on
        for i=2:Choice04
            plot(tempK{1,i}-273.15,Y((ordnumber(i,1)+1):ordnumber(i+1,1),1),'ob','LineWidth',2)
        end
    else
        %  Nothing happens
    end
    legend('GPZ Conc. [-]',1);
    hold off
    print -djpeg fig02GPZConc.jpeg
end

%  Plot of secondary precipitates concentration vs. Time:
    figure(6*Nfreq+1)
    plot(timeS{1,1}/60,YE3(1:Nobptotal(1,1),1),'or','LineWidth',2,'MarkerEdgeColor','r')
    xlabel('Time [min]')
    ylabel('Precipitate Concentration [-]')
    title('Computed Precipitate Concentration vs. Time')
    if (Choice04 >= 2)
        hold on
        for i=2:Choice04
            plot(timeS{1,i}/60,YE3((ordnumber(i,1)+1):ordnumber(i+1,1),1),'or','LineWidth',2)
        end
    else
        %  Nothing happens
    end
    legend('Precipitate Conc. [-]',1);
    hold off
    print -djpeg fig03PrecConc.jpeg

%  Plot of secondary precipitates concentration vs. T:
    figure(7*Nfreq+1)
    plot(tempK{1,1}-273.15,YE3(1:Nobptotal(1,1),1),'or','LineWidth',2,'MarkerEdgeColor','r')
    xlabel('Temperature [ºC]')
    ylabel('Precipitate Concentration [-]')
    title('Computed Precipitate Concentration vs. Temperature')
    if (Choice04 >= 2)
        hold on
        for i=2:Choice04
            plot(tempK{1,i}-273.15,YE3((ordnumber(i,1)+1):ordnumber(i+1,1),1),'or','LineWidth',2)
        end
    else
        %  Nothing happens
    end
    legend('Precipitate Conc. [-]',1);
    hold off
    print -djpeg fig04PrecConc.jpeg
```

C.2 FUNCTION HANDLE: funDMA01StorageZZv16

```
%% Function handle for M-file for MATLAB: Non-linear fit - All frequencies
%  Jose I. Rojas
%  2010

%  Main functionality:
%  - Non-linear fit of proposed storage modulus model to DMA experimental results

%  This function handle is called by M-file: MfileNonlinearFitZZv16
%  This function handle calls function handle: funDMA02StorageZZv16, which performs:
%  - Integration of system of Differential Eq. using Runge-Kutta method for a system of Eq.
```

```
%% Recalling the fitting parameters:

%  - actEnergE2     % b(1) gb1          [eV/atom] Ea for GPZ dissolution
%  - preExpE2       % b(2) gb2          [1/s] Pre-exp. factor for GPZ dissolution
%  - actEnergE3     % b(3) gb3          [eV/atom] Ea for secondary precipitation
%  - preExpE3       % b(4) gb4          [1/s] Pre-exp. factor for secondary precipitation
%  - nAvrE3         % b(5) gb5          [-] Avrami index for secondary precipitation
%  - Ert            % b(6) gb6          [Pa] Storage modulus model coef. E0 for 1st freq.
%  - E0             % b(7) gb7          [Pa/ºC] Storage modulus model coef. E1 for 1st freq.
%  - E1             % b(8) gb8          [Pa] Storage modulus model coef. E2 for 1st freq.
%  - E2             % b(9) gb9          [Pa] Storage modulus model coef. E3 for 1st freq.
%  - Ert            % b(10) gb10        [Pa] Storage modulus model coef. E0 for 2nd freq.
%  - ...


%% Function handle definition:

function [out01] = funDMA01StorageZZv16(b,X)

global tspan k y0 Data01 Nfreq freqs YE3
global Time Y Choice02 Choice04 j timeS02 tempK02
global gbn timeS tempK Conc0E2 Conc0E3 E00 timeMinmin timeMinmax ordnumber
global hr x0E3 iexpE3 betaE3 alphaE3 x0 iexp beta alpha xf b0 fit

if (fit(1,1) > 0)
   gbn(1) = abs(b(1));
else
   gbn(1) = b0(1,1);
end
if (fit(2,1) > 0)
   gbn(2) = abs(b(2));
else
   gbn(2) = b0(2,1);
end
if (fit(3,1) > 0)
   gbn(3) = abs(b(3));
else
   gbn(3) = b0(3,1);
end
if (fit(4,1) > 0)
   gbn(4) = abs(b(4));
else
   gbn(4) = b0(4,1);
end
if (fit(5,1) > 0)
   gbn(5) = abs(b(5));
else
   gbn(5) = b0(5,1);
end
if (fit(6,1) > 0)
   for i=1:Choice04
      gbn(5+(4*i-3)) = abs(b(5+(4*i-3)));
   end
else
   for i=1:Choice04
      gbn(5+(4*i-3)) = b0(5+(4*i-3),1);
   end
end
if (fit(7,1) > 0)
   for i=1:Choice04
      gbn(5+(4*i-2)) = -abs(b(5+(4*i-2)));
   end
else
   for i=1:Choice04
      gbn(5+(4*i-2)) = b0(5+(4*i-2),1);
   end
end
if (fit(8,1) > 0)
   for i=1:Choice04
      gbn(5+(4*i-1)) = abs(b(5+(4*i-1)));
   end
else
   for i=1:Choice04
      gbn(5+(4*i-1)) = b0(5+(4*i-1),1);
   end
end
if (fit(9,1) > 0)
```

```
   for i=1:Choice04
      gbn(5+(4*i)) = abs(b(5+(4*i)));
   end
else
   for i=1:Choice04
      gbn(5+(4*i)) = b0(5+(4*i),1);
   end
end

%  Definition of tolerances:
AbsoTol = 1e-4;

clear tspan

%  METHOD 01:
Data04(1,1) = {Data01};
for i=1:(Nfreq-Choice04)
   clear freqHz0
   freqHz0 = Data04{1,i}(:,7);
   Data04(1,i+1) = {Data04{1,i}(freqHz0<freqs(Nfreq-(i-1),1)|freqHz0>(freqs(Nfreq-(i-1),1)+0.001),:)};
end
clear Data01
Data05 = Data04{1,(Nfreq-Choice04+1)};
Data01 = Data05(1:ordnumber(Choice04+1,1),:);

%  METHOD 04:
timeS03 = Data01(:,1)*60;
tspan = [min(timeMinmin*60) max(timeMinmax*60)];
y0 = Conc0E2;
timeS02 = timeS03;
tempK02 = Data01(:,2) + 273.15;

%  Calculus of precipitate concentration YE3:
ffE3 = gbn(4)*gbn(3)/(k*hr);
for z=1:Choice04
   [rowstimeS,columnstimeS] = size(timeS{1,z});
   for i=1:rowstimeS
      x0E3(ordnumber(z,1)+i,1) = gbn(3)/(k*tempK{1,z}(i,1));  % lower integration limit
      iexpE3(ordnumber(z,1)+i,1) = quadgk(@funHelpPapazian,x0E3(ordnumber(z,1)+i,1),xf);
      betaE3(ordnumber(z,1)+i,1) = ffE3*iexpE3(ordnumber(z,1)+i,1);
      alphaE3(ordnumber(z,1)+i,1) = min(abs(1-exp(-betaE3(ordnumber(z,1)+i,1)^gbn(5))),1);
   end
end
YE3 = Conc0E3*alphaE3;


if (Choice02 == 1)                          % When using Jena 1989

   %  Solver command using Rung-Kutta for a system of DEs:
   %[T,Y] = solver(odefun,tspan,y0);
   %[T,Y] = ode45(@rigid,[0 12],[0 1 1],options);
   %  dy = funDMA02StorageZZv16(t,y)
   %  Time:   Column vector of time points = coincidental with timeS
   %  Y:      Solution array: each row in Y corresponds to solution [E C] at a
   %  time returned in corresponding row of T
   %options = odeset('RelTol',1e-4,'AbsTol',AbsoTol,'Stats','on');
   %  Default: RelTol: 1e-3 = 0.1%; Stats: off
   options = odeset('RelTol',1e-4,'AbsTol',AbsoTol);
   [Time,Y] = ode45(@funDMA02StorageZZv16,tspan,y0,options);
   [rowsTime,columnsTime] = size(Time);

   for j=1:Choice04
      [rowstimeS,columnstimeS] = size(timeS{1,j});

      for i=1:rowstimeS
         %  METHOD 04:
         tt = timeS{1,j}(i,1);
         [ktime,d0] = dsearchn(Time,tt);
         if (d0 == 0)
            out01(ordnumber(j,1)+i,1) = gbn(5+(4*j-3))+(gbn(5+(4*j-2))/100)*tempK{1,j}(i,1)+ ...
             ... gbn(5+(4*j-1))*Y(ktime(1,1),1)+gbn(5+(4*j))*YE3(ordnumber(j,1)+i,1);
         else
            if (ktime(1,1) == 1)
               Time01 = Time(1,1);
               Time02 = Time(2,1);
               Y01 = Y(1,1);
               Y02 = Y(2,1);
```

```
            elseif (ktime(1,1) == rowsTime)
               Time01 = Time(rowsTime-1,1);
               Time02 = Time(rowsTime,1);
               Y01 = Y(rowsTime-1,1);
               Y02 = Y(rowsTime,1);
            else
               d1 = tt - Time(ktime(1,1)-1,1);
               d2 = Time(ktime(1,1)+1,1) - tt;
               if (d1 > d2)
                  Time01 = Time(ktime(1,1),1);
                  Time02 = Time(ktime(1,1)+1,1);
                  Y01 = Y(ktime(1,1),1);
                  Y02 = Y(ktime(1,1)+1,1);
               else  % (d1 >= d2)
                  Time01 = Time(ktime(1,1)-1,1);
                  Time02 = Time(ktime(1,1),1);
                  Y01 = Y(ktime(1,1)-1,1);
                  Y02 = Y(ktime(1,1),1);
               end
            end
            poltempKS03 = polyfit([Time01; Time02],[Y01; Y02],1);
            out01(ordnumber(j,1)+i,1) = gbn(5+(4*j-3))+(gbn(5+(4*j-2))/100)*tempK{1,j}(i,1)+ ...
             ... gbn(5+(4*j-1))*polyval(poltempKS03,tt)+gbn(5+(4*j))*YE3(ordnumber(j,1)+i,1);
         end
      end
   end

elseif (Choice02 == 2)                          % When using Eq 5 from Pap. 1982

   %  Calculus of GPZ concentration Y:
   ff = gbn(2)*gbn(1)/(k*hr);
   for z=1:Choice04
      [rowstimeS,columnstimeS] = size(timeS{1,z});
      for i=1:rowstimeS
         x0(ordnumber(z,1)+i,1) = gbn(1)/(k*tempK{1,z}(i,1));  % lower integration limit
         iexp(ordnumber(z,1)+i,1) = quadgk(@funHelpPapazian,x0(ordnumber(z,1)+i,1),xf);
         beta(ordnumber(z,1)+i,1) = ff*iexp(ordnumber(z,1)+i,1);
         alpha(ordnumber(z,1)+i,1) = min(abs(1-(1-sqrt(beta(ordnumber(z,1)+i,1)))^3),1);
      end
   end
   Y = Conc0E2*(1-alpha);

   for j=1:Choice04
      [rowstempK,columnstempK] = size(tempK{1,j});
      for i=1:rowstempK
         out01(ordnumber(j,1)+i,1) = gbn(5+(4*j-3))+(gbn(5+(4*j-2))/100)*tempK{1,j}(i,1)+ ...
          ... gbn(5+(4*j-1))*Y(ordnumber(j,1)+i,1)+gbn(5+(4*j))*YE3(ordnumber(j,1)+i,1);
      end
   end

else                                            % When using Eq 6 from Papazian 1982

   %  Calculus of GPZ concentration Y:
   ff = gbn(2)*gbn(1)/(k*hr);
   for z=1:Choice04
      [rowstimeS,columnstimeS] = size(timeS{1,z});
      for i=1:rowstimeS
         x0(ordnumber(z,1)+i,1) = gbn(1)/(k*tempK{1,z}(i,1));  % lower integration limit
         iexp(ordnumber(z,1)+i,1) = quadgk(@funHelpPapazian,x0(ordnumber(z,1)+i,1),xf);
         beta(ordnumber(z,1)+i,1) = ff*iexp(ordnumber(z,1)+i,1);
         alpha(ordnumber(z,1)+i,1) = min(abs(1-exp(-beta(ordnumber(z,1)+i,1))),1);
      end
   end
   Y = Conc0E2*(1-alpha);

   for j=1:Choice04
      [rowstempK,columnstempK] = size(tempK{1,j});
      for i=1:rowstempK
         out01(ordnumber(j,1)+i,1) = gbn(5+(4*j-3))+(gbn(5+(4*j-2))/100)*tempK{1,j}(i,1)+ ...
          ... gbn(5+(4*j-1))*Y(ordnumber(j,1)+i,1)+gbn(5+(4*j))*YE3(ordnumber(j,1)+i,1);
      end
   end

end
end
```

C.3 FUNCTION HANDLE: funDMA02StorageZZv16

```
%% Function handle for function handle for M-file for MATLAB: Non-linear fit - All frequencies
%  Jose I. Rojas
%  2010

%  Main functionality:
%  - Integration of system of Differential Eq. using Runge-Kutta method for a system of Eq.

%  This function handle is called by function handle: funDMA02StorageZZv16


%% Recalling the fitting parameters:

%  - actEnergE2     % b(1) gb1          [eV/atom] Ea for GPZ dissolution
%  - preExpE2       % b(2) gb2          [1/s] Pre-exp. factor for GPZ dissolution
%  - actEnergE3     % b(3) gb3          [eV/atom] Ea for secondary precipitation
%  - preExpE3       % b(4) gb4          [1/s] Pre-exp. factor for secondary precipitation
%  - nAvrE3         % b(5) gb5          [-] Avrami index for secondary precipitation
%  - Ert            % b(6) gb6          [Pa] Storage modulus model coef. E0 for 1st freq.
%  - E0             % b(7) gb7          [Pa/ºC] Storage modulus model coef. E1 for 1st freq.
%  - E1             % b(8) gb8          [Pa] Storage modulus model coef. E2 for 1st freq.
%  - E2             % b(9) gb9          [Pa] Storage modulus model coef. E3 for 1st freq.
%  - Ert            % b(10) gb10        [Pa] Storage modulus model coef. E0 for 2nd freq.
%  - ...


%% Function handle definition:
%  fun is function handle, specified by @ sign (as in @myfun) to function like: yhat = myfun(b,X):

function dy = funDMA02StorageZZv16(t,y)

global k gbn j timeS02 tempK02

dy = zeros(1,1);

   [ktime,d0] = dsearchn(timeS02,t);
   [rowstimeS02,columnstimeS02] = size(timeS02);

if (d0 == 0)

   dy(1) = -y(1)*gbn(2)*exp(-gbn(1)/(k*tempK02(ktime(1,1),1)));    % when using Jena 1989

else

   if (ktime(1,1) == 1)
      timeS0201 = timeS02(1,1);
      timeS0202 = timeS02(2,1);
      tempK0201 = tempK02(1,1);
      tempK0202 = tempK02(2,1);
   elseif (ktime(1,1) == rowstimeS02)
      timeS0201 = timeS02(rowstimeS02-1,1);
      timeS0202 = timeS02(rowstimeS02,1);
      tempK0201 = tempK02(rowstimeS02-1,1);
      tempK0202 = tempK02(rowstimeS02,1);
   else
      d1 = t - timeS02(ktime(1,1)-1,1);
      d2 = timeS02(ktime(1,1)+1,1) - t;
      if (d1 > d2)
         timeS0201 = timeS02(ktime(1,1),1);
         timeS0202 = timeS02(ktime(1,1)+1,1);
         tempK0201 = tempK02(ktime(1,1),1);
         tempK0202 = tempK02(ktime(1,1)+1,1);
      else                                          % (d1 >= d2)
         timeS0201 = timeS02(ktime(1,1)-1,1);
         timeS0202 = timeS02(ktime(1,1),1);
         tempK0201 = tempK02(ktime(1,1)-1,1);
         tempK0202 = tempK02(ktime(1,1),1);
      end
   end

   poltempKS03 = polyfit([timeS0201; timeS0202],[tempK0201; tempK0202],1);
   dy(1) = -y(1)*gbn(2)*exp(-gbn(1)/(k*polyval(poltempKS03,t)));   % When using Jena 1989

end
```